Université de Liège
**Faculté des Sciences**
Département de Mathématique

# Application of wavelet transforms to geosciences: Extraction of functional and frequential information

Dissertation présentée par
**ADRIEN DELIÈGE**
en vue de l'obtention du grade de Docteur en Sciences

— Mai 2017 —

| | | | | | |
|---|---|---|---|---|---|
| A. Arneodo<br>**Rapporteur** | F. Bastin<br>**Président** | X. Fettweis | P. Flandrin<br>**Rapporteur** | G. Mabille | S. Nicolay<br>**Promoteur** |

©Université de Liège, Belgique

*"As far as the laws of mathematics refer to reality,*
*they are not certain;*
*and as far as they are certain,*
*they do not refer to reality."*
A. Einstein

# Abstract

It is now well-known that there exist functions that are continuous but nowhere differentiable. Still, it appears that some of them are less "irregular" than others. The pointwise regularity of a function can be characterized by its Hölder exponent at each point. For the sake of practicability, it is more appropriate to determine the "size" of the sets of points sharing a same exponent, through their Hausdorff measure. By doing so, one gets the multifractal spectrum of a function, which characterizes in particular its monofractal or multifractal nature.

The first part of this work is based on the so-called "wavelet leaders method" (WLM), recently developed in the context of multifractal analysis, and aims at its application to concrete situations in geosciences. First, we present the WLM and we insist particularly on the major differences between theory and practice in its use and in the interpretation of the results. Then, we show that the WLM turns out to be an efficient tool for the analysis of Mars topography from a unidimensional and bidimensional point of view; the first approach allowing to recover information consistent with previous works, the second being new and highlighting some areas of interest on Mars. Then, we study the regularity of temperature signals related to various climate stations spread across Europe. In a first phase, we show that the WLM allows to detect a strong correlation with pressure anomalies. Then we show that the Hölder exponents obtained are directly linked to the underlying climate and we establish criteria that compare them with their climate characteristics as defined by the Köppen-Geiger classification.

On the other hand, the continuous version of the wavelet transform (CWT), developed in the context of time-frequency analysis, is also studied in this work. The objective here is the determination of dominant periods and the extraction of the associated oscillating components that constitute a given signal. The CWT allows, unlike the Fourier transform, to obtain a representation in time and in frequency of the considered signal, which thus opens new research perspectives. Moreover, with a Morlet-like wavelet, a simple reconstruction formula can be used to extract components.

Therefore, the second part of the manuscript presents the CWT and focuses mainly on the border effects inherent to this technique. We illustrate the advantages of the zero-padding and introduce an iterative method allowing to alleviate significantly reconstruction errors at the borders of the signals. Then, we study in detail the El Niño Southern Oscillation (ENSO) signal related to temperature anomalies in the Pacific Ocean and responsible for extreme climate events called El Niño (EN) and La Niña (LN). Through the CWT, we distinguish its main periods and we extract its dominant components, which reflect well-known geophysical mechanisms. A meticulous study of these components allows us to elaborate a forecasting algorithm for EN and LN events with lead times larger than one year, which is a much better performance than current models. After, we generalize the method used to extract components by developing a procedure that detects ridges in the CWT. The algorithm, called WIME (Wavelet-Induced Mode Extraction), is illustrated on several highly non-stationary examples. Its ability to recover target components from a given signal is tested and compared with the Empirical Mode Decomposition. It appears that WIME has a better adaptability in various situations. Finally, we show that WIME can be used in real-life cases such as an electrocardiogram and the ENSO signal.

# Résumé

Il est désormais bien connu qu'il existe des fonctions continues nulle part dérivables. Cependant, il apparaît que certaines d'entre elles soient tout de même moins "irrégulières" que d'autres. La régularité ponctuelle d'une fonction peut se caractériser par son exposant de Hölder en chaque point. Dans un souci de faisabilité, il est plus approprié de déterminer "la taille" des ensembles de points partageant un même exposant, via la mesure de Hausdorff. On obtient ainsi le spectre multifractal d'une fonction, qui caractérise en particulier sa nature monofractale ou multifractale.

La première partie de ce travail se penche sur la méthode dite des "coefficients d'ondelettes dominants" (WLM), récemment développée dans le contexte de l'analyse multifractale, et a pour objectif sa mise en application à des situations concrètes en géosciences. Nous présentons d'abord la WLM et insistons particulièrement sur les différences majeures entre théorie et pratique, tant au niveau de l'utilisation de la méthode qu'au niveau de l'interprétation des résultats. Nous montrons ensuite que la WLM s'avère être un outil d'analyse performant pour l'étude de la topographie de la surface de la planète Mars d'un point de vue unidimensionnel et bidimensionnel; la première approche permettant de récupérer des informations cohérentes avec de précédents travaux, la seconde étant inédite et mettant en évidence certaines zones d'intérêt de Mars. Ensuite, nous étudions la régularité de signaux de température relatifs à diverses stations climatiques réparties en Europe. Dans un premier temps, nous montrons que la WLM permet de détecter une corrélation forte avec les anomalies de pression. Nous montrons alors que les exposants de Hölder obtenus sont directement liés au climat sous-jacent et nous établissons des critères qui les mettent en parallèle avec leurs caractéristiques climatiques telles que définies par la classification de Köppen-Geiger.

D'autre part, la version continue de la transformée en ondelettes (CWT), développée dans le cadre de l'analyse temps-fréquence, est également étudiée dans ce travail. Le but poursuivi ici est la détermination de périodes dominantes et l'extraction des composantes oscillantes associées qui constituent un signal donné. La CWT permet, contrairement à la transformée de Fourier, d'obtenir une représentation en temps et en fréquence du signal considéré, ce qui ouvre donc de nouvelles perspectives d'analyse. En outre, avec une ondelette de type Morlet, une formule de reconstruction simple peut être utilisée lors de l'extraction d'une composante.

Ainsi, la seconde partie du manuscrit présente la CWT et se concentre principalement sur les effets de bords inhérents à cette technique. Nous illustrons les avantages du "zero-padding" et introduisons une méthode itérative permettant d'atténuer significativement les erreurs de reconstruction aux bords des signaux. Ensuite, nous étudions en détail le signal ENSO (El Niño Southern Oscillation) relatif aux anomalies de températures de l'Océan Pacifique et responsable d'événements climatiques extrêmes appelés El Niño (EN) et La Niña (LN). Grâce à la CWT, nous en distinguons les principales périodes et en extrayons les composantes dominantes, qui sont d'ailleurs le reflet de mécanismes géophysiques connus. Une étude minutieuse de ces composantes nous permet d'élaborer un algorithme de prédiction à plus d'un an des événements EN et LN, ce qui constitue une meilleure performance que les modèles actuels. Enfin, nous généralisons la méthode d'extraction des composantes utilisée jusqu'alors en développant une procédure qui détecte des crêtes dans la CWT. L'algorithme, nommé WIME (Wavelet-Induced Mode Extraction), est illustré sur plusieurs exemples hautement non-stationnaires. Ses capacités à récupérer des composantes connues hors d'un signal donné sont testées et comparées à l'Empirical Mode Decomposition. Il apparaît que WIME dispose d'une meilleure adaptabilité dans diverses situations. Nous montrons finalement que WIME peut être appliqué à des situations réelles comme un électrocardiogramme ou encore le signal ENSO.

# Acknowledgements

I would like to express my gratitude to all the people who contributed to the incredible experience this thesis has been. First and foremost, I would like to thank Samuel Nicolay for his unreserved support during the last four years. He has been an amazing boss, team leader, coach, colleague, collaborator, guide and friend during this journey. He was always motivated and incited me to explore new horizons, which led me to discover thrilling research areas. He allowed me to carry out this work, to meet great people and gave me a lot of freedom to study the subjects that I wanted to investigate. His energy and determination really fueled my work.

Then, I would like to thank Alain Arneodo and Patrick Flandrin for having accepted to be the "foreign experts" of my jury. I feel privileged and honored of their interest in my research. Besides, they both allowed me to advance in my thesis at several occasions. Alain provided excellent comments and suggestions for my papers on multifractal analysis; Patrick helped me for the time-frequency part and enabled me to participate to its summer school in Peyresq, which was definitely a memorable experience. I hope to have the opportunity to collaborate with them in a near future.

I also thank Françoise Bastin, Xavier Fettweis and Georges Mabille for having accepted to be the "local experts" of my jury. It has been a pleasure to discuss with Xavier and Georges about my research on temperatures and El Niño. Their feedback and their ideas, along with those of Michel Erpicum, certainly contributed to several results presented in the manuscript. In the same spirit, I thank all the professors in the Math department who made this thesis possible.

Besides, I thank Desislava Petrova and Joan Ballester, from the IC3 team of Barcelona, for their excellent advice on El Niño analysis. The few discussions we had were particularly fruitful and will hopefully lead to further developments in El Niño predictions.

Special thank to the MT180 team, especially Evelyne Favart, who accompanied me through all the steps of the competition and allowed me to get more involved in MT180! This challenge was exciting and I am glad that it represents a part of my PhD life.

This adventure wouldn't have been the same without my colleagues and friends Céline and Thomas, with whom I have unforgettable memories in a few conferences. Working and traveling with them was a real delight. I also had the chance to have entertaining lunch breaks with my friends Julien, Laurent, Loïc, Émilie, among others. I will miss playing whist with them!

Of course, I thank my parents Claudine and Félix for their unconditional support throughout these years. Math is not their cup of tea and even though they admit they do not really understand what I am doing, they have always believed in me and have done everything they could to help me. The same goes for my sister Marine, my cousins Bruno and Marc, and my friends Adrien and Pierre.

Christelle, I am sure you are at least as happy as I am that this thesis is over. Thank you for your support during the last couple of years, you are the best!

Finally, I would like to thank the FNRS for funding my research. It allowed me to travel a lot and to meet a lot of interesting people. I hope that many promising bright math students will have the chance to live a wonderful experience thanks to similar research grants.

# Contents

# Introduction

Nature holds many secrets that humans have been trying to unveil through ages, which eventually led to numerous scientific breakthroughs. These discoveries were often the result of meticulous studies of natural phenomena, starting with careful observations and ending with the modeling of the underlying distinct processes. Such dissections of apparently complex problems into simpler principles and equations are at the basis of the most famous theories ever created, such as Newton's laws of classical mechanics, Mendel's laws of heredity or Bohr and Chadwick's atomic model. They all managed to identify the ingredients explaining why and how a part of nature actually works. In mathematical analysis, a groundbreaking discovery of at least the same importance can be attributed to the French genius Joseph Fourier in 1822 with his theory of decomposition of a given function into trigonometric series [56]. This tool allows to rewrite functions in terms of utterly simple "building blocks" composed of sine and cosine functions, which can be assimilated to the various atoms forming a molecule. Moreover, the associated Fourier spectrum provides a brand new type of information: the spectral content of a signal, i.e. the proportion of energy in a signal that can be imputed to a given frequency. The implications of the masterpiece proposed by Fourier, coupled with the development of computer science, are now beyond the sole world of mathematics or even physics[1]: his method has become an unmissable tool for every scientist. In the 1890's, Henri Poincaré even wrote[2]: "Fourier's Analytic Theory of Heat is one of the first examples of application of analysis to physics [...]. The results he obtained are certainly interesting by themselves, but what is even more interesting is the method he used to obtain them, which will always serve as a model for anyone desirous of cultivating some branch of

[1] Fourier developed his theory while working on heat equations.

[2] "La Théorie de la Chaleur de Fourier est un des premiers exemples d'application de l'analyse à la physique [...]. Les résultats qu'il a obtenus sont certes intéressants par eux-mêmes, mais ce qui l'est plus encore est la méthode qu'il a employée pour y parvenir et qui servira toujours de modèle à tous ceux qui voudront cultiver une branche quelconque de la physique mathématique. [...] Le livre de Fourier a une importance capitale dans l'histoire des mathématiques." [32, 119].

mathematical physics. [...] Fourier's book is of paramount importance in the history of mathematics."[32, 119].

Despite its unquestionable usefulness, the Fourier transform has a non-negligible flaw: the loss of temporal information. In other words, it could be used as a way to detect which notes are played in a song but not when they are played. Mathematically speaking, this says that the Fourier transforms of e.g.

$$f_1(x) = \cos(2\pi x)\chi_{[0,10]}(x) + \cos(4\pi x)\chi_{[10,20]}(x)$$

and

$$f_2(x) = \cos(4\pi x)\chi_{[0,10]}(x) + \cos(2\pi x)\chi_{[10,20]}(x)$$

allow to determine the two frequencies present in $f_1$ and $f_2$ but not which one appeared first in each function. This problem shows that the transition from the time domain to the frequency domain is somehow a bit rude. It would thus be opportune to find a way to decompose a function $f$ in a Fourier-like spirit that can still give its spectral content while keeping the possibility to identify the appearance of regime shifts or the presence of short-lived components. Nevertheless, it is not possible to obtain a perfect accuracy on both sides because time and frequency compete with each other and are regulated by uncertainty principles comparable to Heisenberg's inequality in quantum mechanics. Whatever the methods developed, it is thus necessary to make a trade-off between these two dimensions. Besides, it can be felt that there is a need to visualize the result of the analysis in a time-frequency plane, like an image that displays the interactions between time and frequency, which is infeasible with the Fourier transform. In this spirit, when a local study of $f$ at a given time $t$ and frequency $a$ is performed, it seems reasonable to give more weight to the values of $f$ closer to $t$, and the size of the window around $t$ through which $f$ is examined should be inversely proportional to $a$. This necessity to adapt the window as a function of the frequency is nicely summed up in the following citation of Norbert Wiener in [152]: "A fast jig on the lowest register of an organ is in fact not so much bad music but no music at all."[3] That being said, a complete analysis of $f$ would thus require convolutions of $f$ with translations and expansions/contractions of an analyzing modulated function. The wavelet transform naturally emerges.

Even though the first "wavelet" is generally attributed to Alfred Haar in 1909 [65], it is commonly admitted that Hungarian Dennis Gabor introduced the first wavelet as described above, in 1946 [59]. The translations and expansions of his Gabor functions were often called the "Gabor atoms". These atoms were thus used as new building blocks of signals, allowing to extract sharp information from a time-frequency point of view. The term "wavelet" (derived from the French word "ondelette") appeared later,

[3]En français, la formulation de Patrick Flandrin est tout aussi élégante: "Une note, pour être percue comme telle, doit être tenue d'autant plus longtemps qu'elle est plus grave." [52].

in 1984, with the seminal works of Jean Morlet and Alex(ander) Grossmann [63]. In 1986, Pierre Gilles Lemarié and Yves Meyer unify the results related to wavelets and by doing so, they literally establish the first cornerstone of wavelet theory [93]. This golden age is then enriched by the contributions of Stéphane Mallat [96, 97], Ingrid Daubechies [34] and Yves Meyer [100, 101] amongst others, who consolidate the first generation of works on wavelets and mark the starting point of a new era in signal analysis. Since then, wavelets have proliferated and diversified in their shapes and uses[4] so that they are now prominent stakeholders in distinct branches of signal analysis[5]. One of them is naturally time-frequency analysis, in which the continuous wavelet transform with Morlet-like wavelets kept on expanding with its original objectives in focus: providing a time-frequency representation of a signal and allowing the extraction of its elemental building blocks. In the literature, this direction was followed by e.g. Flandrin [53, 54], Cohen [30], Mallat [98]; half of this thesis integrates in this vein as well. On the other hand, some fields of research have been hugely influenced by the discrete version of the wavelet transform[6]. Indeed, this one led for instance to the development of image compression standards (JPEG 2000), multiresolution analysis and multifractal analysis [34, 96, 100].

This last example, namely multifractal analysis, has become a widespread tool in the analysis of the irregularity of geophysical signals and images. As mentioned, some methods based on wavelets have been designed, but other particularly popular algorithms also exist, which reinforces our motivation to show that wavelets are an excellent choice in that context. Multifractal analysis thus naturally establishes itself as an important subject that has to be studied in the present work. Therefore, let us now have a deeper look at the origins of this other thrilling wavelet-impacted area.

It all begins by the following question:"Is every continuous function differentiable except on a set of isolated points?" This could have been one of the most treacherous questions to ask mathematicians in the 19th century. At the time, mathematics was mostly used as a tool to describe the laws of physics and was thus inspired by nature. Rather than dealing with abstract and intangible concepts, it generally had to be intuitive and geometrically interpretable. Therefore, the instinctive answer to the question was an uncontested "yes", which was even supported by the "proof" provided by eminent French scientist André-Marie Ampère in 1806 [9]. Its argument relied on the "obvious" fact that a continuous curve had to have some sections on which it was either increasing, decreasing or constant and thus allowing the computation of a derivative. From the

[4]A non-exhaustive -but long- list with the description of hundreds of wavelets can be found in [45].

[5]Yves Meyer was even awarded the 2017 Abel Prize for his lifelong work on wavelets.

[6]Or sometimes by both the continuous and the discrete wavelet transforms, e.g. multifractal analysis.

parabolic trajectory of a cannonball to the elliptic motions of planets, every physical phenomenon looked to comply with the theorem and no exception seemed to lurk in the apparently soft world of continuous functions.

In 1872, Karl Weierstrass, a German mathematician not satisfied with Ampere's vague claims, presented at the Academy of Science in Berlin a work that would soon take the world by storm and lead to a revolution in mathematics. He constructed a special family of functions (using Fourier-like series) that were continuous everywhere but nowhere differentiable [144, 145]. By doing so, Weierstrass had literally released monsters in a mathematical realm which was not necessarily ready for such a cataclysm; this would trigger intense debates on the usefulness of such unnatural objects among specialists. For example, in 1893, Charles Hermite wrote to Thomas Stieltjes *"I turn with terror and horror from this lamentable scourge of functions with no derivatives"*([68, 118]). In 1908, his fellow-countryman Henri Poincaré wrote:[7] *"Logic sometimes engenders monsters. Masses of strange functions emerged and seemed to endeavor to look as little as possible to the honest functions that are of some use. No more continuity, or continuity but no derivatives[...] In the past, when a new function was invented, it was with practical perspectives; nowadays, they are invented on purpose to show our ancestors' reasoning is at fault, and we shall never get anything more out of them."*[120]. Since then, many such counter-intuitive functions have been constructed and studied by renowned mathematicians of the 19th and 20th century, e.g. Darboux, Peano, Hilbert, Takagi, Banach,... ([138]). The stunning diversity of that type of functions raises a problem in which the other half of the present work find its roots: the characterization of their irregularity[8].

While the function $f_\theta : x \mapsto |x|^\theta$ is not differentiable at 0 for $0 < \theta \leq 1$, one can feel that $f_\theta$ becomes "smoother" at 0 as $\theta$ increases. In this case, $\theta$ can be seen as the parameter that characterizes the regularity of $f_\theta$ at 0. Continuous but nowhere differentiable functions are much more complicated since they display singularities everywhere. Nevertheless, there is no reason to doubt that characterizing them in a similar way is possible. For that purpose, the notion of Hölder exponent is commonly used, which is initially designed to quantify the pointwise regularity of a function. In the case of the Weierstrass function, it appears that each point displays the same Hölder exponent, which makes it belong to the class of the "regularly irregular" monoHölder functions. Even if the sole

[7] Originally: *"La logique parfois engendre des monstres. On vit surgir toute une foule de fonctions bizarres qui semblaient s'efforcer de ressembler aussi peu que possible aux honnêtes fonctions qui servent à quelque chose. Plus de continuité, ou bien de la continuité, mais pas de dérivées[...] Autrefois, quand on inventait une fonction nouvelle, c'était en vue de quelque but pratique ; aujourd'hui, on les invente tout exprès pour mettre en défaut les raisonnements de nos pères, et on n'en tirera jamais que cela."*

[8] The interested reader can find much more information about the fascinating story of continuous but nowhere differentiable functions in [138] and in the nice all-audiences article [89].

Hölder exponent associated with a monoHölder function may allow a first distinction between some of the beasts that once troubled mathematicians, it is not sufficient to fully characterize the others, the so-called multiHölder ones ([4, 147]). Besides, the computation of the Hölder exponent at each point might turn out overly difficult and even useless since it may change radically from point to point. For these reasons, it becomes clear that it would be preferable to obtain some kind of distribution of the Hölder exponents that can be found within a function. This concept, properly called *spectrum of singularities* or *multifractal spectrum*, is theorized as the application that computes, for a given Hölder exponent $h$, the Hausdorff dimension of the sets of points having $h$ as exponent. In other words, it "measures the size" of the so-called iso-Hölder sets, which gives it the expected distribution-like interpretation. With these considerations taken into account, the functions for which the support of the spectrum of singularities is reduced to a singleton are called *monofractal* (they include the monoHölder ones) while the others are termed *multifractal* (these are multiHölder).

Mathematicians are thus confronted with another difficult task: the determination of the spectrum of singularities of a given function. Even if the problem can often be tackled from the definitions in the case of theoretical examples, numerical methods involving stable and computable quantities have to be developed for real-life signals. These algorithms designed to study the fractal nature of an object are called *multifractal formalisms* and first emerged in the world of physics, more precisely in the context of turbulence ([11, 57]). In the 1940's, Russian mathematician Andreï Kolmogorov hypothesized that the structure function (moments of variations of velocity in a fluid) follows a linear power-law of the increments [22]. While the statement has since been proven wrong in a general framework, it paved the way for the modern understanding and analysis of turbulent flows. Giorgio Parisi and Uriel Frisch reflected on the concepts presented by Kolmogorov and suggested that a nonlinear dependence was the signature of different types of singularities in the fluid. As a result, they presented the Frisch-Parisi conjecture [114], a multifractal formalism based on the computation of a structure function which was linked with the spectrum of singularities by heuristic arguments and a Legendre transform. This pioneering technique had some limitations though, such as the fact that only the strongest singularities contribute to the process ([13, 19, 103]). Among its numerous successors is the class of wavelet-based multifractal formalisms, which appeared in the 1990's and are still being developed. Over the years, two main wavelet-based methods have been extensively studied and used in practice. The first one, mostly developed at the instigation of Alain Arneodo, uses the continuous wavelet transform and is called wavelet transform modulus maxima (WTMM) ([13, 19, 103]). The other one, mainly deepened by Stéphane Jaffard, relies on a discrete wavelet transform ([2, 98]) and is termed wavelet leaders method (WLM) ([73, 75, 148, 151]). In this work, we chose to use the WLM over the WTMM for several reasons: it borrows ideas from both the Frisch-Parisi and the WTMM formalisms while being computationally

faster, it has a strong mathematical background, it is easy to implement and to generalize to real-valued functions of $n$ variables.

It can be easily deduced from the outline presented so far that this thesis is organized in two parts: one about time-frequency analysis based on the continuous wavelet transform and the other one about multifractal analysis with the WLM. Contrary to this introduction, we decided to invert these two parts in the following. They could be reversed with only minor modifications, but such a choice has been guided by a few reasons. First, from a pedagogical point of view, it is more convenient to present the large amount of mathematical notions and properties required for multifractal analysis all at once. Since some of them involve results about wavelets, we judged best suited to introduce these in that part as well, which somehow forces multifractal analysis to be presented first. Moreover, from a chronological point of view, multifractal analysis is actually the first subject that we investigated, it thus seemed more natural to start with it as it is more comprehensive and completed. Regarding time-frequency analysis, we got involved with it almost one year and a half later and this subject was new to us at that time. Adding to the fact that we are still actively working on some related projects, this explains why that part is presented in second place and leaves several open doors. As a consequence, the structure of the manuscript is the following.

The first part deals with multifractal analysis through the WLM. In chapter 1, we present the mathematical concepts involved in the WLM: Hölder exponent, Hausdorff dimension and wavelet leaders. Then, we develop the WLM and illustrate it with a theoretical example. A large part of the chapter is dedicated to the explanation of the differences between theory and practice and how to properly interpret the results. Chapter 2 is devoted to a direct application of the WLM in geosciences, namely the study of the fractal nature of Mars topography. We conduct an extensive analysis of its Hölder regularity in several ways (one-dimensional, two-dimensional, small scales, large scales) and relate some of the results to particular features of the planet. Chapter 3 consists in another application of the WLM: the study of the surface air temperature variability in Europe. However, in this case, we take a closer look at the values of the Hölder exponents by examining their connection with pressure anomalies. We also show that these exponents can be used to characterize the climate type of the corresponding regions in a way which is consistent with the Köppen-Geiger climate classification. The chapter ends with a discussion of the results and possible future works.

The second part is organized in the same way as the first part. Chapter 4 introduces and exemplifies the continuous wavelet transform (CWT) with Morlet-like wavelets and the representation of the signal in the time-frequency plane. Special attention is given to border effects, which are inherent to the use of the CWT with finite signals. Then, chapter 5 is devoted to the study of the El Niño climate index related to temperature

anomalies in the Equatorial Pacific Ocean. This signal is analyzed with the CWT in order to extract the main periods and components. We develop a method based on these components that allows to predict the evolution of the curve more than one year ahead, which is a benchmark that current models do not seem to be able to achieve. Finally, chapter 6 is somehow a generalization of the extraction technique used thus far. We formulate an algorithm named WIME (for Wavelet-Induced Mode Extraction) that captures the highly nonstationary behavior of test signals. Its skills are tested in several ways and compared with another method: the Empirical Mode Decomposition. The manuscript ends with a conclusion that goes over the major points exposed in the six chapters.

# Part I

# Wavelet-based multifractal analysis

# Chapter 1

# Mathematical tools and wavelet leaders method

This chapter presents the mathematical notions and tools orbiting the wavelet leaders method (WLM) used in chapter 2 and chapter 3. Since this thesis is oriented towards the practical aspect of wavelet-based methods for natural data analyses, the theoretic part is intentionally reduced to the necessary minimum; the reader interested in the technical details is invited to consult the references given throughout the sections. Besides, we do not intend to rewrite the complete story and development of the WLM. This has already been done impeccably in several excellent theses and we can only recommend to go through [47, 91, 147] for more information on that subject.

## 1.1 Hölder exponent

**Definition 1.1.1.** Let $f : \mathbb{R}^n \to \mathbb{R}$ be a locally bounded function, $x_0 \in \mathbb{R}^n$ and $\alpha \geq 0$; $f$ belongs to the *Hölder space* $C^\alpha(x_0)$ if there exist a polynomial $P$ of degree strictly inferior to $\alpha$, a constant $C > 0$ and a neighborhood $V$ of $x_0$ such that

$$|f(x) - P(x - x_0)| \leq C|x - x_0|^\alpha \quad \forall x \in V.$$

**Remarks 1.1.2.** The restriction to locally bounded functions holds for the rest of the chapter. It can be shown that, if $f \in C^\alpha(x_0)$, then the polynomial $P$ in the previous definition is unique and, if $f$ is $\lfloor \alpha \rfloor$ continuously differentiable on a neighborhood of $x_0$, then $P$ corresponds to the Taylor polynomial of $f$ at order $\lfloor \alpha \rfloor$ ($\alpha - 1$ if $\alpha \in \mathbb{N}$). However, the differentiability at $x_0$ is not guaranteed if $f \in C^1(x_0)$ as shown by $f : \mathbb{R} \to \mathbb{R} : x \mapsto |x|$

and $x_0 = 0$. In the frequent case where $0 < \alpha \leq 1$, $P$ boils down to $f(x_0)$, which leads to the following definition.

**Definition 1.1.3.** Let $f : \mathbb{R}^n \to \mathbb{R}$ be a locally bounded function; $f$ is said *uniformly Hölder* if there exist $0 < \epsilon \leq 1$ and $C > 0$ such that

$$|f(x) - f(y)| \leq C|x - y|^\epsilon \quad \forall x, y \in \mathbb{R}^n.$$

This somehow vague definition is handy and sufficient when it is only required that $f$ is "just a bit more than continuous" (see section 1.3).

The Hölder spaces are embedded, i.e. $C^\alpha(x_0) \subseteq C^{\alpha'}(x_0)$ if $\alpha' \leq \alpha$. A notion of regularity of $f$ at $x_0$ is thus given by the "highest exponent" $\alpha$ such that $f$ belongs to $C^\alpha(x_0)$.

**Definition 1.1.4.** The *Hölder exponent* of a function $f$ at $x_0$ is defined as

$$h_f(x_0) = \sup\{\alpha \geq 0 : f \in C^\alpha(x_0)\}.$$

**Remarks 1.1.5.** Although the Hölder exponent is mainly used for the characterization of "irregularities" in $f$ and thus is generally finite, its definition can lead to $h_f(x_0) = +\infty$. Therefore, $h_f$ can be viewed as a function with values in $[0, +\infty]$:

$$h_f : \mathbb{R}^n \to [0, +\infty] : x \mapsto h_f(x).$$

For example, if

$$f_\alpha : \mathbb{R} \to \mathbb{R} : x \mapsto |x|^\alpha$$

with $\alpha \geq 0$, then $h_{f_\alpha}(0) = \alpha$ if $\alpha$ is a non-integer real number or an odd integer and $h_{f_\alpha}(0) = +\infty$ if $\alpha$ is an even integer. Note that $f$ need not belong to $C^\alpha(x_0)$ to have $h_f(x_0) = \alpha$. Indeed, if $\alpha > 0$ and if one considers

$$f_1 : \mathbb{R} \to \mathbb{R} : x \mapsto |x|^\alpha \log |x|$$

and

$$f_2 : \mathbb{R} \to \mathbb{R} : x \mapsto |x|^\alpha \sin\left(\frac{1}{|x|}\right)$$

with $f_1(0) = 0 = f_2(0)$, then it turns out that $h_{f_1}(0) = \alpha = h_{f_2}(0)$ but $f_1 \notin C^\alpha(0)$ whereas $f_2 \in C^\alpha(0)$. These rather simple functions display only one so-called singularity (at 0) which is the only point with a finite Hölder exponent. Some functions have the same exponent at each point, others do not, which naturally gives the following definitions.

**Definition 1.1.6.** If there exists $H \in [0, +\infty]$ such that $h_f(x) = H \quad \forall x \in \mathbb{R}^n$, the function $f$ is said *monoHölder with Hölder exponent H*. Otherwise, if there exist $x_1, x_2 \in \mathbb{R}^n$ $(x_1 \neq x_2)$ such that $h_f(x_1) \neq h_f(x_2)$, then $f$ is said *multiHölder*.

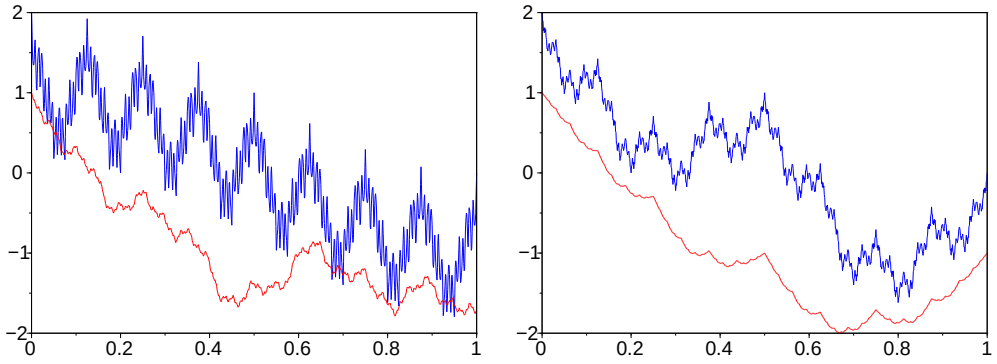


Figure 1.1: Weierstrass function $W_{a,b}$ on $[0,1]$ for $a = 0.5$ and $b = 16$ (left, blue), 4 (right, blue), $2^{4/3}$ (left, red), 2 (right, red). The functions plotted in red are shifted 1 unit downwards for the sake of clarity. The corresponding Hölder exponents are 0.25, 0.5, 0.75, 1.

**Remarks 1.1.7.** It is trivial to build monoHölder functions with exponent $H = +\infty$; the interesting question is about the existence of functions for which $h_f(x) < +\infty$ for all $x \in \mathbb{R}^n$ or at least for "large" sets of points. From a historical point of view, this issue actually emerged in the 19th century under the form: "Is every continuous function differentiable except on a set of isolated points?" At the time, this was commonly admitted to be true; Ampere even provided a "proof" of that claim [9]. However, in 1872, Weierstrass published the first example of a family of continuous functions nowhere differentiable [145][1]:

$$W_{a,b} : \mathbb{R} \to \mathbb{R} : x \mapsto \sum_{n=0}^{+\infty} a^n \cos(b^n \pi x)$$

where $a \in (0,1)$ and $b \in [1/a, +\infty)$. In 1916 [66], Hardy gave the first proof that the Weierstrass function is monoHölder with Hölder exponent

$$h_{W_{a,b}}(x) = -\log(a)/\log(b) \quad \forall x \in \mathbb{R}.$$

The function is plotted in Figure 1.1 for $a = 0.5$ and $b = 16, 4, 2^{4/3}, 2$, which gives Hölder exponents $H = 0.25, 0.5, 0.75, 1$ respectively. It can clearly be seen that the Hölder exponent is an appropriate measure of the regularity of a function since $W_{a,b}$ appears smoother as $H$ increases. The monoHölder nature of the function is also visible in the sense that, even though $W_{a,b}$ is irregular, it is actually "regularly irregular", i.e. all the points are singularities of the same nature, with the same Hölder exponent.

[1] Other mathematicians constructed such functions at the same period, e.g. Bolzano, Cellérier, Riemann (see [138]).

Computing the Hölder exponent of a function at a given point is often difficult in practice, if not impossible. Besides, it is usually more interesting to obtain global information about the pointwise regularity of $f$, i.e. some kind of "distribution" of the exponents, rather than the potentially erratic and numerically unstable function $h_f$. Therefore, even though the notions of monoHölder and multiHölder functions are defined in an intuitive and natural way, they are often supplanted by the concepts of *monofractal* and *multifractal* functions. These are detailed in the following but require more advanced mathematical tools first.

## 1.2 Hausdorff dimension

The classic topological dimension always being an integer number, it is not always sufficient to underline the properties of the sets considered or to make a distinction between them, even when they appear totally different. The Hausdorff dimension solves that problem because it generalizes the notion of dimension to non-integers. Its definition relies on the Hausdorff outer measure, defined as follows (see e.g. [50]).

**Definition 1.2.1.** Let $X \subset \mathbb{R}^n$ and $d \geq 0$. The *d-dimensional Hausdorff outer measure* of $X$ is defined as

$$\mathcal{H}^d(X) = \lim_{\epsilon \to 0} \inf \left\{ \sum_{r \in R} \operatorname{diam}(r)^d : R \in \mathcal{R}_\epsilon(X) \right\}$$

where $\mathcal{R}_\epsilon(X)$ denotes the set of all countable covers of $X$ by sets of diameter inferior to $\epsilon$.

**Proposition 1.2.2.** *Given a set $X \subset \mathbb{R}^n$, there exists a unique value $d^* \geq 0$ such that $\mathcal{H}^d(X) = +\infty$ if $0 \leq d < d^*$ and $\mathcal{H}^d(X) = 0$ if $d > d^*$.*

This allows to define the Hausdorff dimension of $X$.

**Definition 1.2.3.** *The Hausdorff dimension* of $X \subset \mathbb{R}^n$ is defined as

$$\dim_{\mathcal{H}}(X) = \inf\{d \geq 0 : \mathcal{H}^d(X) = 0\}.$$

Note that $\mathcal{H}^{\dim_{\mathcal{H}}(X)}(X)$ can be 0, $+\infty$ or any strictly positive number. Also, the convention $\dim_{\mathcal{H}}(\emptyset) = -\infty$ is often considered for easier technical uses. Some of the properties of the Hausdorff dimension are exposed below.

**Proposition 1.2.4.**

- *If $U \subset \mathbb{R}^n$ is a non-empty open set, then* $\dim_{\mathcal{H}}(U) = n$.
- *If $X \subset Y \subset \mathbb{R}^n$ then* $\dim_{\mathcal{H}}(X) \leq \dim_{\mathcal{H}}(Y) \leq n$.

- *If* $(X_j)_{j\in\mathbb{N}}$ *is a sequence of subsets of* $\mathbb{R}^n$*, then*

$$\dim_{\mathcal{H}}\left(\cup_{j\in\mathbb{N}}X_j\right) = \sup_{j\in\mathbb{N}}\{\dim_{\mathcal{H}}(X_j)\}$$

- *If* $X \subset \mathbb{R}^n$ *is countable, then* $\dim_{\mathcal{H}}(X) = 0$.

**Remarks 1.2.5.** The classic triadic Cantor set $C$ is a perfect example that shows the usefulness of the notion of Hausdorff dimension. It is possible to show that

$$\dim_{\mathcal{H}}(C) = \frac{\log(2)}{\log(3)} \text{ and } \mathcal{H}^{\dim_{\mathcal{H}}(C)}(C) = 1,$$

which illustrates the dimension at which it is possible to "measure" $C$. If one tries to "measure" it by counting its number of points, i.e. computing $\mathcal{H}^0(C)$, then one gets $+\infty$ since $C$ is uncountable ($C$ has the cardinality of the continuum). The next natural attempt would be to "measure" its length, i.e. computing $\mathcal{H}^1(C)$, in which case one gets 0 since $\mathcal{H}^1$ coincides with the Lebesgue measure $\mathcal{L}^1$ and $\mathcal{L}^1(C) = 0$. Besides, its topological dimension is also equal to 0. Therefore, the Hausdorff dimension of $C$ is somehow a "hybrid" way to measure $C$ and gives finer information regarding such a complex mathematical object.

We can now come back to the Hölder regularity of a function $f$. As mentioned, it is interesting to obtain a global characterization of the regularity of $f$ through a distribution-like function of its Hölder exponents. This can now be achieved with the spectrum of singularities of $f$, defined as follows.

**Definition 1.2.6.** The *spectrum of singularities* (or *singularity spectrum*) of a function $f$ defined on $\mathbb{R}^n$ is the function

$$d_f : h \in [0, +\infty] \mapsto \dim_{\mathcal{H}}\{x \in \mathbb{R}^n : h_f(x) = h\}.$$

In other words, $d_f(h)$ is the Hausdorff dimension of the set of points having $h$ as Hölder exponent (also called *iso-Hölder set of exponent* $h$).

The spectrum of singularities gives a straightforward glimpse on how regular $f$ is. It allows to define the notions of monofractal and multifractal functions in a natural way[2].

**Definition 1.2.7.** A function $f$ is *monofractal* with Hölder exponent $H$ if the support of its spectrum of singularities is reduced to $\{H\}$; $f$ is said *multifractal* otherwise.

**Remark 1.2.8.** Although the concepts monoHölder and monofractal are close and have a similar physical interpretation, they are not mathematically equivalent. The inclusions that always hold are that a monoHölder function is monofractal and a multifractal function is multiHölder. In the literature, the focus is generally on the mono/multifractal

[2]Let us note that slightly different definitions also exist in the literature.

nature of the functions or signals considered. This is due to the fact that several techniques have been developed to estimate the spectrum of singularities of a signal (e.g. [73, 76, 102, 114]). They bear the generic name of *multifractal formalisms*; among them is the wavelet leaders method introduced by Jaffard in [73], which is described in the following. This formalism has already been successfully applied in several scientific fields, such as fully developed turbulence ([92]), heart rate variability ([6]) or texture classification ([149]).

## 1.3 The wavelet leaders method in theory

### 1.3.1 Wavelet leaders

There seems to be no consensus in the literature on one unique definition of a wavelet. Nevertheless, the following conditions are amongst the most commonly used.

**Definition 1.3.1.** We say that $\psi : \mathbb{R} \to \mathbb{R}$ is a *wavelet* if $\psi \in L^1(\mathbb{R}) \cap L^2(\mathbb{R})$ and if $\psi$ satisfies the so-called admissibility condition

$$\int_{\mathbb{R}} \frac{|\hat{\psi}(\omega)|^2}{|\omega|} d\omega < +\infty,$$

where $\hat{\psi}$ denotes the Fourier transform of $\psi$.

**Remarks 1.3.2.** The admissibility condition forces $\psi$ to satisfy $\hat{\psi}(0) = 0$, i.e. $\int_{\mathbb{R}} \psi(x)dx = 0$. This indicates that $\psi$ has (at least) 1 vanishing moment, which makes $\psi$ orthogonal to polynomials of degree 0. In many situations, it is preferable to use wavelets that are orthogonal to all low-order polynomials. Therefore, it is generally required that $\psi$ has $M$ ($M \in \mathbb{N}$) vanishing moments, i.e. for each $m \in \mathbb{N}$ such that $m < M$, the function $x \mapsto x^m \psi(x)$ belongs to $L^1(\mathbb{R})$ and

$$\int_{\mathbb{R}} x^m \psi(x) dx = 0.$$

Let us add that $n$-dimensional wavelets are constructed using tensor products of 1-dimensional wavelets ([34, 98, 100]).

The multifractal properties of a function can be studied by decomposing it in an orthonormal wavelet basis of the space $L^2(\mathbb{R}^n)$. The usual procedure to construct such a basis comes from a multiresolution analysis of $L^2(\mathbb{R}^n)$. For more details on how this works and on the properties of these concepts, the reader is referred to [34, 96, 98, 100].

**Proposition 1.3.3.** *Under some general assumptions ([34, 98]), it is possible to build a wavelet $\phi$ and $2^n - 1$ wavelets $(\psi^{(i)})_{1 \leq i < 2^n}$ such that*

$$\{\phi(x-k) : k \in \mathbb{Z}^n\} \cup \{\psi^{(i)}(2^j x - k) : 1 \leq i < 2^n, k \in \mathbb{Z}^n, j \in \mathbb{N}\}$$

*form an orthogonal basis of* $L^2(\mathbb{R}^n)$*. Therefore, any function* $f \in L^2(\mathbb{R}^n)$ *can be decomposed as*

$$f(x) = \sum_{k\in\mathbb{Z}^n} C_k\phi(x-k) + \sum_{j\in\mathbb{N}}\sum_{k\in\mathbb{Z}^n}\sum_{1\le i<2^n} c_{j,k}^{(i)}\psi^{(i)}(2^j x-k),$$

*where*

$$c_{j,k}^{(i)} = 2^{nj}\int_{\mathbb{R}^n} f(x)\psi^{(i)}(2^j x-k)\,dx$$

*and*

$$C_k = \int_{\mathbb{R}^n} f(x)\phi(x-k)\,dx.$$

**Remark 1.3.4.** The coefficients $c_{j,k}^{(i)}$ are called the wavelet coefficients of $f$. The index $i$ can be seen as the direction in which the function is analyzed. In $\mathbb{R}^n$, these directions are given by the $2^n-1$ vectors between the origin and the other vertices of the unit cube $[0,1)^n$. For a given scale $j$ ($j\in\mathbb{N}$) and position $k=(k_1,...,k_n)$ ($k\in\mathbb{Z}^n$), the wavelet coefficients $c_{j,k}^{(i)}$ ($1\le i<2^n$) are usually associated with the dyadic cube $\lambda_{j,k}$ of $\mathbb{R}^n$ defined as

$$\lambda_{j,k} = \left[\frac{k_1}{2^j},\frac{k_1+1}{2^j}\right)\times\ldots\times\left[\frac{k_n}{2^j},\frac{k_n+1}{2^j}\right).$$

In other words, it can be conveniently considered that $c_{j,k}^{(i)}$ lies in $\lambda_{j,k}$. These dyadic cubes allow an easy geometric visualization of the concepts of wavelet leaders related to a point and to a cube defined in the following.

**Definition 1.3.5.** The wavelet leader of $x_0\in\mathbb{R}^n$ at the scale $j$ is defined as

$$d_j(x_0) = \sup\left\{|c_{j',k'}^{(i)}| : \lambda_{j',k'}\subset 3\lambda_{j,k}(x_0), 1\le i<2^n\right\},$$

where $\lambda_{j,k}(x_0)$ is the unique dyadic cube at the scale $j$ containing $x_0$ and $3\lambda_{j,k}(x_0)$ is a three times enlarged version of $\lambda_{j,k}(x_0)$, i.e. it consists in the union of $\lambda_{j,k}(x_0)$ and its $3^n-1$ neighbors at scale $j$.

The wavelet leaders $(d_j(x_0))_{j\in\mathbb{N}}$ of $x_0$ are key quantities to study the pointwise regularity of $x_0$, as shown in the following theorem and its corollary ([39, 73, 87]).

**Theorem 1.3.6.** *Let* $f:\mathbb{R}^n\to\mathbb{R}$ *be a locally bounded function,* $x_0\in\mathbb{R}^n$ *and* $\alpha\ge 0$.

1. *If* $f$ *belongs to* $C^\alpha(x_0)$*, then there exist* $C>0$ *and* $J\in\mathbb{N}$ *such that*

$$d_j(x_0)\le C2^{-\alpha j}\ \forall j\ge J. \tag{1.1}$$

2. *Conversely, if there exist* $C>0$ *and* $J\in\mathbb{N}$ *such that inequality (1.1) holds and if* $f$ *is uniformly Hölder, then there exist a polynomial* $P$ *of degree strictly inferior to* $\alpha$*, a constant* $C'>0$ *and a neighborhood* $V$ *of* $x_0$ *such that*

$$|f(x)-P(x-x_0)|\le C'|x-x_0|^\alpha\log|x-x_0|\quad\forall x\in V. \tag{1.2}$$

**Corollary 1.3.7.** *If $f$ is uniformly Hölder, the Hölder exponent of $f$ at $x_0$ is given by*

$$h_f(x_0) = \liminf_{j \to +\infty} \frac{\log d_j(x_0)}{\log 2^{-j}}.$$

This result is the cornerstone of the wavelet leaders multifractal formalism. However, since we are interested in global quantities and not in the exact computation of the pointwise regularity, the definition of a wavelet leader has to be adapted so that it does not depend on a particular point anymore. Therefore, it is natural to associate wavelet leaders with the dyadic cubes of $\mathbb{R}^n$, which are independent of the function of interest.

**Definition 1.3.8.** The wavelet leader of $f$ associated with the cube $\lambda_{j,k}$ is the quantity

$$d_{j,k} = \sup \left\{ |c^{(i)}_{j',k'}| : \lambda_{j',k'} \subset 3\lambda_{j,k}, 1 \leq i < 2^n \right\},$$

where $3\lambda_{j,k}$ is again the set of cubes consisting of $\lambda_{j,k}$ and the $3^n - 1$ cubes surrounding $\lambda_{j,k}$ at scale $j$.

**Remarks 1.3.9.** The wavelet leaders of $f$ are always finite since the Cauchy–Schwarz inequality implies

$$|c_{j,k}| \leq C \, \|f\|_{L^2(\mathbb{R}^n)} \, \|\psi\|_{L^2(\mathbb{R}^n)}$$

for some positive constant $C$. A geometric view of the wavelet leader of a dyadic cube is represented in Figure 1.2 in the case $n = 2$ (an example in the case $n = 1$ is detailed in section 1.4). It can be seen that the wavelet leaders are hierarchical quantities and have a "vertical" structure, this contributes to the validity of the WLM described below. If $f$ has a strong singularity at some point, then its influence can be perceived through the scales, from the finer to the coarser. The wavelet leaders take this effect into account by considering the largest coefficients through the scales, which reinforces the impact of such singularities in the method and thus their characterization. In the same spirit, the fact of considering $3\lambda_{j,k}$ rather than simply $\lambda_{j,k}$ in definitions 1.3.5 and 1.3.8 allows to track down singularities more efficiently. The use of $3\lambda_{j,k}$ is also justified by the wavelet transform itself because, at the scale $j$ and position $k$, $\psi_{j,k}$ has most of its energy concentrated in $3\lambda_{j,k}$.

### 1.3.2 Wavelet leaders-based multifractal formalism

We now describe the $n$-dimensional wavelet leaders method (WLM) used to analyze the Hölder regularity of $n$-dimensional data. The WLM is somehow an adaptation of the box-counting method [58, 114] in the context of the discrete wavelet transform [73, 74, 75, 76]. It can also be seen as the discrete counterpart of the renowned wavelet transform modulus maxima (WTMM, see e.g. [10, 11, 102, 103]) which has been used successfully in many domains (see e.g. [12, 13, 14, 15, 37]). Even if one may think that

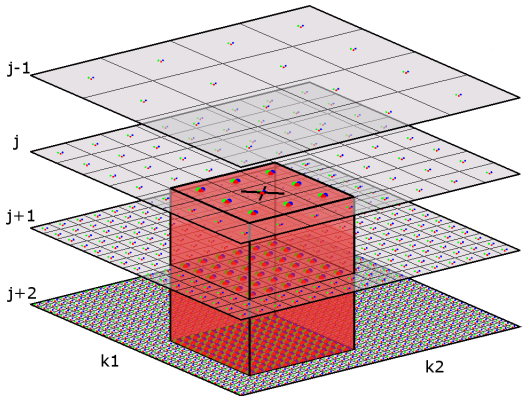


Figure 1.2: The wavelet leader of the dyadic cube $\lambda$ (dyadic square in 2D) marked by a black cross is the supremum of the modulus of the wavelet coefficients associated with the cubes in the red volume: $\lambda$, its 8 neighbors, and the cubes at finer scales that fit in these 9 cubes. There are 3 wavelet coefficients associated with each cube, indicated by the green, blue and red dots in each of them. Image borrowed from [147].

the WTMM provides more information than the WLM, there is no formal proof that one method is better suited for multifractal analyses than the other ([76]).

First, the structure function (or partition function) $S$ associated with the WLM is defined as

$$S(j,q) = 2^{-nj} \sum_k (d_{j,k})^q, \tag{1.3}$$

where the sum is restricted to the indices $k$ such that $d_{j,k} \neq 0$. Then, the scaling function $\eta$ is obtained as

$$\eta(q) = \liminf_{j \to +\infty} \frac{\log S(j,q)}{\log 2^{-j}} \tag{1.4}$$

and one can hope to obtain the spectrum of singularities as

$$d_f^{\eta}(h) = \inf_q \{hq - \eta_f(q)\} + n. \tag{1.5}$$

The heuristic arguments underpinning this method are the following ([73, 150]). First, by construction (equation (1.4)), $\eta$ is involved in the asymptotic behavior (as $j \to +\infty$) of the sum of the wavelet leaders:

$$\sum_k (d_{j,k})^q \sim 2^{(n-\eta(q))j}. \tag{1.6}$$

On the other hand, if $\lambda_{j,k}$ is a dyadic cube at the scale $j$ containing a point of Hölder exponent $h$, then theorem 1.3.6 states that $d_{j,k}$ should behave as $\sim 2^{-hj}$ for $j$ large enough and thus

$$(d_{j,k})^q \sim 2^{-hqj}.$$

Moreover, the iso-Hölder set of exponent $h$ can be covered by about $2^{d_f(h)j}$ cubes[3], which implies that the dominant behavior of the sum of the wavelet leaders should be

$$\sum_k (d_{j,k})^q \sim 2^{\sup_h\{d_f(h)-hq\}j}. \tag{1.7}$$

Comparing relations (1.6) and (1.7) gives

$$\sup_h\{d_f(h) - hq\} = n - \eta(q), \tag{1.8}$$

and a Legendre transform gives relation (1.5).

**Remarks 1.3.10.** Through equation (1.5), the WLM leads to a concave spectrum $d_f^\eta$ which is actually a tight upper bound for the true spectrum ([73, 75]):

$$d_f(h) \leq d_f^\eta(h).$$

In practice, $d_f^\eta$ is usually the only quantity numerically computable and is often interpreted as the spectrum of singularities $d_f$. Despite the fact that it is not possible to determine whether the equality holds or not, $d_f^\eta$ still provides valuable information. Indeed, it can be shown ([73, 75]) that $d_f^\eta$ is independent of the wavelet basis used throughout the formalism provided that the number of vanishing moments exceeds the supremum of the Hölder exponents found in the function. This condition is not really restrictive since wavelets can be chosen arbitrarily smooth. As a consequence, even though we only have $d_f(h) \leq d_f^\eta(h)$, the estimated spectrum $d_f^\eta$ contains information which is intrinsically linked with the Hölder regularity of $f$ and that can be used legitimately in data analysis. Moreover, even if the conditions under which this multifractal formalism holds (i.e. $d_f(h) = d_f^\eta(h)$) are still unclear, it has been shown that it yields exact results in many situations, including fractional Brownian motions, cascades and Lévy processes ([3, 18, 73, 74, 75, 150]).

## 1.4 The wavelet leaders method in practice

### 1.4.1 Application to a Brownian motion

The practical use of theoretical methods often needs complementary explanations and adjustments; the WLM does not contravene this principle. For that reason, this section is dedicated to a thorough exemplification of the WLM with a commonly used monofractal process, namely the Brownian motion. The wavelet used is the third order Daubechies wavelet ([34]) which has proven well-suited for multifractal analysis.

[3]Assuming that, in a practical case, the signal analyzed (of finite length) is defined on $[0, 1]$.

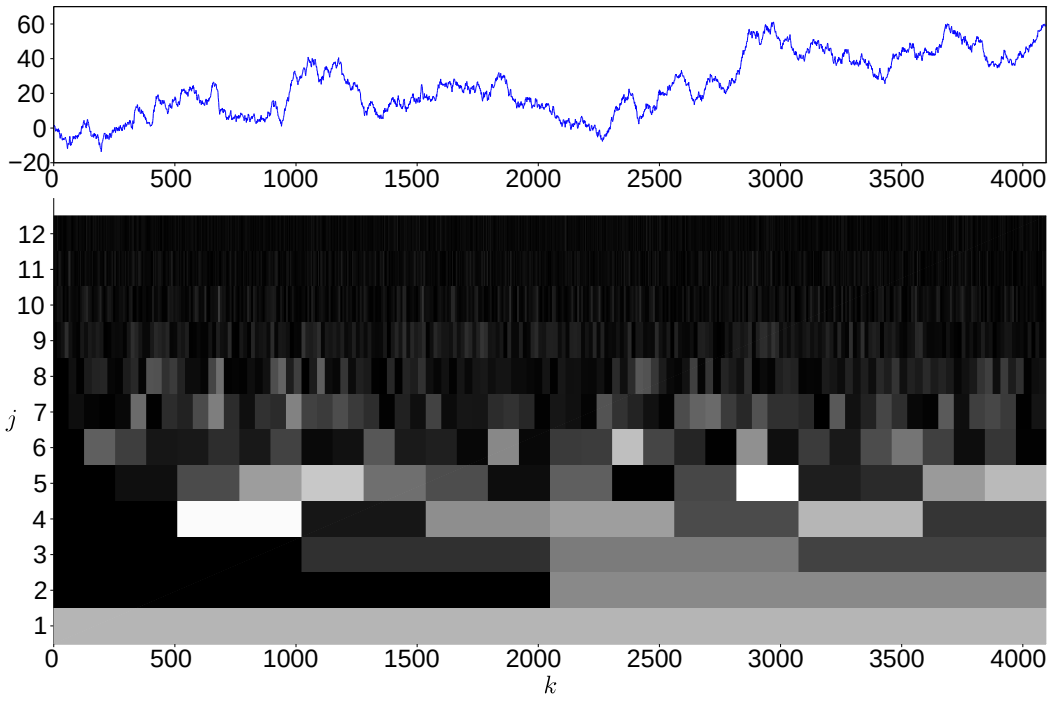


Figure 1.3: The Brownian motion studied as an example and the modulus of its discrete wavelet coefficients in the time-scale plane. The values range from 0 (black) to 10.2 (white).

The signal used in the present case is a classic Brownian motion which is monofractal with Hölder exponent $H = 0.5$ and which is made of $2^{12}$ data points. It is represented in Figure 1.3 with its discrete wavelet transform. The wavelet leaders corresponding to each dyadic interval are represented in Figure 1.4 and the time-scale plane is re-paved with them.

The structure function $S$ is computed and the function $j \mapsto \log_2(S(j,q))$ is represented in Figure 1.5 for several values of $q$. Even though the top left panel is consistent with the theory explained in this chapter, it is often displayed the other way round in the literature, as in the top right panel (where $j^* = 13 - j$). This is simply a question of vocabulary. The terminology used so far states that large scales $j \gg$ are more accurate in some sense since they eventually allow to characterize the regularity as $j \to +\infty$. However, as $j$ increases, the window through which the function is examined becomes smaller and smaller and thus comes the denomination "small scales" for the scales that are of real interest. From this point forward, we will give way to the customs of the scientific literature and the term small scales will relate to the scales of finest/highest resolution. In the same spirit, $j$ will actually stand for $j^*$.

The top right panel in Figure 1.5 illustrates how the scaling function $\eta$ is computed. Given $q$, $\eta(q)$ is obtained by performing a linear regression of $j \mapsto \log_2(S(j,q))$ on a

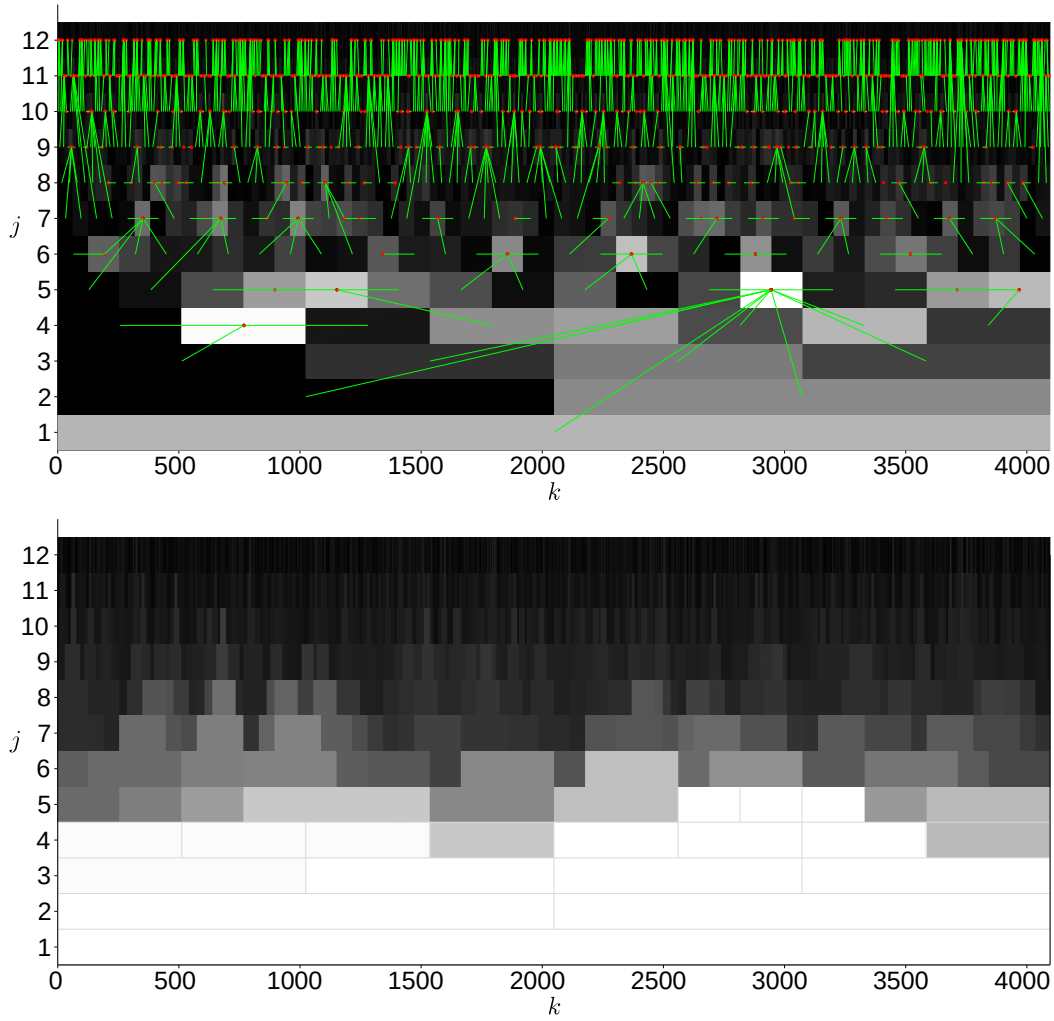


Figure 1.4: Top: Each dyadic interval is connected to its wavelet leader by a green line (excepted those at scale $j = 12$ for clarity). The intervals whose coefficient serves as wavelet leaders during the process are marked with a red star. Bottom: The time-scale representation of the DWT when the coefficients are replaced by their leader. This is the map used to compute the structure function $S(j, q)$.

range of small scales at which a scaling regime occurs, i.e. where $j \mapsto \log_2(S(j,q))$ is reasonably linear. The scaling function $\eta$ obtained this way is shown in the bottom left part of Figure 1.5. Since $\eta$ displays a remarkably linear behavior with slope 0.5, the associated spectrum $d_f^\eta$ is almost reduced to one point (see fourth plot) located at $(0.5, 1)$ which is the expected spectrum of singularities. Zooming in on that point indicates a slightly concave spectrum $d_f^\eta$, which was expected in a practical use of the WLM.

## 1.4.2 The WLM in practice: Important comments

### Removal of some scales

The elementary example presented in this section illustrates the basic functioning of the WLM. Despite its apparent simplicity, a certain number of important points can be discussed. First, the smallest scale $j = 1$ is rarely used in practice because the associated wavelet leaders are not hierarchical quantities as for the other scales. Indeed, it is impossible to envisage connecting them with wavelet coefficients at smaller scales as in Figure 1.4. Also, the computation roughly concerns the differences between two consecutive data points, thus the wavelet coefficients at that scale are often extremely close to zero so that numerical instabilities may occur when computing $S(1,q)$ for negative values of $q$. This explains why the first scale is not used to compute $\eta$. Also, as the scale grows, the number of wavelet coefficients available decreases exponentially. In order to compute sound means when building the structure function (equation (1.3)) and to prevent a handful of larger coefficients from controlling the whole process, it is advised to avoid the use of too large scales. In the present case, we stopped at the $7^{\text{th}}$ scale (see top right plot in Figure 1.5) because the next scale contains only 16 coefficients. By the way, the horizontal stabilization of the structure function in the top left plot in Figure 1.5 exposes perfectly the effect of a reduced number of coefficients.

### Choice of values of $q$

The range of the values of $q$ is subject to a careful choice. Indeed, the lowest (resp. highest) values of $q$ provide more weight to small (resp. large) wavelet leaders. Therefore, in the same spirit as stated above, considering extreme values of $q$ leads to an imbalance in equation (1.3) because only one abnormally small (or large) coefficient may take it all. The impact of such coefficients is weakened with larger datasets. Also, if the range is too restricted, then significant information may go missing and the spectrum might not be complete. Consequently, the choice of the values of $q$ is guided by the number of data points and the type of data to be analyzed. Since there is no consensus on a fixed range of values for the parameter $q$, experiments with the signals considered have to be carried out prior the proper analysis of the data. Nevertheless, in order to detect the possible increasing and decreasing parts in the spectra, it is recommended to use

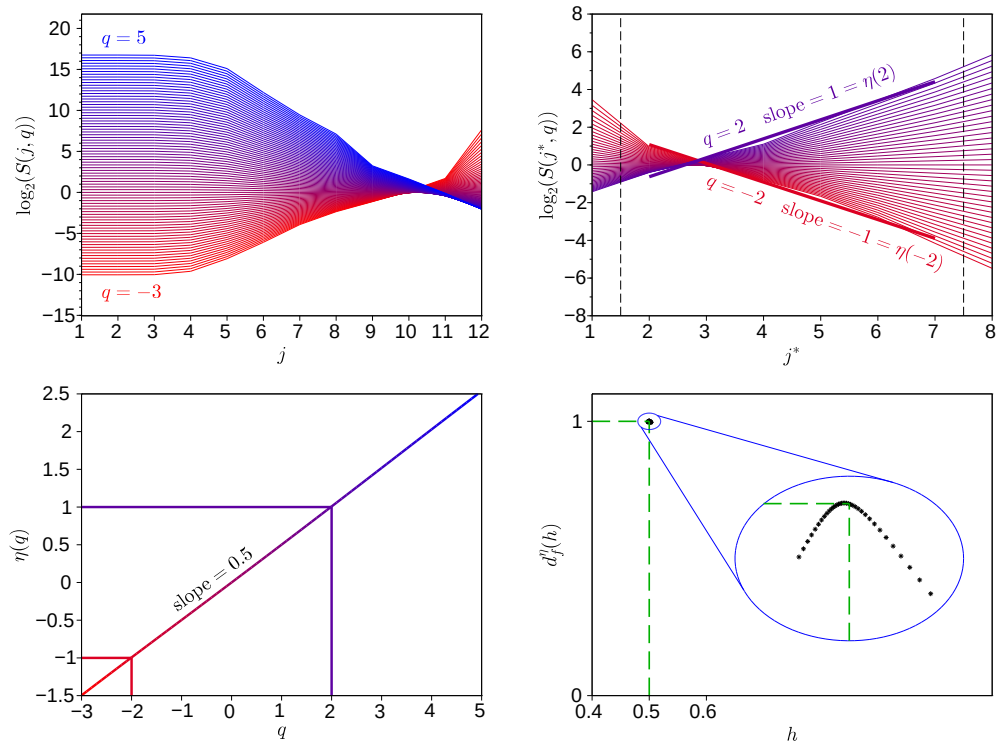


Figure 1.5: Steps of the WLM applied to the Brownian motion (with Hölder exponent 0.5). Top left: $j \mapsto \log_2(S(j,q))$ for $q$ ranging from -3 (red) to 5 (blue). Top right: $j^* \mapsto \log_2(S(j^*,q))$ with $j^* = 13 - j$ only at small scales (small values of $j^*$) and for $q$ ranging from -2 to 2 for the sake of clarity. This is a more common way to represent the structure function. It illustrates how the scaling function $\eta$ is obtained. Bottom left: Scaling function $q \mapsto \eta(q)$. Its linear behavior indicates that the signal is monofractal, with Hölder exponent given by the slope of $\eta$. Bottom right: the estimated spectrum of singularities $h \mapsto d_f^\eta(h)$, which is almost reduced to the point $(0.5, 1)$ as expected. Its concave shape is due to the use of a Legendre transform.

negative and positive values of $q$.

### Focusing on $\eta$ rather than $d_f^\eta$

From a practical aspect, the function $\eta$ already contains most of the information useful for the practitioner. A linear function $\eta$ is the signature of a monofractal signal and the slope of $\eta$ coincides with the Hölder exponent of the signal (i.e. the support of the spectrum) and characterizes its irregularity. Indeed, if we consider[4] $\eta(q) = c_1 q$, then

$$\begin{aligned} d_f^\eta(h) &= \inf_q \{hq - c_1 q\} + n \\ &= \begin{cases} n & \text{if } h = c_1 \\ -\infty & \text{otherwise.} \end{cases} \end{aligned}$$

On the other hand, a nonlinear $\eta$ indicates a multifractal behavior. If $\eta$ is of the form $\eta(q) = c_1 q - c_2 q^2$ (with $c_2 > 0$), then the estimated spectrum is

$$\begin{aligned} d_f^\eta(h) &= \inf_q \{hq - c_1 q + c_2 q^2\} + n \\ &= \frac{-(h - c_1)^2}{4c_2} + n. \end{aligned}$$

In both cases the maximum of $d_f^\eta$ is located at $(c_1, n)$ and since $d_f(h) \leq d_f^\eta(h) \leq n$, it turns out that "the most frequent" Hölder exponent in the signal can be obtained as the first order coefficient $c_1$ associated with $\eta$, regardless of its linearity. This could have been seen the other way round: if the expected spectrum $d_f$ is of the form $d_f(h) = -d_2 h^2 + d_1 h + d_0$ with $d_2 > 0$ and its maximum is located at $(H, n)$, then an inverse Legendre transform gives

$$\sup_h \{-d_2 h^2 + d_1 h + d_0 - qh\} = n - \left( Hq - \frac{q^2}{4d_2} \right)$$

and the same conclusion arises as seen to equation (1.8).

This remark is an interesting point since in practice $\eta$ is never perfectly linear but can be accurately approximated with a second-order polynomial of the form $c_1 q - c_2 q^2$. In that case, the focus is on the parameters $c_1$ and $c_2$ as in e.g.[11, 44, 151]. Similarly, $d_f^\eta$ can never be perfectly reduced to a single point, which is problematic to classify monofractal signals as such. However, a coefficient $c_2$ close to zero (or any other indicator of a linear behavior of $\eta$) suggests that the signal has a near-monofractal nature. As for the values of $q$, no consensus on a threshold for $c_2$ or on another method has been established to firmly decide when a given signal is monofractal or not; this may differ from one work to another. As a consequence, when the spectrum of singularities is not the primary objective of the study, it is common to abandon the computation of $d_f^\eta$ in favor of an analysis of $\eta$.

[4] Note that $S(j, 0)$ is the $0^{\text{th}}$-order moment of the wavelet leaders, giving $S(j, 0) = 1$ and thus $\eta(0) = 0$.

### Estimation of the multifractal parameters

The coefficients $c_1$ and $c_2$ of the present example are estimated via a least-square polynomial fitting of $\eta$ with the constraint of vanishing at 0. A regression of the type $f(x) = c_1 x$ of a set of points $(x_i, y_i)_i$ gives

$$c_1 = \frac{\sum_i x_i y_i}{\sum_i x_i^2}. \tag{1.9}$$

In this case we get $c_1 = 0.5051$, which is very close to the theoretical value 0.5. A least-square second-order fit of the type $f(x) = c_1 x - c_2 x^2$ leads to

$$c_1 = \frac{\sum_i x_i^4 \sum_i x_i y_i - \sum_i x_i^3 \sum_i x_i^2 y_i}{\sum_i x_i^4 \sum_i x_i^2 - \left(\sum_i x_i^3\right)^2} \tag{1.10}$$

and

$$c_2 = \frac{\sum_i x_i^3 \sum_i x_i y_i - \sum_i x_i^2 \sum_i x_i^2 y_i}{\sum_i x_i^4 \sum_i x_i^2 - \left(\sum_i x_i^3\right)^2}. \tag{1.11}$$

Note that the denominator in equations (1.10) and (1.11) never vanishes in practice; this is clearer when it is rearranged as

$$\sum_i x_i^4 \sum_i x_i^2 - \left(\sum_i x_i^3\right)^2 = \sum_{\substack{i,j \\ i \neq j}} x_i^2 x_j^2 (x_i - x_j)^2.$$

With these equations we get $c_1 = 0.5011$ which matches again almost perfectly the expected value 0.5, and $c_2 = 0.0015$ which is extremely close to 0 as awaited. Another natural indicator of the linear behavior of $\eta$ is the Pearson correlation coefficient (PCC):

$$\mathrm{PCC} = \frac{\sum_i (x_i - \bar{x})(y_i - \bar{y})}{\sqrt{\sum_i (x_i - \bar{x})^2 \sum_i (y_i - \bar{y})^2}}$$

where $\bar{x}$ (resp. $\bar{y}$) denotes the mean of the $(x_i)_i$ (resp. $(y_i)_i$) points. In our example, the PCC is as high as 0.99998 and thus confirms the monofractal signature of the signal. Let us note that if the values of $q$ are chosen symmetrically with respect to 0, e.g. from -2 to 2 by steps of 0.1, then $\sum_i x_i^3 = 0$ in equations (1.10) and (1.11) and thus

$$c_1 = \frac{\sum_i x_i y_i}{\sum_i x_i^2} \qquad c_2 = \frac{-\sum_i x_i^2 y_i}{\sum_i x_i^4}, \tag{1.12}$$

which gives back equation (1.9) for $c_1$. It is worth recalling that there is no consensus in the literature on a parameter nor on a threshold that should be used to affirm that a signal is monofractal or multifractal. Such choices are left to the discretion of the practitioner depending on the context.

### Scaling regimes, scale breaks and practical interpretation

A last important remark is about the practical interpretation of the Hölder exponents obtained from a signal. Theoretically, the notion of Hölder exponent is intrinsically linked to limits and the WLM requires to examine the asymptotic behavior (at small scales) of the partition and scaling functions. Nevertheless, only a finite number of scales are available in practice and the smallest scales depend on the resolution of the data. Therefore, if the scales 2 to 7 are used to build $\eta$ (as in the top right plot of Figure 1.5) and if we conclude that $\eta$ is monofractal with exponent 0.5, it actually means that the signal has a monofractal structure with Hölder exponent 0.5 **at those scales**. The physical dimension of the data is necessary to fully understand how this works. Conceptually speaking, if we consider that the above Brownian motion is sampled at the rate of 1 measurement per hour, then, roughly speaking, the scales 2 to 7 study the signal by blocks of $2^2 = 4$ to $2^7 = 128$ data points and thus the signal is monofractal from the scale of the hour to the scale of the week. Now, if a new device allows measurements every second, it is possible that a different scaling regime (either monofractal or multifractal) appears from the scale of the second to the scale of the hour (which are the new smallest scales available), while at larger scales this new signal still displays its monofractal behavior with Hölder exponent 0.5. Such regime shifts can be observed when the structure function is plotted and thus guide the choice of the scales to consider to build the scaling function $\eta$.

This discussion is illustrated with the following example. We consider a Brownian motion $f_1$ (with $H = 0.5$) made of $2^{18}$ points and a fractional Brownian motion (fBm) $s$ of exponent 0.8 made of $2^{11} + 1$ points. We build the signal $s'$ as

$$s'(1 + k2^7 + j) = s(k + 1) + \frac{s(k + 2) - s(k + 1)}{2^7} j$$

for $k = 0, \ldots, 2^{11} - 1$ and $j = 0, \ldots, 2^7 - 1$ so that $s'$ is made of $2^{18}$ points, corresponds with $s$ every $2^7$ points and is linear on each segment of the type $[1 + k2^7, 1 + (k + 1)2^7]$. We set $f_2 = 100s'$ and we apply the WLM on $f = f_1 + f_2$, which is partially plotted in Figure 1.6 along with $f_1$ and $f_2$. By construction and with the use of a wavelet with at least two vanishing moments, the influence of $f_2$ remains negligible for scales 1 to 7 and is the dominant force at stake from the $8^{\text{th}}$ scale, which is confirmed by the structure function plotted in Figure 1.7. The two distinct scaling regimes can be observed. The first one, at small scales (from 2 to 7), gives a linear scaling function $\eta$ with slope $c_1 = 0.51$, $c_2 < 10^{-2}$ and PCC $> 0.99$, which is the signature of $f_1$. The second one, at larger scales (from 8 to 14), also gives a linear $\eta$ with $c_1 = 0.83$, $c_2 < 10^{-2}$ and PCC $> 0.99$; it thus captures the variability of $f_2$. The scale break between scales 7 and 8 is actually well-marked in Figure 1.8, which shows that the hierarchy that generally arises among the wavelet leaders is broken between those scales. Similarly, the right plot of Figure 1.8 shows the proportion of wavelet leaders at a given scale $j$ that actually are

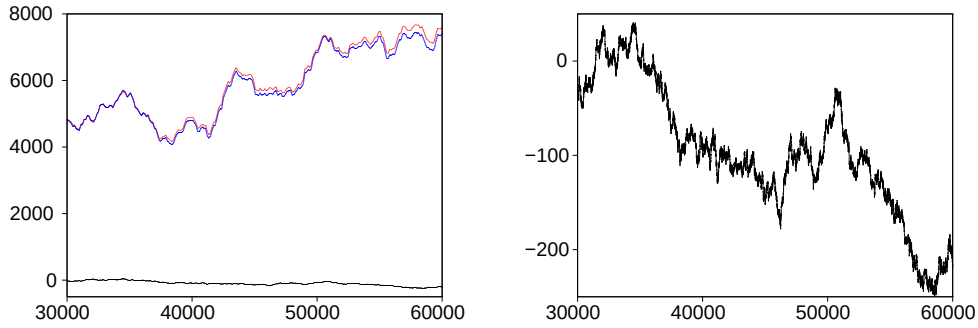


Figure 1.6: Left: The signals $f_1$ (black), $f_2$ (red), and $f$ (blue) studied to show the presence of two scaling regimes within the same signal. Right: Close-up on $f_1$. At large scales, $f_2$ governs the variability of the signal while at small scales it is $f_1$.

wavelet coefficients at that scale $j$ (i.e. the proportion of horizontal green lines per scale in the left panel). Since this percentage reaches 99.3% for $j = 8$ and notably differs from the proportions for $j < 8$ and $j > 8$ [5], it can be suggested that a change of mechanism occurs at that scale. The same curves are also displayed when $f_1$ and $f_2$ are processed separately with the WLM. It can clearly be seen that the behavior of $f$ mostly depends on $f_1$ at small scales and that a switch to $f_2$ occurs at scale 8.

Finally, this discussion shows that the naming "Hölder exponent" cannot have exactly the same meaning in theory and in practice. When used in practice, it is implicitly associated with a particular range of scales used in the underlying multifractal formalism. In the literature it is often denoted as **scaling exponent** of the signal at the relevant scales. Alternatively, in order to get closer to the mathematical meaning, the ambiguity can be dispelled by precising in advance the type (scale) of data being studied. For example, the denomination *"Hölder exponents of daily mean temperature signals"* signify that the signals are sampled at the specific rate of one measurement per day and only the scaling regime at *small scales* is studied[6]. That being said, the terms Hölder exponent and scaling exponent will be used interchangeably in the following and their interpretation (e.g. regularity at small/large scales) will be clear from the context.

[5] Recall that the first scale and the largest ones are not relevant.

[6] Indeed, if a scale break is present and if a second scaling regime occurs at large scales, the associated exponents are not related to the daily scale anymore.

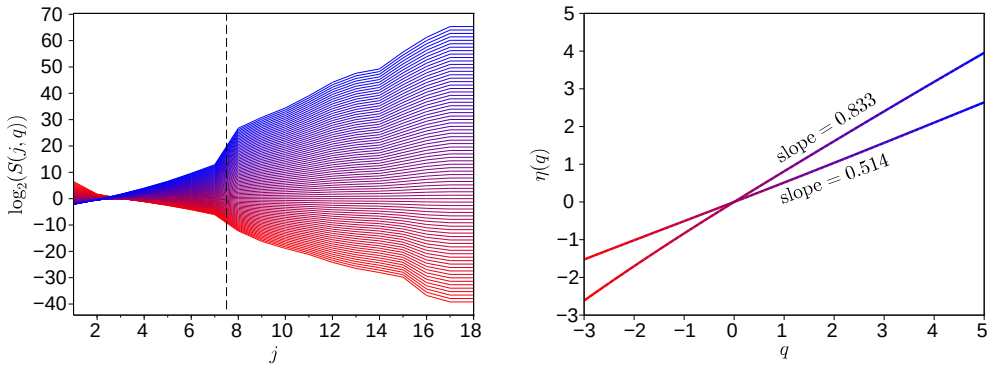


Figure 1.7: Left: $j \mapsto \log_2(S(j,q))$ for $q$ ranging from -3 to 5. A scale break can be observed between scales 7 and 8, as expected. Right: $q \mapsto \eta(q)$ for the scaling regime at scales 2 to 7, giving a slope close to 0.5, and at scales 8 to 14, which gives back the behavior of $f_2$.

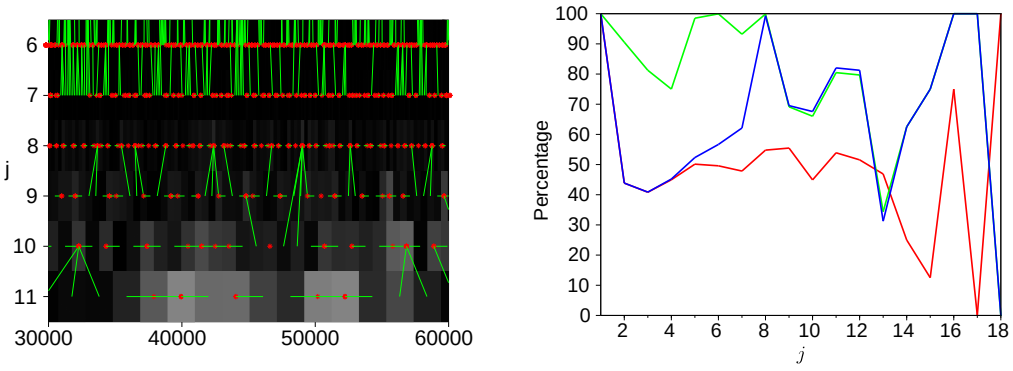


Figure 1.8: Left: A partial time-scale representation of the wavelet leaders of $f$. The change of regime from scale 7 to 8 can be observed. Right: The proportion of wavelet leaders of $f$ (blue) at scale $j$ which actually are wavelet coefficients at scale $j$, as a function of $j$, and for $f_1$ (red) and $f_2$ (green) when they are analyzed separately. Clearly, $f$ displays a similar behavior as $f_1$ at small scales and as $f_2$ at large scales.

# Chapter 2

# Analysis of Mars topography

In this chapter, we investigate the fractal nature of Mars topography with the WLM as detailed in section 1.4; most of the results presented here have been published in [38]. It appeared to us that, due to endless technological improvements and the increasing amount of data collected in recent years, the planetary and space sciences community has a growing interest in multifractal analysis and the regularity/scaling properties of celestial bodies. However, it also seemed that researchers in this specific field are not particularly aware of multifractal wavelet-based techniques such as the WLM, especially when it comes to multidimensional analyses. Therefore, we decided to conduct this study to exhibit the potential of this technique with their datasets and hopefully motivate scientists to use these tools[1]. It thus mainly consists in a practical implementation of the WLM in a real-life context in which we provide an analysis of the scaling regimes and exponents obtained. For more information on the physical significance or more accurate possible interpretations of the results, the reader is referred to the references given throughout the chapter.

## 2.1 Introduction

The surface roughness of Mars is an intensively studied subject in the scientific community [7, 88, 90, 95, 106, 130, 133]. Identifying the best possible landing sites for rovers or future manned missions and finding out the geophysical processes that shape the face of the planet are among the most common reasons to analyze Mars topography. The Mars Orbiter Laser Altimeter (MOLA) data collected during the Mars Global Surveyor

[1] In the best case scenario, we will soon be able to build a complete Scilab toolbox on the WLM which could be used easily by any researcher.

(MGS) mission from 1997 to 2001 gave researchers an unprecedented opportunity to study the surface of the Red Planet with a high accuracy.

During the past two decades, numerous works about the fractal properties of Mars topography have been conducted using several tools, such as median differential slopes [88, 121], root mean square (RMS) slope and deviation [111], wavelets [95], power spectral density (PSD) [7] and statistical moments [90, 130]. Regardless the method used, they usually reveal two distinct scaling regimes in the topography of Mars (one at small scales, the other at larger scales) and the scale break varies from one work to another. The Hölder/scaling exponents[2] associated with these scaling laws appear to differ according to the region considered for the study (cratered terrains, smoother plains, ice cap, etc.) but some common features can still be noted among the different works. These exponents are sometimes used to claim that Mars topography is a monofractal or multifractal field, which may depend on the definition of mono- or multifractality adopted by the authors (if any).

Nevertheless, these studies are all based on precision experiment data records (PEDRs), i.e. one-dimensional (1D) along-track series following North-South trajectories. This implies that the two-dimensional (2D) nature of the topographic field has not been taken into account. Even though it seems reasonable to assume that topography is isotropic at the planetary scale ([90]), small scales may be influenced by the spacecraft's orbit (North/South direction) so that the isotropic assumption may be flawed [8, 90]. Also, most of these works do not analyze the whole surface of Mars but rather different regions that display distinct features (craters, plain, ice cap, etc.). Let us also add that these along-track series may have missing points which need to be properly handled [90].

Therefore, the aim of this chapter is twofold: carrying out a complete study of the surface roughness of Mars with the WLM while taking global longitudinal and latitudinal topographic profiles into account, then perform a more local two-dimensional analysis which thus keeps the 2D aspect of the data. We also show that such an analysis allows to recover the main features of the surface of Mars, which validates the effectiveness of the 2D-WLM. For that purpose, we use one of the topographic maps generated from the MOLA dataset (see section 2.2). At the time of working on this project, this was, to the best of our knowledge, the first WLM-based study of this kind and based on this dataset. Hence, we also hope that this work can convince researchers that the WLM is a suitable candidate for the study of scaling properties of planetary surfaces. The organization of the rest of this chapter is the following. We first give a short overview of the previous results obtained in the above-mentioned works and describe the dataset used. Then we present our results about Mars topography in the 1D then in the 2D case before finally discussing the results and drawing some conclusions.

[2]Also called power-law exponents or generalized Hurst exponents; either way keep in mind the end of section 1.4.2.

Table 2.1: Some previous results on the scale break and scaling exponents of Mars topography. For the region type, "(Mars)" indicates that many different areas covering Mars were used, leading to average scale breaks and exponents at small scales ($H$ Ss) and at large scales ($H$ Ls). See the text for more details.

| Method | Reference | Region type | Scale break | $H$ Ss | $H$ Ls |
|---|---|---|---|---|---|
| PSD | [7] | Cratered | $\approx$ 10km | 1.2 | 0.2 |
| PSD | [7] | Lowlands | $\approx$ 10km | 1.2 | 0.5 |
| PSD | [106] | (Mars) | $\approx$ 3.3 km | 1.4 | 0.65 |
| Var. of DWT | [95] | Polar cap | $\approx$ 24km | 1.25 | 0.5 |
| Var. of DWT | [95] | Volcanic plain | None | 0.5 | 0.5 |
| RMS dev. | [111] | (Mars) | N/A | 0.7 | N/A |
| Struct. fcts. | [107] | (9 regions) | $\approx$ 2km | 0.75-0.92 | Not done |
| Haar fluct. | [90] | (Mars) | $\approx$ 10km | 0.76 | 0.52 |

## 2.2 State of the art and dataset

### A wide spectrum of results

In this section we give a short review concerning the scaling properties of Mars topography obtained in the previously mentioned papers. The relevant information is summarized in Table 2.1. Let us first note that the so-called power-law exponent $\beta$ originally obtained with the PSD method is related to the Hölder exponent $H$ obtained with the other methods as $\beta = 2H + 1$ (which is proved for fBms [46, 90, 111]). From now on, $\beta$ will be automatically replaced by $H = (\beta - 1)/2$, so that only $H$ is used to facilitate comparisons.

Among the seminal papers using the MOLA database, [7] and [95] are certainly at the top of the list. The first one uses the so-called "PSD" method on two different regions of Mars: a cratered one in the South and a smoother one in the North (lowlands). At small scales ($< 10$ km), the power spectrum of both areas display a power-law with $H \approx 1.2$ while at large scales ($> 10$ km), one gets $H \approx 0.2$ for the cratered region and $H \approx 0.5$ in the smooth region. Such results are in agreement with those obtained in [95] on the analysis of Mars polar topography using the variance of a discrete wavelet transform of the data: it appears that the Northern polar cap has an exponent $H \approx 1.25$ at small scales ($< 24$ km) and $H \approx 0.5$ at large scales ($> 24$ km). A study of the whole gridded surface of Mars using the PSD was later carried out in [106], where statistical confirmation of the different scaling regimes is brought. It is suggested that $H \approx 1.4$ at small scales and $H \approx 0.6 - 0.7$ at large scales, with a scale break occurring on average around 3.3 km, but some scale breaks up to 10 km are also found. One can see that, even though there are common features between these works, there seems to be no consensus

on the value of $H$ nor about the scale at which the break occurs.

Slightly different results are found when other methods are used. For example, authors in [111] use the "RMS deviation" to compute the Hölder exponent of 30-kilometers long profiles and so covering the planet with small grids. It appears that the distribution of the exponents $H$ follows a Weibull distribution with mean 0.7, while no scale break is detected since only small scales are considered relevant for that study. In the same spirit, authors in [107] computed generalized structure functions (based on surface elevation increments) of order 1 to 12 related to nine distinct sites on Mars which led to exponents $H \approx 0.75 - 0.9$. More recently, in [90], a multifractal formalism based on statistical moments of several orders relying on Haar fluctuations was used. It turns out that their computation of $H$ gives $H \approx 0.76$ at small scales and $H \approx 0.52$ at larger scales, with a scale break occurring at $\approx 10$ kilometers.

Consequently, drawing on these works on the surface roughness of Mars, it seems that PSD-based and wavelet-based methods and those relying on (some kinds of) statistical moments of fluctuations display a scale break which occurs somewhere between 2 and 25 kilometers. At small scales, the power-law exponent $H$ is $H \approx 1.2 - 1.4$ with the former methods and $H \approx 0.7 - 0.9$ with the latter. At large scales though, they seem to agree on the value $H \approx 0.5 - 0.7$. Moreover, let us note that the notions of monofractality and multifractality (if debated) related to the scaling regimes and exponents obtained in these papers heavily depend on the definition (if any) of the authors and is subject to interpretation. Therefore, we will give in the next section our definition of a monofractal or multifractal behavior in the present context.

### MOLA data

Unlike the papers previously mentioned, and due to the objectives of this work, the data used here is not PEDRs profiles. Instead, we perform our analysis on the MOLA Mission Experiment Gridded Data Records (MEGDRs) [132], which are global topographic maps of Mars created by combining altimetry values from the PEDR data acquired over the entire MGS mission (about 600 million measurements). MEGDRs are available at 4, 16, 32, 64 and 128 pixels per degree and are available at `http://pds-geosciences.wustl.edu/missions/mgs/megdr.html`. In order to have as many scales as possible at our disposal, the 128-pixel-per-degree map is naturally chosen. Let us note that this map almost represents the whole planet; the latitude ranges from 88° S to 88° N. More details about the mission, the data and the MOLA experiment can be found in [132, 133] and on the website mentioned above.

## 2.3 Results on the one-dimensional study

First, the WLM is carried out as explained in section 1.4.2 of chapter 1 for 1D latitudinal and longitudinal bands: in this framework, 22528 latitudinal and 46080 longitudinal topographic profiles are analyzed. The third-order Daubechies wavelet [34] is used and the 2D analysis relies on a usual tensor product-based technique [34, 100].

The structure and scaling functions $S$ and $\eta$ defined by equations (1.3) and (1.4) are computed for $q$ ranging from -2 to 2. We know that this choice might seem restricted but it can be justified; we refer the reader to appendix 2.A for a discussion on this point. An example of $j \mapsto \log_2 S(j,q)$ for these values of $q$ is shown in Figure 2.1, as well as $j \mapsto \log_2 S(j,0.5)$ for several longitudinal profiles. As mentioned in section 2.2, several studies about the surface roughness of Mars reveal a scale break occurring at scales between 2 and 25 kilometers [7, 90, 95, 106]. Such a phenomenon also appears in both longitudinal and latitudinal analyses in our computations at $\approx 15$ kilometers, as illustrated in Figure 2.1, which is in good agreement with [7, 90, 95]. We thus consider two scaling regimes: the first one at small scales ($< 15$km) and the second one at large scales ($> 60$km); the scales in between represent the transition from one regime to the other.

### 2.3.1 Small scales ($< 15$ km)

We start with the scaling regime at small scales ($< 15$ km). The function $\eta$ related to different longitudinal and latitudinal profiles is displayed in Figure 2.2. From numerical experiments, we set that $\eta$ is "linear enough" in this context to allow the signal to be considered monofractal if the associated PCC is greater than 0.98 and multifractal otherwise. Let us remind that this threshold is somehow arbitrary and is only used to make clear-cut categories (i.e. mono-multifractal) that allow statistical analyzes; the parameter $c_2$ introduced in section 1.4.2 brings similar information and is not used in the present study. It is more important to keep in mind that a high PCC indicates a near-monofractal behavior and that the distributions of these coefficients also bring valuable information.

As far as the longitudinal signals are concerned, more than 99.7% of them are considered monofractal, i.e. the corresponding $\eta$ has a PCC $> 0.98$ (and $> 0.975$ for more than 99.9% of them). This can be seen on the top left histogram in Figure 2.3. The exponents $H$ extracted and the histogram of their distribution are also represented in Figure 2.3 (middle left and bottom left). The mean value of $H$ is 1.15 with a standard deviation of 0.06. As expected, such results are in agreement with PSD- and other wavelet-based methods [7, 95]. Regarding the latitudinal signals, it appears that 92.1% are monofractal. Such a drop in the proportion of monofractal signals may seem surprising at first sight, but a few reasons may contribute to explain it: the crustal dichotomy of Mars, the presence of polar caps, the fact that the map is actually a projection of

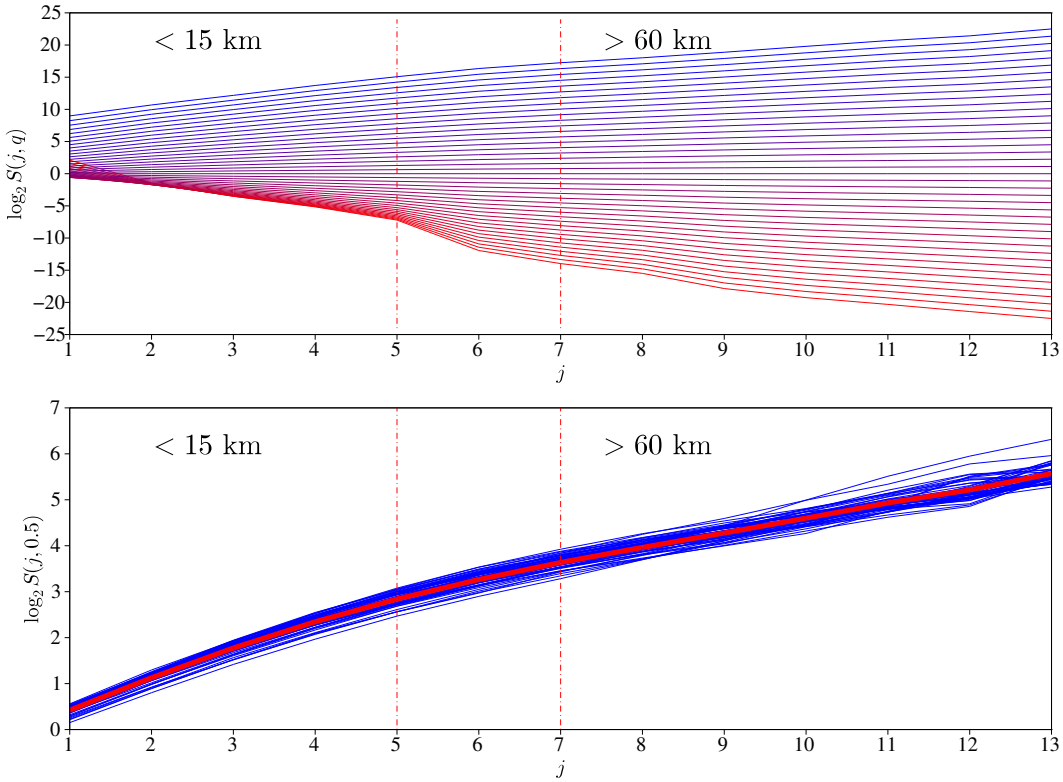


Figure 2.1: Top: $\log_2 S(j,q)$ versus $j$ for $q$ ranging from -2 (red) to 2 (blue) by steps of 0.1 for a longitudinal band. A given scale $j$ corresponds to a spatial resolution of $0.463 * 2^j$ kilometers. The vertical dashed lines delimit the scaling regimes at small scales ($<$ 15 km) and at large scales ($>$ 60 km). Bottom: $\log_2 S(j,0.5)$ versus $j$ for several longitudinal bands (blue) and mean of these functions over the longitudinal bands (red).

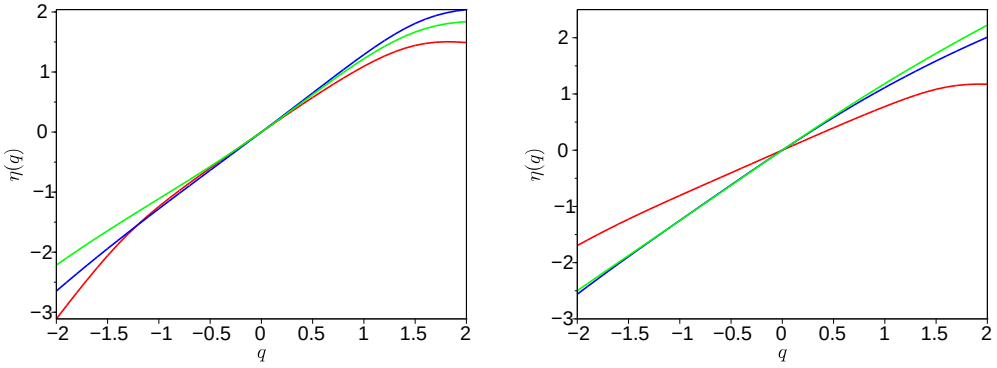


Figure 2.2: Left (resp. right): functions $q \mapsto \eta(q)$ for several longitudinal (resp. latitudinal) profiles at small scales. In both cases the red one is considered as the signature of a multifractal signal.

the planet, the North/South trajectory of the orbiter, among others. Moreover, if we only keep latitudes between $80°S$ and $80°N$, then more than 96.7% of the signals are monofractal and again this percentage rises above 99.9% if we allow PCC $> 0.975$; this can be noted on the top right histogram in Figure 2.3 (with latitudes kept from $80°S$ to $80°N$). Considering only these restricted latitudes, the mean value of $H$ is 1.05 with standard deviation 0.13. The influence of latitude can be clearly seen in Figure 2.3 and such a latitudinal pattern is in agreement with [111]. Besides, a clear difference appears between the two hemispheres: the mean value of $H$ is 0.98 in the North and 1.12 in the South.

Consequently, it seems reasonable to admit that a monofractal behavior is indicated at small scales but the latitudinal study has to be more carefully interpreted and could even be irrelevant in polar regions. Let us also note that the results of the longitudinal case remain almost unchanged when poles are removed and that the clear difference of shape in the histograms of Figure 2.3 and the differences in the values of $H$ may indicate a slight anisotropy of the surface roughness at small scales, as mentioned in [8].

### 2.3.2 Large scales ($> 60$ km)

Let us now focus on the larger scales. For that purpose, we consider scales ranging from $\approx$ 60 km to $\approx$ 4000 km (between $\approx$ 15 km and $\approx$ 60 km we consider that a transition occurs). Contrary to the results obtained at the small scales, it turns out that the longitudinal and the latitudinal (restricted) analyses mostly display a multifractal behavior (see Figure 2.4). Indeed, for the longitudinal ones (resp. latitudinal), the PCC is lower than 0.98 for 91.7% (resp. 63.2%) of the bands. Such an observation is in agreement with [90], though the latitudinal study has to be carefully interpreted as already mentioned. A large percentage of latitudinal bands still has to be considered

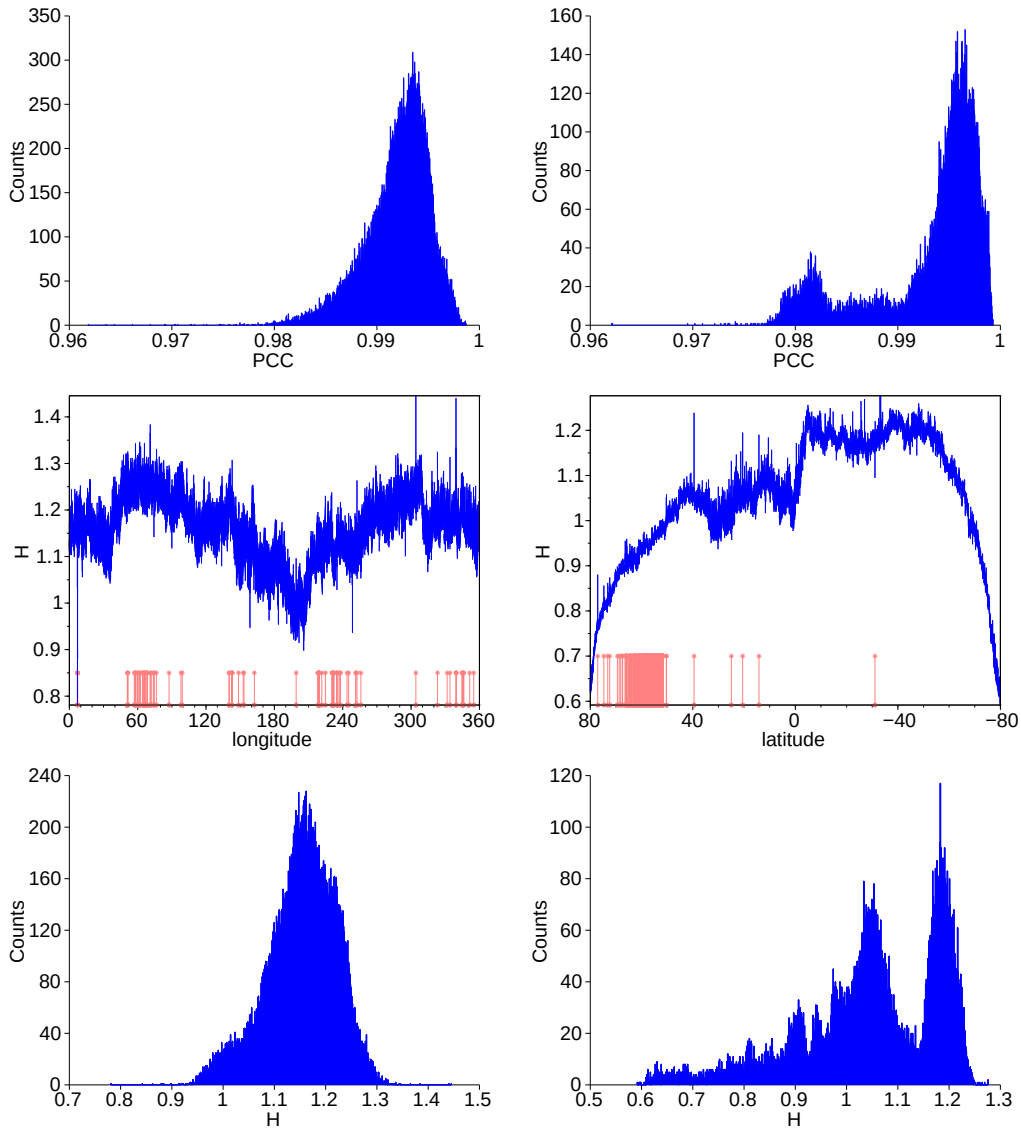


Figure 2.3: Top: Histograms of the distribution of the PCCs related to the functions $\eta$ for the longitudinal (left) and latitudinal (right) analyses at small scales ($< 15$ km), subdivided into 1000 equally spaced bins. Middle: Exponent $H$ as a function of longitude (left) and latitude (right) at small scales ($< 15$ km). The red lines indicate the topographic profiles that are considered multifractal. Bottom: the corresponding histograms of the distributions of $H$, subdivided into 1000 equally spaced bins.

Table 2.2: Proportions of longitudinal (left) and latitudinal (right) bands that are monofractal/multifractal at small scales (Ss) and at large scales (Ls).

| Ls \ Ss | Mono. | Multi. |
|---|---|---|
| Mono. | 8.25% | 0.05% |
| Multi. | 91.53% | 0.17% |

| Ls \ Ss | Mono. | Multi. |
|---|---|---|
| Mono. | 33.67% | 3.18% |
| Multi. | 63.07% | 0.08% |

monofractal; however, there is a clear difference in the distribution of the PCCs and the exponents $H$ compared to the small scales case (Figure 2.3 and Figure 2.4). The mean value of $H$ is 0.78 for the longitudinal bands (resp. 0.65 for the latitudinal) with standard deviation 0.087 (resp. 0.11), which is consistent with [106]. Again, a clear difference appears between the two hemispheres: the mean value of $H$ is 0.74 in the North and 0.55 in the South. Let us add that longitudinal results remain almost unchanged when poles are removed. It is also worth to recall that in the multifractal case, $H$ does not fully characterize the multifractal nature of the data but stands for the "most frequent" exponent in the signal (maximum of the spectrum of singularities).

### 2.3.3 Localization of the monofractal and multifractal profiles

To complete this section on the 1D analysis of Mars topography, we briefly discuss the spatial distribution of the monofractal and multifractal bands. For that purpose, Figure 2.5 shows a topographic map of Mars in false colors. On the top of the map (resp. on the right), red lines indicate the few longitudinal (resp. latitudinal) bands exhibiting a multifractal behavior at small scales, while the green ones correspond to those associated with a monofractal behavior at large scales. The proportions of longitudinal and latitudinal profiles that are monofractal/multifractal at small scales and monofractal/multifractal at large scales are given in Table 2.2. As mentioned previously, a large part of the signals switch from a monofractal behavior at small scales to a multifractal behavior at larger scales.

The analysis carried out on a band has somehow a "global" connotation from a spatial point of view, compared to the more "local" 2D analysis performed in the next section. That being said, it appears in Figure 2.5 that some areas of Mars seem to have an impact on the whole characterization of the fractal nature of a band. Indeed, regions such as Hellas Planitia ($50°S$ $70°E$), Olympus Mons ($20°N$ $225°E$) and the Tharsis region ($0°N$ $250°E$) are likely to influence both longitudinal and latitudinal analyzes. Also, the latitudinal analysis seems to be affected by the crustal dichotomy of Mars since a large part of the Northern hemisphere displays a multifractal behavior at small scales and a monofractal at large scales. This could be the result of the fact that the

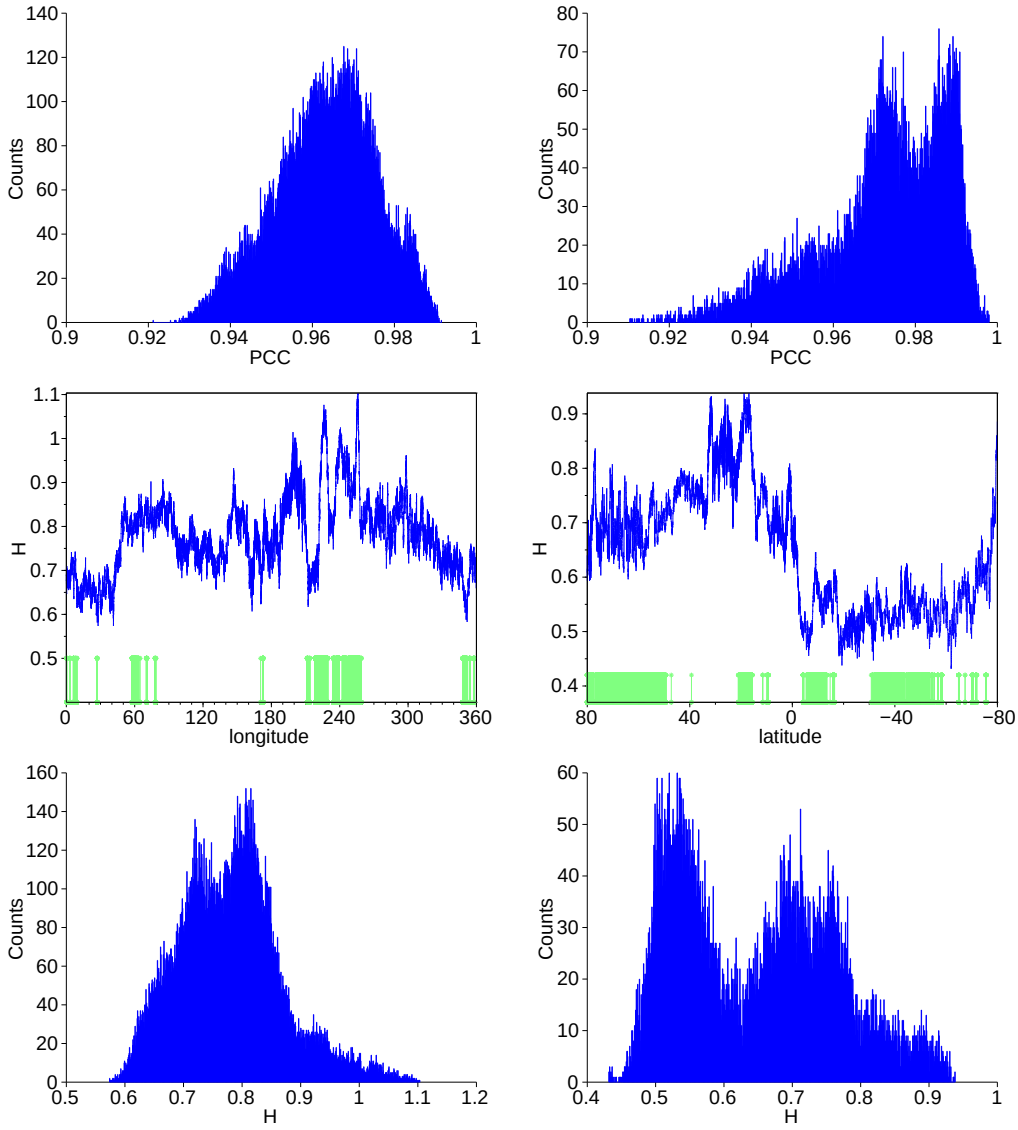


Figure 2.4: Top: Histograms of the distribution of the PCCs for the longitudinal (left) and latitudinal (right) analyses at large scales ($> 60$ km), subdivided into 1000 equally spaced bins. Middle: Exponent $H$ as a function of longitude (left) and latitude (right) at large scales ($> 60$ km). The green lines indicate the topographic profiles that are considered monofractal. Bottom: the corresponding histograms of the distributions of $H$, subdivided into 1000 equally spaced bins.

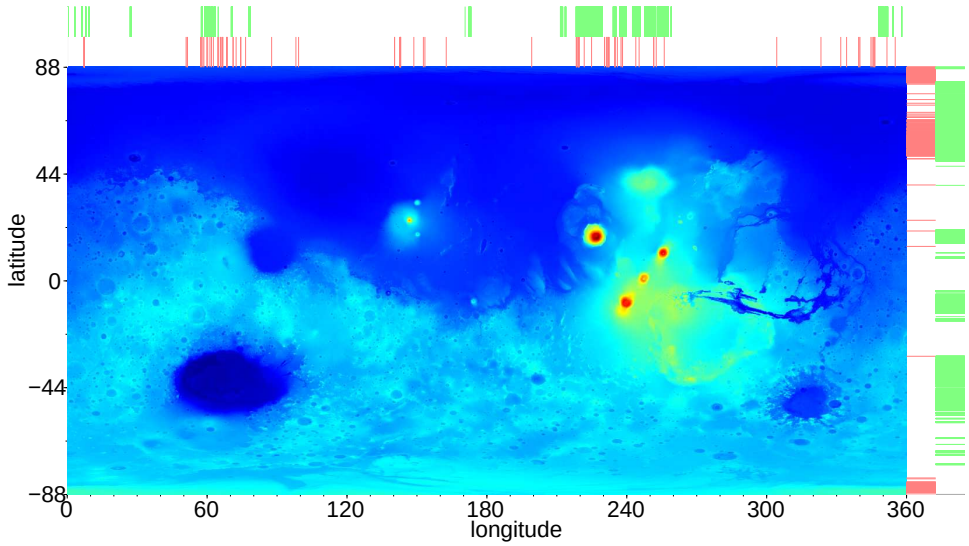


Figure 2.5: Topographic map of Mars in false colors (dark blue corresponds to an altitude of roughly -8100 meters and dark red to 21200 meters). On the top of the map (resp. on the right), red lines indicate the few longitudinal (resp. latitudinal) bands exhibiting a multifractal behavior at small scales, while the green ones correspond to those associated with a monofractal behavior at large scales.

topographic profiles at these latitudes are smooth and, from time to time, interrupted by a crater or an anomalously irregular pattern. Therefore, at small scales, both the wavelet coefficients related to the smooth behavior and those associated with the rougher one are present, which globally results, quite logically, to a multifractal behavior. At large scales though, the sporadic irregularities are somehow smoothed out or masked by the predominant regular (smooth) nature of the profile, thus a monofractal behavior is detected. This can be easily interpreted in another way: with the naked eye (i.e. what we see is the behavior at large scales), it is natural to assert that such profiles do not vary too much due to the smoothness of the entire area, which outbalances the irregularities (they can barely be seen). Moreover, since these bands appear, at large scales, very smooth, it should lead to larger scaling exponents. This is actually the case as seen in Figure 2.4. These explanations should be investigated in more detail in future works, since the influence of possible artifacts cannot be completely excluded.

## 2.4 Results on the two-dimensional analysis

Let us now examine the results of the two-dimensional WLM performed on the topographic map of Mars. Contrary to [8] and [64] where the two-dimensional multifractal detrended fluctuation analysis (see section 3.A) is used to study a grayscale image of a relatively small part of Mars, we aim to examine the whole surface, where data points are actual topographic measurements. For that purpose, the map used in the 1D case is first gridded into squares of $1024 \times 1024$ pixels (which will be called tiles in the following) thus giving $\approx 1000$ tiles to analyze. Such tiles correspond to windows of $8^\circ \times 8^\circ$ on Mars. The choice of the tile size is rather subjective but is a good compromise between a local analysis (size not too large) and the statistical meaning of the results (size not too small). In a different approach, a similar resolution ($5^\circ \times 5^\circ$) is used in [106], where a detailed justification of such a choice is provided. In order to increase the statistical significance of the following results, the grid is also shifted 512 pixels rightward, then downward and finally both rightward and downward, giving us a total number of 3696 tiles to work with.

Due to the restricted number of data available in such tiles, the parameter $q$ now ranges from -1.5 to 1.5 and the threshold for the PCC to consider a signal as monofractal is now 0.97. However, the differences in the distributions of the PCCs and the exponents at small and large scales are somehow more significant than the value chosen for the threshold and the associated proportions of monofractal and multifractal signals. As a first result, it can be noted that a scale break occurs once again at $\approx 15$ kilometers; this is illustrated in Figure 2.6 (which can be compared with Figure 2.1) where the function $j \mapsto \log_2 S(j, q)$ is plotted for a tile for several values of $q$ and $j \mapsto \log_2 S(j, 1)$ is plotted for 370 tiles uniformly distributed in the map. The break may not seem as clear as in the one-dimensional case due to the lower number of topographic measurements available in

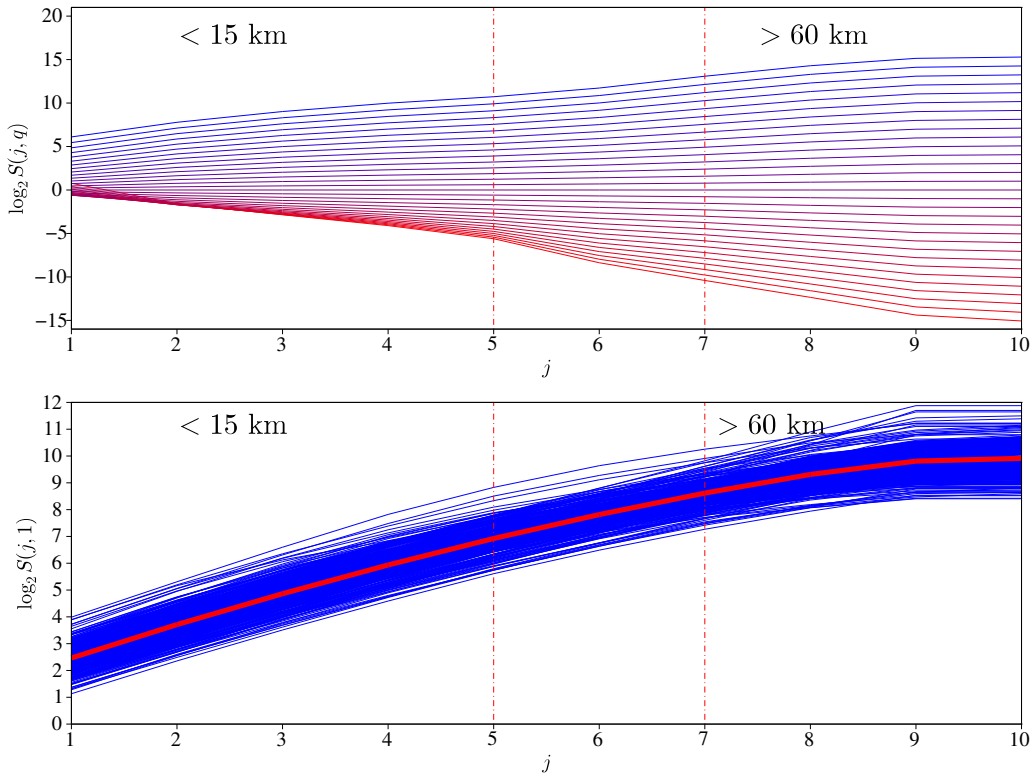


Figure 2.6: Top: $\log_2 S(j,q)$ versus $j$ for $q$ ranging from -1.5 (red) to 1.5 (blue) by steps of 0.1 for a tile. Bottom: $\log_2 S(j,1)$ versus $j$ for several tiles (blue lines) and mean of these functions over the 3696 tiles (red).

this case. Nevertheless, two scaling regimes can still be identified; this will be confirmed in the following.

### 2.4.1 Small scales ($< 15$ km)

Not surprisingly, the 2D analysis of Mars topography reveals a monofractal behavior at small scales. Indeed, 96.1% of the considered tiles have a function $\eta$ with a PCC greater than 0.97, as shown in Figure 2.7. As seen in the spatial distribution of these coefficients (Figure 2.7), the multifractal regions are mostly located around Hellas Planitia ($50°S$ $70°E$), Amazonis Planitia ($25°N$ $180°E$) and Acidalia Planitia ($25°N$ $330°E$). The mean of the exponents $H$ is 1.12, with standard deviation 0.13, which is consistent with the 1D analysis; their distribution is represented in Figure 2.7. One can note that this histogram is somehow bimodal as the one corresponding to the latitudinal study, suggesting that the latitudinal pattern previously observed has some influence in this case. This is confirmed in Figure 2.8, which shows the longitudinal and latitudinal av-

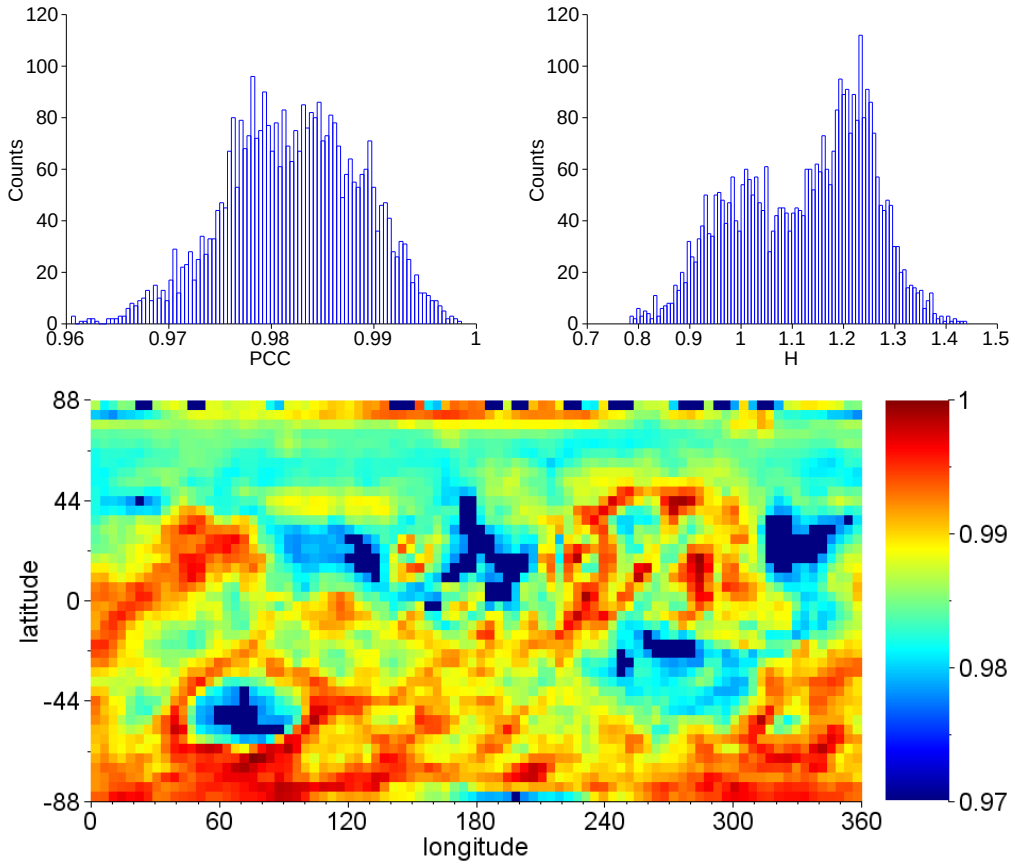


Figure 2.7: Top: Histograms of the distribution of the PCCs and the exponents $H$ for the 2D analysis at small scales ($< 15$ km), subdivided into 100 equally spaced bins. Bottom: The spatial distribution of the PCCs where the multifractal tiles are all colored in dark blue.

erage of $H$ of the 2D analysis. It can also be noted that these curves display a similar behavior as those obtained by averaging the exponents of the 1D case by blocks of 1024 longitudinal and latitudinal bands. Besides, the difference between the two hemispheres is similar to the one in the 1D case: the mean value of $H$ is 1.07 in the North and 1.17 in the South. Overall, these results are in good agreement with those obtained in the 1D case and with studies such as [7, 95, 106].

### 2.4.2 Large scales ($> 60$ km)

Let us now examine the second scaling regime for the 2D analysis. Similarly to the 1D case, it appears that several regions of the planet switch to a multifractal behavior at large scales. Indeed, it turns out that 45.8% of the tiles have a function $\eta$ with a PCC

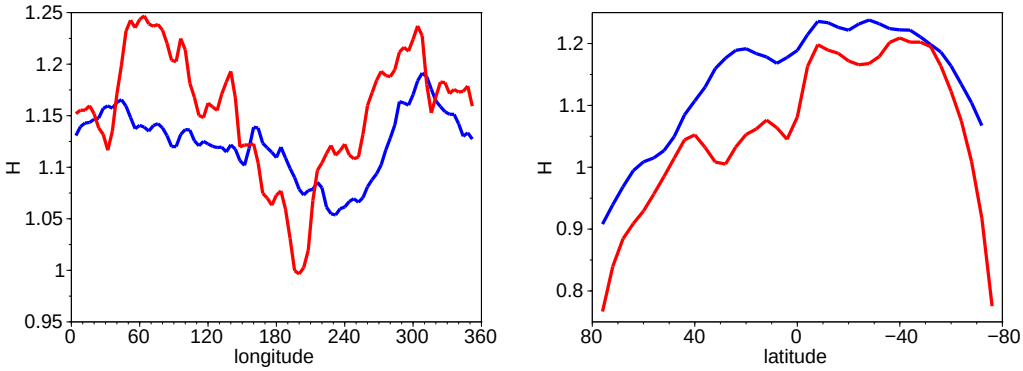


Figure 2.8: Left (resp. right): the blue line indicates the mean of the exponents $H$ longitudinally (resp. latitudinally) in the 2D case, for the small scales. The red line represents the mean of the exponents $H$ of the 1D case by blocks of 1024 longitudinal (resp. latitudinal) bands.

smaller than 0.97. This is illustrated in Figure 2.9 where the distribution of the PCCs is represented, as well as the distribution of the exponents $H$ extracted. The Northern hemisphere is mostly multifractal and Figure 2.9 clearly exhibits the crustal dichotomy of Mars. Other multifractal areas include Hellas Planitia ($50°S$ $70°E$), Solis Planum ($20°S$ $260°E$) and the southern latitudes (even though the influence of the projection cannot be excluded in this case). This switch from monofractality to multifractality is less pronounced than in the 1D case because of the restricted number of scales available in this context, which artificially facilitates the monofractal characterization. Also, the 1D study is more concerned with global features while the 2D study examines the local scaling of the topographic field. Nevertheless, the clear difference in the distributions of the PCCs and exponents $H$ at small and large scales still supports the existence of two distinct scaling regimes, regardless the monofractal or multifractal nature of the tiles. The mean value of $H$ is 0.67, with a large standard deviation of 0.3. Surprisingly enough are the curves displayed in Figure 2.10, which show as in Figure 2.8 the longitudinal and latitudinal average of $H$ of the 2D analysis compared with those obtained by averaging the exponents of the 1D case by blocks of 1024 longitudinal and latitudinal bands. Regarding the longitudinal case, the consistency between the two is obvious, with $H$ slightly lower in the 2D case. The latitudinal case is interesting in another way. Indeed, the exponents extracted in the 2D case are much larger in the Northern hemisphere, then they drop to lower levels. As already mentioned, this may be explained by the famous Martian crustal dichotomy: the Northern hemisphere is rather flat, with few impact craters. Therefore, it appears extremely smooth at large scales, which explains the relatively large scaling exponents $H$ associated with the regions within that area. Such a difference in the surface roughness of the two hemispheres was also noted in the

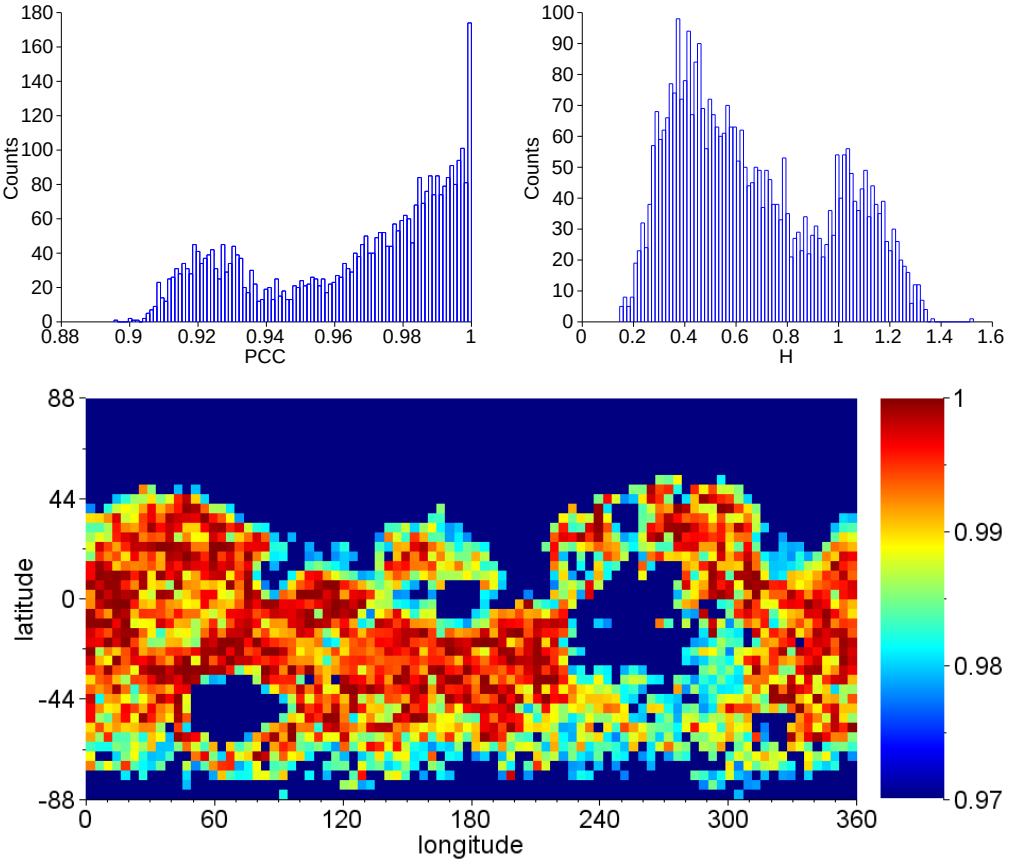


Figure 2.9: Top: Histograms of the distribution of the PCCs and the exponents $H$ for the 2D analysis at large scales ($> 60$ km), subdivided into 100 equally spaced bins. Bottom: The spatial distribution of the PCCs, where the multifractal tiles are all colored in dark blue.

1D case and is largely confirmed here: the mean value of $H$ is 0.83 in the North and 0.51 in the South. The fact that the results differ so much from the 1D case for the highest latitudes may be due to the fact that less wavelet coefficients are used in the analysis of tiles of $1024 \times 1024$ pixels than in the latitudinal bands and that the 2D case is more a "local" analysis.

### 2.4.3 Detection of major surface features

In this last section, we show that the spatial distribution of the scaling exponents $H$ obtained from the 2D analysis of Mars is not "random". Indeed, it is possible to detect major surface features of Mars in the spatial distribution of these exponents, which is an extra argument in favor of the effectiveness of the WLM. The identification of a

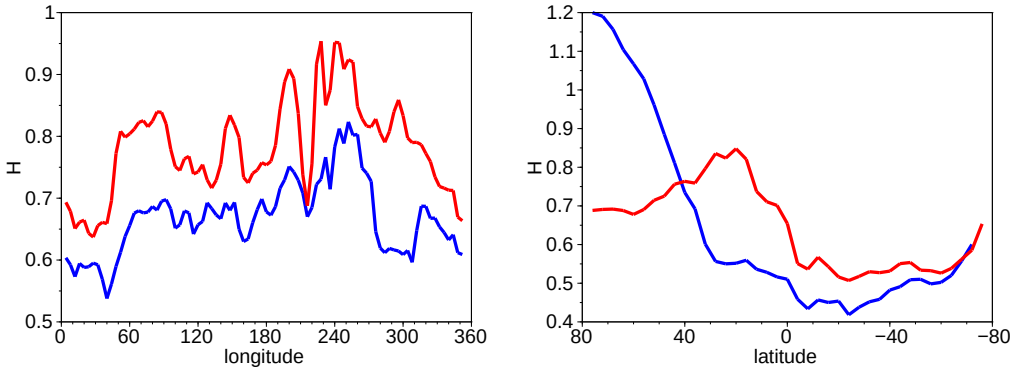


Figure 2.10: Left (resp. right): the blue line indicates the mean of the exponents $H$ longitudinally (resp. latitudinally) in the 2D case, for the large scales. The red line represents the mean of the exponents $H$ of the 1D case by blocks of 1024 longitudinal (resp. latitudinal) bands.

particular feature is merely qualitative and subjective. In other words, we do not use any algorithm to determine whether a pattern is detected or not; such a decision may depend on the expectations of the reader for a feature to be detected. Nevertheless, as shown below, there is often no point denying that some characteristics are clearly identified.

For that purpose, we consider 9 of the most famous sites of the Red Planet: Hellas Planitia (A), Isidis Planitia (B), Elysium Mons (C), Vestitas Borealis - Northern plains (D), Olympus Mons (E), Tharsis (F), Valles Marineris (G), Argyre Planitia (H) and Acidalia Planitia (I). These regions are represented in Figure 2.11. Let us recall that the analysis carried out in the previous section was only performed on a sample of tiles of $1024 \times 1024$ pixels, not all the possible ones. The value of $H$ corresponding to a tile is associated with the central pixel of the tile and, in order to fill in the gaps, the missing values are interpolated using a 2D cubic spline. The interpolation method used is not of primary importance; it is only used for more comfortable visual results and the interpolated values are not used in any statistical analysis. The maps representing the spatial distribution of the scaling exponents $H$ at small and large scales are displayed in Figure 2.11.

At small scales, among the 9 features of interest, it seems reasonable to say that sites A, B, D, F, G and H can be identified on the map, whereas regions C, E and I cannot. Regarding the exponents $H$ at large scales, it is safe to assert that areas A, B, D, E, F and I are pinpointed on the map, while it is not as clear as far as features C, G and H are concerned. As already mentioned, poles appear to behave differently than their surroundings but this may be due to some artifacts such as the projection used to generate the maps. Also, the typical crustal dichotomy and the border of that feature

(the vast Vestitas Borealis and Northern plains in a broad sense) are clearly detected on the maps, especially the one representing the exponents $H$ at large scales.

## 2.5 Conclusion

We used the MOLA data from the Mars Global Surveyor mission to study the surface roughness of Mars with the WLM. We first focused on 1D latitudinal and longitudinal topographic profiles of the complete 128-pixels-per-degree map of the planet. It appeared that a scale break occurs at $\approx 15$ kilometers as in some previous studies, which led us to consider small and large scales separately. Regarding the small scales, Mars topography was shown to exhibit a monofractal nature, with a mean scaling exponent $H \approx 1.11$. Conversely, it turned out that at large scales, a multifractal behavior is often displayed, with $H \approx 0.74$. A latitudinal trend also appeared, as well as indications of a slight anisotropy in the topographic field, though such statements have to be confirmed via several analyses. Regardless the values of $H$, we also showed that our results are in agreement with previous seminal studies, thus confirming that the WLM is well-suited for studying the irregularity of celestial bodies.

The results obtained in the 2D analysis confirmed most of the results of the 1D case. A scale break at $\approx 15$ kilometers was detected, with a mean scaling exponent $H \approx 1.12$ at small scales and $H \approx 0.67$ at large scales, as well as a switch from a monofractal behavior at small scales to a multifractal behavior at large scales in several regions. The 2D analysis also gave information on the scaling law at a "local" level, which allowed us to show that the spatial distribution of the exponents $H$ recovers some of the most characteristic features of the surface of Mars. It is important to keep in mind that the 2D analysis was carried out with the assumption that the surface of Mars is isotropic, which might not be exactly the case, as mentioned above. Therefore, the differences in the values of $H$ between the 1D and 2D cases could be partially explained this way, though more investigations are needed. The most natural approach for that purpose would be to adapt the wavelet analysis using a hyperbolic wavelet transform ([1, 5, 125, 126]). This seems to be an excellent way to obtain complementary information about the roughness of planetary surfaces.

Let us note that the scale break detected at $\approx 15$ km indicates a change in the geological processes that shape the surface of Mars. While there seems to be no consensus in the literature on the exact nature of these processes, craterization appears to be an eligible candidate, at least as far as the small scales are concerned [7, 90, 108]. Further research is needed to fully understand Martian topography. Nevertheless, it appears that the WLM is a useful tool in the present framework. The results provided here could prove helpful for further investigation on the scaling properties of the surface roughness of Mars. Finally, the topography of other celestial bodies could be studied in an automatic way in future works.

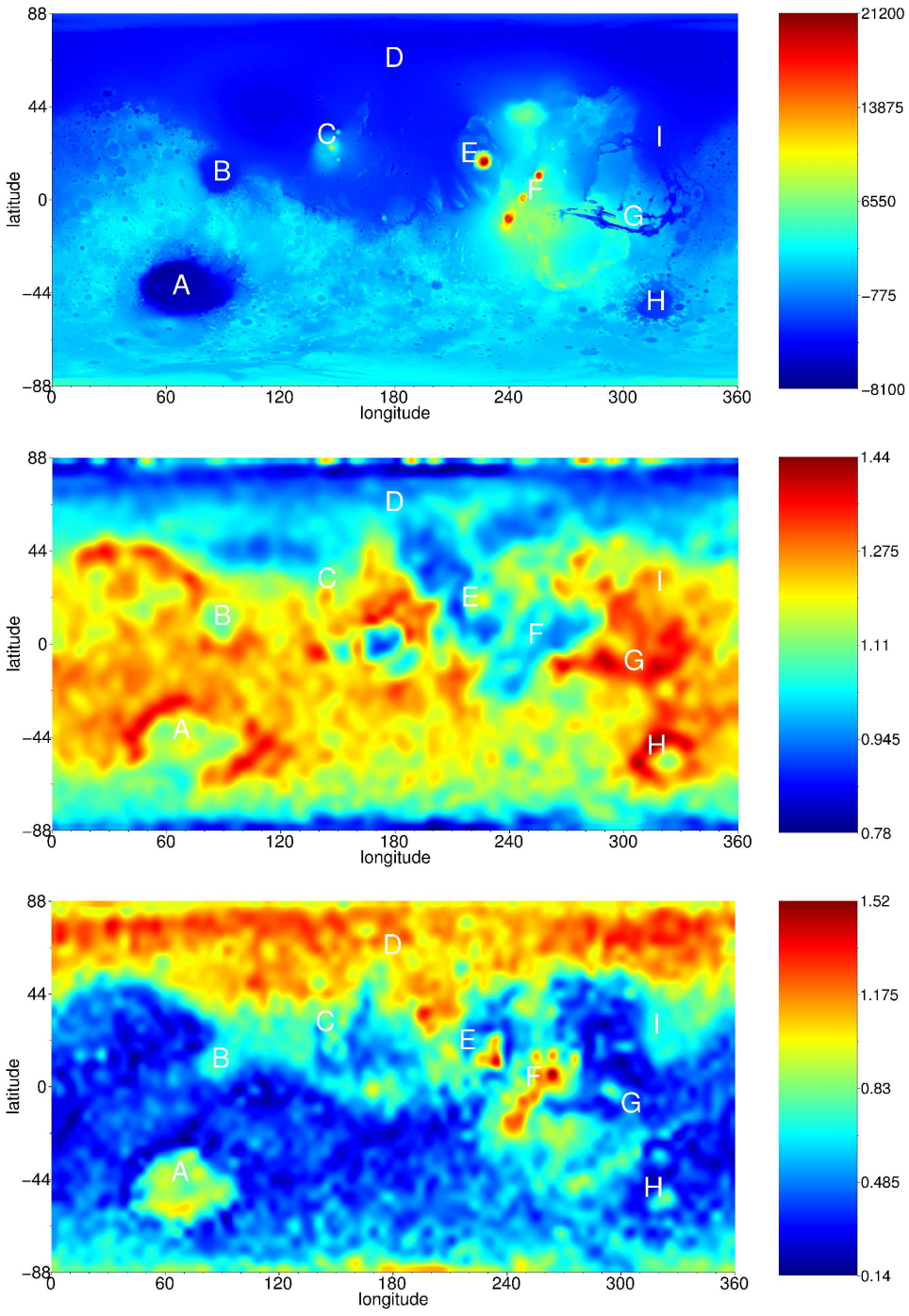


Figure 2.11: From top to bottom: the topographic map of Mars in false colors, the map representing the spatial distribution of the exponents $H$ at small scales, then at large scales. The regions of interest are Hellas Planitia (A), Isidis Planitia (B), Elysium Mons (C), Vestitas Borealis - Northern plains (D), Olympus Mons (E), Tharsis (F), Valles Marineris (G), Argyre Planitia (H) and Acidalia Planitia (I).

*Computational resources have been provided by the Consortium des Équipements de Calcul Intensif (CÉCI), funded by the Fonds de la Recherche Scientifique de Belgique (F.R.S.-FNRS) under Grant No. 2.5020.11. The MOLA data was obtained freely from the Planetary Data System:* `http://pds-geosciences.wustl.edu/missions/mgs/megdr.html`.

# Appendix

## 2.A On the range of values of $q$

As stated in section 2.3, the values of $q$ range from $-2$ to 2 for the 1D study. The arguments supporting this range are illustrated in Figure 2.12 and briefly discussed in this section. First, the lower bound $q = -2$ is acceptable since moments of order $-2$ (and sometimes even below) appear steady and convergent and do not induce any erratic behavior in the functions $\eta$. For the upper bound, as it can be seen from the top right panel in Figure 2.12, a break around $q = 2$ may occur, which makes us choose this value as the upper bound for the values of $q$ for the sake of fairness between the signals. This break is due to a handful of extreme wavelet coefficients (see histogram on the left) that appear when intense sharp variations are present within the signal. According to the criterion used in this paper, the topographic profiles corresponding to the blue and green curves are monofractal and the one associated with the red curve is multifractal. The bottom left figure shows that a comparable break can be simulated with a Brownian motion ($H = 0.5$) for which a data point has been set to five times the maximum value of the signal. A break around $q = 2$ occurs, similarly to the one observed in the top right panel, but the slope of $\eta$ up to $q = 2$ corresponds to the expected value 0.5. It is also shown that this break can be annihilated when the highest 10% of the wavelet coefficients are removed at each scale before the computation of $S(j, q)$. One can see that the break is only due to the highest wavelet coefficients and that removing them only adjusts the curve, though the slope or the monofractal nature of the signal are correctly identified up to $q = 2$. This is also observed for the signals of Mars, as indicated in the last plot and this justifies our choice to limit the ranges of the values of $q$ to -2 and 2.

The same kind of arguments justify the choice of -1.5 to 1.5 as the range of values of $q$ in the 2D case. Let us note that a brief investigation of the breaks did not reveal any relevant information. Anyway, since we are interested in practical results of a standardized analysis of a large number of signals, we imposed these limitations for the values of $q$ for the sake of equity between the signals. It is also worth mentioning that these breaks in the functions $\eta$ could probably be avoided with the more intricate $L^\nu$ method ([48]) when they can be imputed to only a few coefficients, which could refine some of the results presented here. However, this could be seen as a loss of information and the signals considered in the present study are possibly too small for this method to be as efficient as in [48].

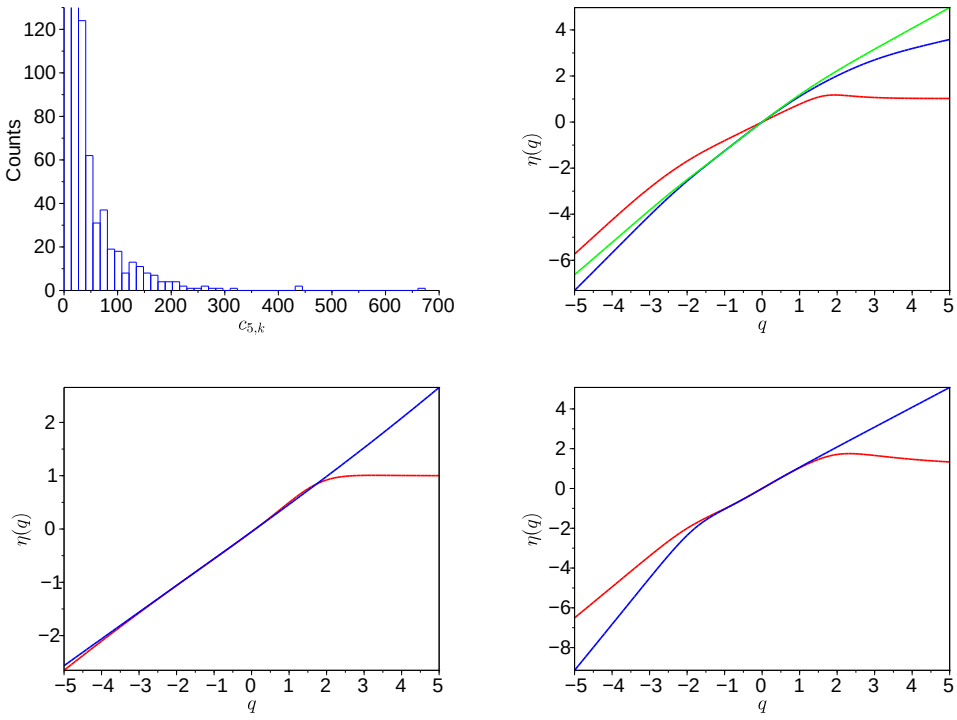


Figure 2.12: Top left: Histogram of the wavelet coefficients at scale $j = 5$ for a longitudinal profile. Top right: Three functions $\eta$ versus $q$ at small scales for $q$ ranging from -5 to 5 for some latitudinal signals (those of Figure 2.2). The red curve and the histogram come from the same signal. Bottom left: In red, the function $\eta$ versus $q$ for a perturbed Brownian motion ($H = 0.5$). In blue, the function $\eta$ obtained for the same signal when the highest 10% of the wavelet coefficients are removed at each scale. Bottom right: In red, a function $\eta$ for a longitudinal profile. In blue, the function $\eta$ obtained for the same signal when the highest 10% of the wavelet coefficients are removed at each scale.

# Chapter 3

# On the fractal nature of temperature time series

As shown in chapter 2, the WLM can provide valuable information on the fractal nature of real-life signals. More specifically, the influence of some particular features of Mars could be observed in both 1D and 2D analyses. However, in that context, it is not easy to come up with a rigorous framework that allows to perform quantitative measurements of this influence. Therefore, we wonder if the WLM can provide information that can be evaluated somehow and that is subtle enough to go beyond the sole computation of Hölder exponents. Far from being the preserve of planetary scientists, the scaling properties of natural datasets are widely studied in numerous fields of geosciences. However, as for chapter 2, it appeared to us that wavelet-based methods are often supplanted by other techniques. As a consequence, we now immerse ourselves in the field of climate data analysis and explore the Hölder regularity of daily mean air temperature data in Europe with the WLM; most of the results presented here have been published in [40].

## 3.1 Introduction

The study of the fractal nature of climate time series is a subject of intense research in the geosciences community, as demonstrated by the wide variety of related publications (see e.g. [10, 23, 94, 112, 128, 129, 137]). When it comes to the investigation of the regularity of air temperature signals, a privileged tool used for the job is the Detrended Fluctuation Analysis (DFA) or its common generalization named Multifractal Detrended Fluctuation Analysis (MFDFA) ([24, 80, 81, 116]) described in section 3.A. These techniques allow to exhibit a monofractal nature in air temperature time series (e.g. [84, 85, 135]) but the values of the Hölder/scaling exponents obtained are hardly

discussed. More specifically, most of these studies agree on a "universal scaling law" governing atmospheric variability with roughly the same exponent ($\approx 0.65$ for the so-called integrated anomalies, not considered here) but few explore the accuracy of the results in terms of correlations with other physical parameters. A geographic distribution of some exponents is displayed in [21] and a "visual" argument states that the results do not seem to be numerical artifacts but have probably a climatological origin. In [78], authors examine the exponents obtained in numerous sites in China and their spatial distribution in more detail. They refute the existence of a "universal" exponent (as we also show) and suggest that the differences might be explained by parameters such as latitude, distance from the shore, monsoons and various landforms interactions. In [77], the same authors study the connection between the scaling exponents of *ground* surface temperature time series and the corresponding types of land (in the same spirit as the work carried out in this chapter) but without considering the climate type of the areas in question.

As stated, this chapter explores the Hölder regularity of daily mean air temperature time series in Europe. We investigate this subject through the WLM presented in chapter 1 with two questions in mind: Is there a strong connection between Hölder exponents and standard deviations of air pressure anomalies? This one is raised because the variability in pressure anomalies can intuitively be seen as one of the natural indicators of the regularity of the climate type that a given region withstands. The second question is: Is the Hölder exponent of a given surface air temperature time series a possible characteristic of its associated climate type? As shown below, it turns out that the Hölder exponents of air temperature data in Europe are indeed closely linked with the Köppen-Geiger climate classification system ([83, 115]).

The rest of this chapter is structured as follows. First, we describe the datasets used and we exhibit a strong anti-correlation between Hölder exponents obtained with the WLM and standard deviations of air pressure anomalies. We also show that this feature is not observed when the MFDFA is performed. Then, we establish a climate classification based on the Hölder exponents in such a way that it allows to recover a simplified version of the Köppen-Geiger classification for Europe. We show that the two classifications match for almost all the stations, and we perform a confirmation test to sustain these observations. We compare these results with those obtained with another dataset to show that the new classification is still well-adapted. Finally, we discuss and summarize the results and we give insights on possible future works.

## Data

The surface air temperature data used throughout this chapter was downloaded from the European Climate Assessment and Dataset website (ECA&D) [49] and consists of daily mean temperatures. The corresponding weather stations were selected in Europe in an area delimited by parallels 36°N (which includes Spain, Italy, Greece) and 55°N (Ireland, Germany) and meridians 10°W (Ireland, Portugal) and 40°E (Ukraine) to have a consistent geographic zone and limit the effects of latitude. Those located above

1000m of altitude were first removed to reduce the influence of this parameter. Also, only temperatures between years 1951 and 2003 were analyzed in order to have numerous homogeneous data. As a result, it appeared that 115 stations fulfilled these requirements. Moreover, the standard deviations of pressure anomalies used in section 3.2, computed from 1951 to 2003, were provided by the NCEP-NCAR Reanalysis Project [109]. The surface air temperature time series used in section 3.3.3 to compare the results with another dataset were also provided by the NCEP-NCAR Reanalysis Project [109].

## 3.2 Hölder exponents and pressure anomalies

We first examine the relation between Hölder exponents and pressure anomalies. The estimation of the Hölder exponents via the WLM is carried out as explained in section 1.4.2 of chapter 1 and is illustrated in Figure 3.1 for the air temperature data of Brindisi (Italy). Note that the air temperature time series are replaced by their cumulative sums before the WLM analysis, i.e. the $n-th$ value is replaced by the sum of the first $n$ values, giving a so-called "temperature profile" [81, 85, 123]. This gives more stable numerical results; it also explains why the Hölder exponents obtained are greater than 1.The wavelet chosen for the analyses is the third order Daubechies wavelet as in chapters 1 and 2.

Since we investigate the Hölder regularity of the time series at a daily scale and since data consists in daily mean temperatures, only the regime at the smallest scales available is investigated (see Figure 3.1). The scaling function $q \mapsto \eta(q)$ of Brindisi is computed for $q$ ranging from -5 to 5 and displays a remarkable linear behavior. Given that the same linear trend is observed for all the stations (see Figure 3.1), the signals can be considered monofractal with Hölder exponents $H$ given by the slope of their scaling function. That being said, in order to improve the robustness to extreme coefficients of this computation, we limit the range of $q$ to $[-2, 2]$. This gives us exponents that range from $\approx 1.1$ to $\approx 1.4$ as shown in the next section, with mean 1.24 and standard deviation 0.087.

To show that the computed Hölder exponents give sound results that can be connected with pressure anomalies, we perform the following test. Each station is associated with its Hölder exponent $h_n$ and with its inverse of standard deviation of pressure anomalies $p_n$ $(n = 1, ..., 115)$. In order to measure if these two sequences are close, we first compact them in the interval $[0, 1]$, i.e. $h_n$ becomes

$$\frac{h_n - \min_n\{h_n\}}{\max_n\{h_n\} - \min_n\{h_n\}} \tag{3.1}$$

and similarly for $p_n$. Then we compute the Euclidean distance $d$ between them and we define $i_0 = d^{-1}$ as an index of similarity between the two sequences. In this case, the value of $i_0$ obtained is 0.37. To check if this index is statistically significant, we compute the same distance but with a randomly shuffled sequence $h_n$ to obtain the index of similarity $i_1$. We iterate the process $10^5$ times to obtain the indices $i_m$ $(m = 1, ..., 10^5)$.

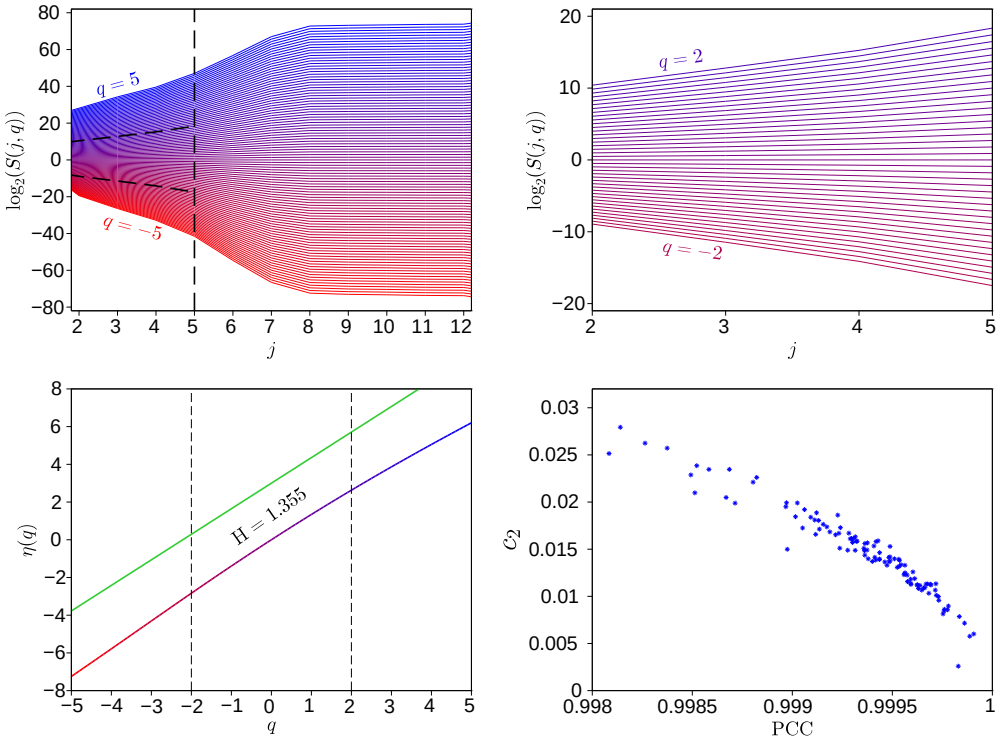


Figure 3.1: Estimation of the Hölder exponent for Brindisi (Italy). Top left: $\log_2(S(j,q))$ versus $j$ for $q=-5$ (red) to $q=5$ (blue) (increasing by steps of 0.1). Only values of $q$ between -2 and 2 and scales up to $j=5$ will be used to compute the Hölder exponents (dashed black lines). Top right: close-up of $\log_2(S(j,q))$ on the values that will be used later on. Bottom left: $\eta$ versus $q$ and associated linear regression line (green) with a vertical shift for the sake of clarity. Since $\eta$ displays a linear behavior (PCC = 0.999, $c_2 = 0.018$), the signal is considered monofractal and the slope gives the Hölder exponent $H$ of the signal. Bottom right: Distribution of the PCC and $c_2$ among the stations (for $q$ from $-5$ to 5). They both give the same information, i.e. the signals display a monofractal behavior.

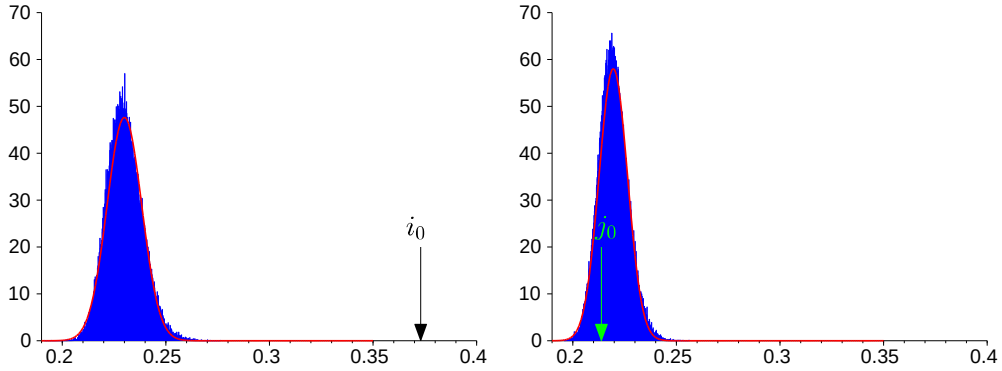


Figure 3.2: Left: Histogram of the indices of similarity between random shuffles of the Hölder exponents $h_n$ obtained with the WLM and the inverse of pressure anomalies $p_n$. The arrow locates the measured index of similarity $i_0 = 0.37$ between $p_n$ and the original sequence $h_n$. The red curve is the Gaussian probability density distribution with mean 0.23 and standard deviation 0.0084. Right: the same for the exponents obtained with the MFDFA instead of those obtained with the WLM. We have $j_0 = 0.21$ and the Gaussian curve has mean 0.22 and standard deviation 0.0069. It appears that $i_0$ is highly significant while $j_0$ is not.

Statistical tests accept the hypothesis that they are normally distributed, with mean 0.23 and standard deviation 0.0084. This implies that the probability that a random shuffle of the Hölder sequence gives an index of similarity larger than $i_0$ is of order $10^{-50}$, which means that $i_0$ is a highly significant index of similarity (see Figure 3.2). Therefore the anti-correlation between the Hölder exponents and the standard deviation of pressure anomalies is confirmed: the higher the standard deviation of pressure anomalies, the lower the Hölder exponents.

For the sake of comparison, we also perform the MFDFA in the same way as described above. More precisely, if $d_n$ $(n = 1, ..., 115)$ denotes the sequence of the exponents re-normalized between 0 and 1 obtained with the MFDFA, then the measured index of similarity between $d_n$ and $p_n$ is $j_0 = 0.21$. The $10^5$ indices $j_m$ $(m = 1, ..., 10^5)$ obtained with the shuffled versions of $d_n$ can be considered normally distributed with mean 0.22 and standard deviation 0.0069, which implies that the probability that a random shuffle of $d_n$ gives an index of similarity larger than $j_0$ is as high as 0.8 (see Figure 3.2). Therefore, in the present case, it appears that the MFDFA is not able to recover sharp information about a connection between the regularity of temperatures and pressure anomalies.

This preliminary study thus indicates that the WLM gives sound results and that its use is appropriate in the following.

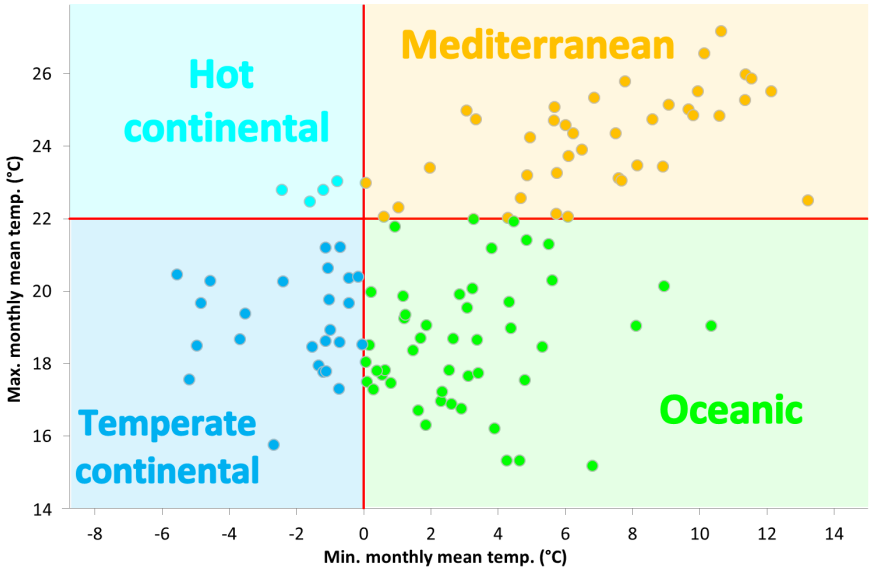


Figure 3.3: Distribution of the 115 weather stations within the different climate types in Europe, according to a simplified version of the Köppen-Geiger climate classification: in this case, precipitation is not taken into account. Hot continental and temperate continental climates are merged and considered as continental climate. Stations close to 0.5°C of another type of climate are also associated with this second category.

## 3.3 From Hölder exponents to a climate classification

### 3.3.1 Köppen-Geiger climate classification

In order to link the Hölder exponents of the stations with their associated climate, we determine the climate type of each station according to a simplified version of the Köppen-Geiger climate classification [83, 115]. Although precipitation is part of the official classification, which can be found in appendix 3.B, we do not take it into account since we focus on air temperature variability. By doing so, and considering the area in which the stations were selected, only two parameters remain to determine the climate type of a station: minimum ($m$) and maximum ($M$) monthly mean temperatures. These induce four different types of climate: Mediterranean (Ca-type, $m > 0$°C, $M > 22$°C), Oceanic (Cb-type, $m > 0$°C, $M < 22$°C), Hot continental (Da-type, $m < 0$°C, $M > 22$°C), Temperate continental (Db-type, $m < 0$°C, $M < 22$°C) (see Figure 3.3).

Compared to the Köppen classification and the map of Europe presented in [115] and copied in appendix 3.B, our simplification has the effect of merging similar climate

types. More precisely, the large part of Spain originally classified as an arid cold steppe (BSk-type, mainly defined by very low precipitation) is now under the Mediterranean label, as well as Northern Italy and some parts of the Balkans (e.g. Serbia), which display the Cfa-type (same as Mediterranean climate with a wetter summer). They clearly have common features in their air temperature data with the surrounding Mediterranean regions and it is thus reasonable to merge them in the present work. Similarly, the Csb-type (mainly the North part of Portugal) has now the Oceanic tag since the only difference is the amount of precipitation during the summer season. Finally, the cold continental types (Dsa, Dfc and ET) only occur at high altitude in the selected area of Europe; data from weather stations located above 1000 meters of altitude will be discussed separately. Subsequently, one can see that neglecting precipitation leads to a union of similar climate types in a consistent way. In Europe, the main interest of taking precipitation into account is to differentiate some relatively small regions of the South half of the continent from the surrounding areas. This somehow brings more diversity in the climate classification, though air temperature remains the most significant and discriminant parameter. Besides, the intrinsic nature of precipitation measurements make it irrelevant to use techniques such as the WLM to extract valuable information.

As a last remark, stations close to 0.5°C of another type of climate are also associated with this second category and the most appropriate one will be chosen in due time. This is justified by the fact that climate may change over time; indeed, 12.2% of the stations display a different climate type when computed from 1951 to 1977 and from 1977 to 2003. Also, due to the lack of Da-type stations (in Europe, only found around the Black Sea), hot continental and temperate continental classes are merged into one category, i.e. Continental stations (D-type). The climate distribution among the stations is given by Figure 3.4.

### 3.3.2 A Hölder exponents-based climate classification

To check if the Köppen-Geiger climate classification in Europe can be regained from the present analysis, we first compute another parameter related to a signal of Hölder exponent $H$. Drawing on the scales used to obtain $H$ and on the wavelet coefficients $(c_{j,k})_{j,k}$, the quantity

$$N = \max_{j,k}\{|c_{j,k}|/2^{jH}\}$$

inspired by equation (1.1) is computed for each signal and called -abusively but for an easy-to-use purpose- the associated "norm"[1]. The mean of the norms is 17.61 and the standard deviation 3.55. The distribution of the couple of parameters $(H, N)$ is represented in Figure 3.5.

At this point, it is interesting to examine how a clustering algorithm regroups the points of the scatter plot displayed in Figure 3.5, without giving any information about the climate type of the stations. For that purpose, we use the standard $k$-means clustering algorithm ([16, 67]) in several ways; the results are displayed in Figure 3.6. First,

[1]It is actually a semi-norm on the uniform Hölder space $C^H$ [86].

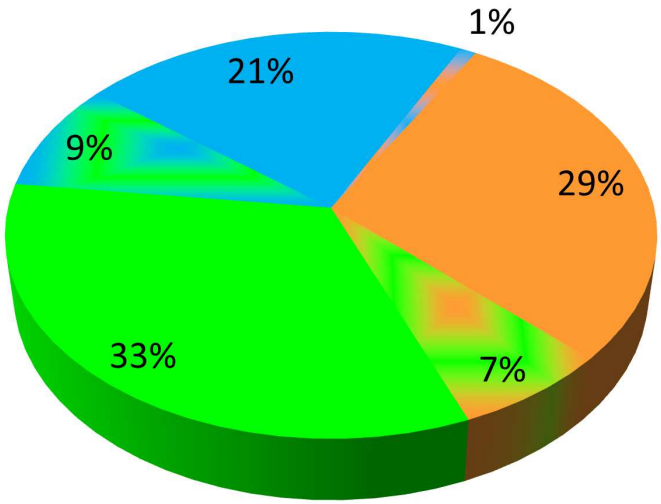


Figure 3.4: Climate distribution among the 115 weather stations. Green (Oceanic, Cb): 33%, Orange (Mediterranean, Ca): 29%, Blue (Continental, D): 21%, Cb and D: 9%, Ca and Cb: 7%, Ca and D: 1%.

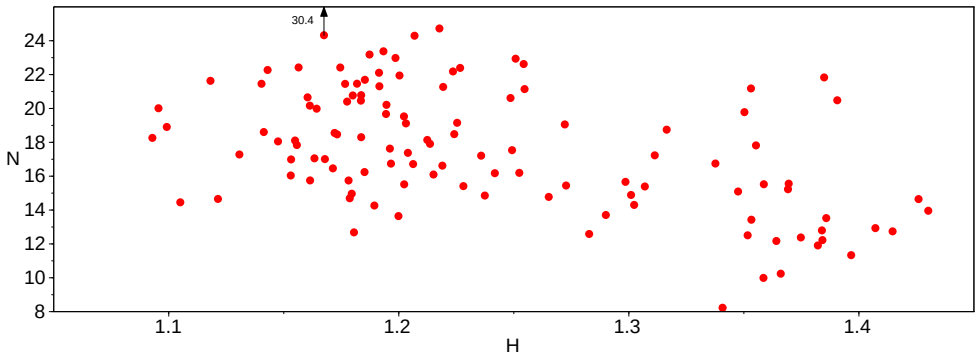


Figure 3.5: Distribution of the Hölder exponents and norms of the air temperature time series.

we cluster as if the norms were equal to zero, so that only $H$ influences the procedure. Since we will deal with three different types of climates in the following, we impose three clusters, and get the clustering $C_1$. Then, we proceed in the opposite way, i.e. as if the exponents were zero, which gives three other clusters, denoted by $C_2$. Therefore, combining these two sets of clusters, the scatter plot can be divided in nine parts, which gives a first "two-dimensional" separation of the points (see Figure 3.6), $C_3$. Our second choice is to perform directly a two-dimensional clustering with nine categories. However, since the values of $N$ are much greater than those of $H$, these two parameters are first re-normalized with equation (3.1) to have a comparable weight in the clustering process, before being reassigned to their initial values. This gives another cut-out of the cloud, $C_4$, which appears similar to $C_3$ (see Figure 3.6).

If we now study more closely the climate types of the stations present in the clusters of these four methods, it can be shown that the clusters in question generally regroup stations having the same climate. More precisely, if we attribute to each cluster the climate type which is the most abundant within, then 79% of the stations have the same climate as their cluster in $C_1$. Similarly, this percentage equals 78% for $C_2$. The combined cut-out $C_3$ assigns the right climate for 83% of the stations, and this percentage rises to 88% with $C_4$. This is interesting since the climate types were not among the parameters used in the clustering procedure. It thus indicates that it should be possible to relate the $(H, N)$ plane to the Köppen-Geiger climate classification. However, despite the fact that $C_3$ and $C_4$ provide stimulating results, it is difficult to describe their clusters analytically[2] and they do not allow to perform an elementary cut-out of the $(H, N)$ plane through few basic horizontal and vertical lines. Finally, the classifications obtained depend on the initial choice for the center of the clusters, and even iterations of the procedure (1000 were performed in each case) cannot guarantee that the optimum solution is found. As a consequence of these remarks, we will simplify our approach to exploit these considerations.

We introduce the Köppen classification in the $(H, N)$ plane of Figure 3.5: each point is now colored according to its climate type (see Figure 3.7). Since it appears that points with the same color are concentrated in the same areas, as foreseen in the previous paragraph, we may now try to cut the plane into rectangles to isolate the three climates. A simple possibility is to use only two vertical cuts (let us say at $H_1$ and $H_2$) and two horizontal cuts (let us say at $N_1$ and $N_2$), which gives 9 rectangles. As previously, each of them is then associated with the climate type that is the most abundant within, which gives rise to a new kind of climate classification. The best way to do so, i.e. the cut-out that gives the maximum coherence between this "Hölder-based classification" and the Köppen-Geiger climate classification, corresponds to the cuts where $H_1 = 1.186$, $H_2 = 1.275$, $N_1 = 14.81$ and $N_2 = 16.18$, which induces the classification given by Table 3.1. In this case, 93.9% of the stations are correctly classified, i.e. their Köppen climate type is recovered (see Figure 3.7).

We then perform a blind test on other weather stations in the same area to validate the Hölder-based classification. Since none of the remaining stations available on [49]

[2]They divide the $(H, N)$ plane in a kind of "broken stone mosaic".

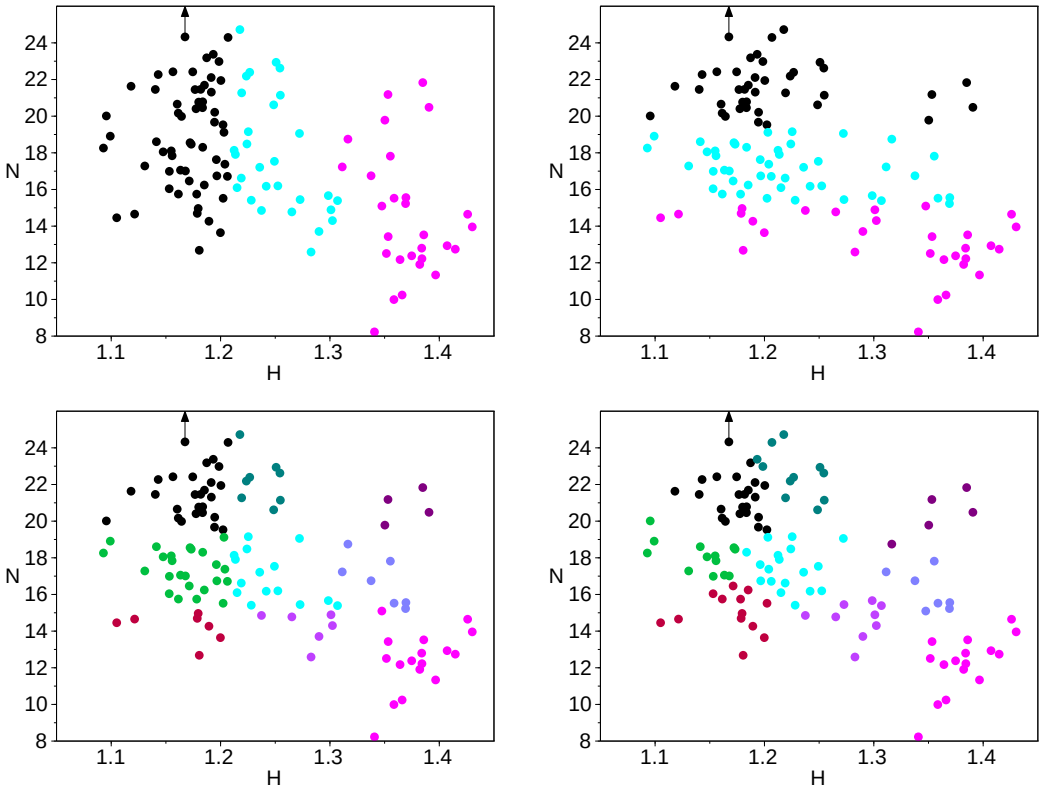


Figure 3.6: Top: $k$-means clustering of the scatter plot of Figure 3.5 if $N$ is considered 0 (left) then if $H$ is considered 0 (right). Bottom left: The combination of the previous clusters giving nine groups of points. Bottom right: Direct two-dimensional clustering in nine classes.

Table 3.1: The "Hölder-based" climate classification that best matches with Köppen's: almost 94% of the stations are correctly associated with their climate type.

| Hölder exponent | Norm | Climate type |
|---|---|---|
| $H < 1.186$ | all | Oceanic |
| $1.186 \leq H < 1.275$ | $N < 14.81$ | Mediterranean |
| | $14.81 \leq N < 16.18$ | Oceanic |
| | $16.18 \leq N$ | Continental |
| $1.275 \leq H$ | all | Mediterranean |

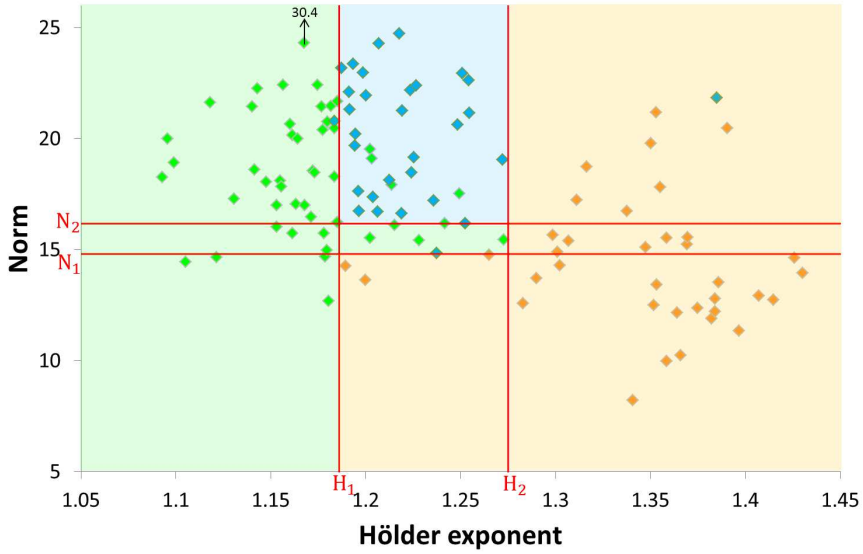


Figure 3.7: The diamonds (Green: Cb, Orange: Ca, Blue: D) represent the distribution of the Hölder exponents and norms of the 115 weather stations. Based on these two variables, the red lines cut the plane into rectangles that induce a climate classification (given by the color of the rectangles) designed to match as much as possible with the Köppen-Geiger classification. Almost 94% of the points have the same color as the rectangle in which they are located, which indicates that the classification based on Hölder exponents and norms matches with Köppen's.

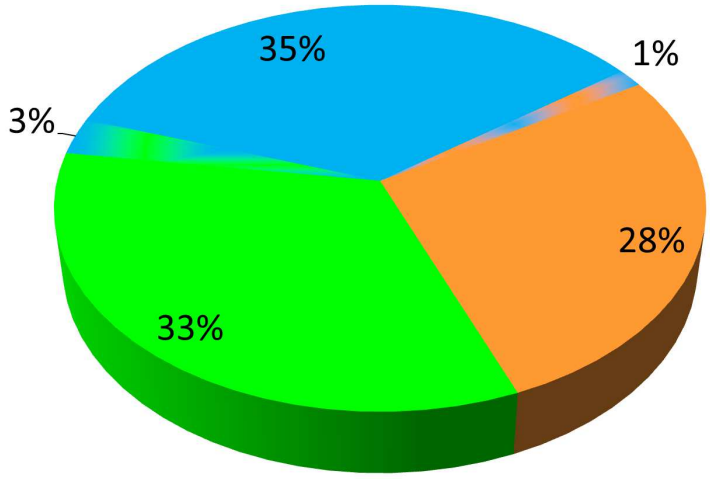


Figure 3.8: Climate distribution among the 69 weather stations selected for the blind test. Green (Oceanic, Cb): 33%, Orange (Mediterranean, Ca): 28%, Blue (Continental, D): 35%, Cb and D: 3%, Ca and D: 1%.

displayed at least 50 years of data between 1951 and 2003, we allowed shorter time series for the test (at least 40 years of data in that period). We found 69 stations exploitable for this experiment. As previously, we determine their Köppen climate types (their distribution is given by Figure 3.8) and we display the scatter plot representing the Hölder exponents and norms of these new stations (see Figure 3.9). Of course, the values of $H_1$, $H_2$, $N_1$ and $N_2$ are left unchanged, as well as the cut-out of the plane into rectangles and the colors of these rectangles. In this context, it appears that most of the points (88.4%) are still correctly classified. Figure 3.10 shows a global overview of the results (the first 115 stations and the 69 new ones).

As a reminder, all the stations used so far are placed below 1000 meters of altitude. One can thus wonder how Hölder exponents behave for weather stations located at high altitudes. We managed to find 10 stations above 1000 meters of altitude in the selected part of Europe which display at least 40 years of data between 1951 and 2003. These stations, as well as the associated information (Köppen climate, altitude) and results (Hölder exponent, norm, prescribed climate) can be found in Table 3.2. Let us remark that according to the simplified version of the Köppen classification described in this paper, these stations are unsurprisingly classified as "Db" (Continental), and none of them is 0.5° close to another type of climate. Nevertheless, following the original classification, Fichtelberg, Mont Aigoual and Zavizan are actually "Dc" type (minimum monthly mean temperature below 0°C and only between 1 and 3 months display a monthly mean temperature above 10°C), whereas Sonnblick, Säntis, Grand Saint-Bernard and Kredarica

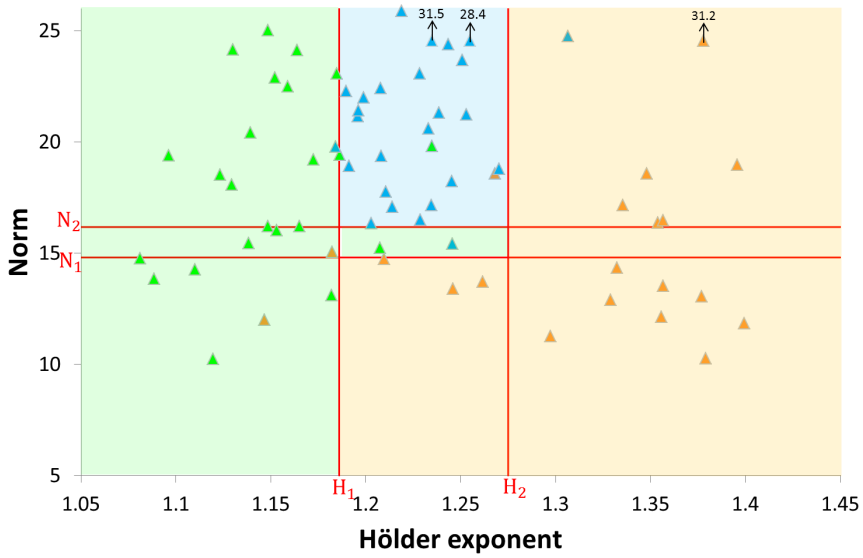


Figure 3.9: The triangles (Green: Cb, Orange: Ca, Blue: D) represent the distribution of the Hölder exponents and norms of the 69 weather stations selected for the blind test. In order to check if the classification based on the Hölder exponents and norms still match with Köppen's, the cut-out of the plane is left unchanged. Again, most of the points (almost 89%) have the same color as the rectangle in which they are located, which confirms the first result.

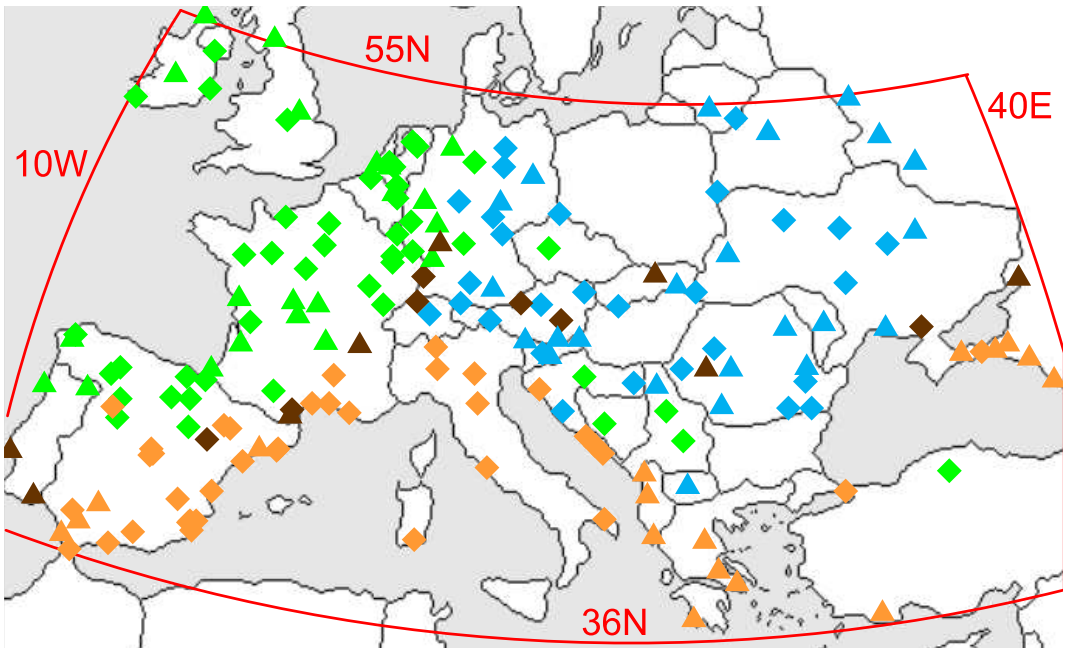


Figure 3.10: The first 115 weather stations are represented with diamonds, the 69 stations used for the blind test are represented with triangles. Each of them is colored as follows: Oceanic stations (Cb-type) in green, Continental stations (D-type) in blue, Mediterranean stations (Ca-type) in orange, and brown diamonds and triangles are used for stations for which the climate type is erroneously predicted by the Hölder-based classification.

Table 3.2: List of the stations located above 1000 meters of altitude (Alt. column, in meters) sorted by altitude and other relevant information. They are naturally classified as "Db" according to Köppen but as "Cb" with our method (Hclim column) because of their low Hölder exponent. This result seems surprising but is discussed in section 3.4

| Alt. | City (Country) | Tmax | Tmin | Köppen | $H$ | $N$ | Hclim |
|---|---|---|---|---|---|---|---|
| 1067 | Vojsko (Slovenia) | 15.6 | -2.6 | Db | 1.168 | 16.4 | Cb |
| 1180 | Ai-Petri (Ukraine) | 15.6 | -3.3 | Db | 1.163 | 19.5 | Cb |
| 1213 | Fichtelberg (Germany) | 12.1 | -4.7 | Db | 1.136 | 20.5 | Cb |
| 1567 | Mont Aigoual (France) | 12.9 | -1.9 | Db | 1.125 | 23.4 | Cb |
| 1594 | Zavizan (Croatia) | 13.1 | -4.1 | Db | 1.137 | 21.8 | Cb |
| 1894 | Navacerrada (Spain) | 16.2 | -0.7 | Db | 1.148 | 19.5 | Cb |
| 2472 | Gd.-St.Bernard (Swit.) | 7.6 | -7.9 | Db | 1.130 | 23.1 | Cb |
| 2502 | Säntis (Switzerland) | 5.9 | -8.0 | Db | 1.077 | 19.6 | Cb |
| 2514 | Kredarica (Slovenia) | 6.5 | -8.1 | Db | 1.098 | 23.2 | Cb |
| 3106 | Sonnblick (Austria) | 2.1 | -12.7 | Db | 1.123 | 20.8 | Cb |

are actually "E"-type of climate (maximum monthly mean temperature below 10°C). Table 3.2 indicates that all these stations located above 1000 meters of altitude are classified as "Cb" (Oceanic) according to our classification, due to their low Hölder exponents. Such a result may seem surprising at first sight but is discussed in section 3.4.

### 3.3.3 Comparison between ECA&D and NCEP data

It can be asked whether the results described above are dependent on the dataset used (i.e. ECA&D [49]). To answer that question, we perform the same analysis on surface air temperature data from the NCEP/NCAR Reanalysis Project [109]. In this dataset, our area of interest is divided in 27x10 pixels (1.875° of latitude, 1.905° of longitude), each of them associated with a signal of daily mean temperatures over the period 1951-2003. Figure 3.11 shows how Europe is divided in pixels, which are colored according to the mean temperature over the 53 years of data.

After removing the pixels corresponding to the different seas, we analyze the Hölder regularity and norms of the remaining air temperature profiles of the data with the WLM. We then associate two climates with each pixel: one based on the Köppen-Geiger classification, the other one using the Hölder-based classification (Table 3.1). With the same color code as usual, the resulting maps are represented in Figure 3.12 (top left and right) and match for 72% of the pixels.

To compare this result with those obtained from the ECA&D analysis, maps of the same format representing these latter are needed. We first quad the map of Figure 3.10 to have the same pixels as the NCEP maps, then we associate two climates with each

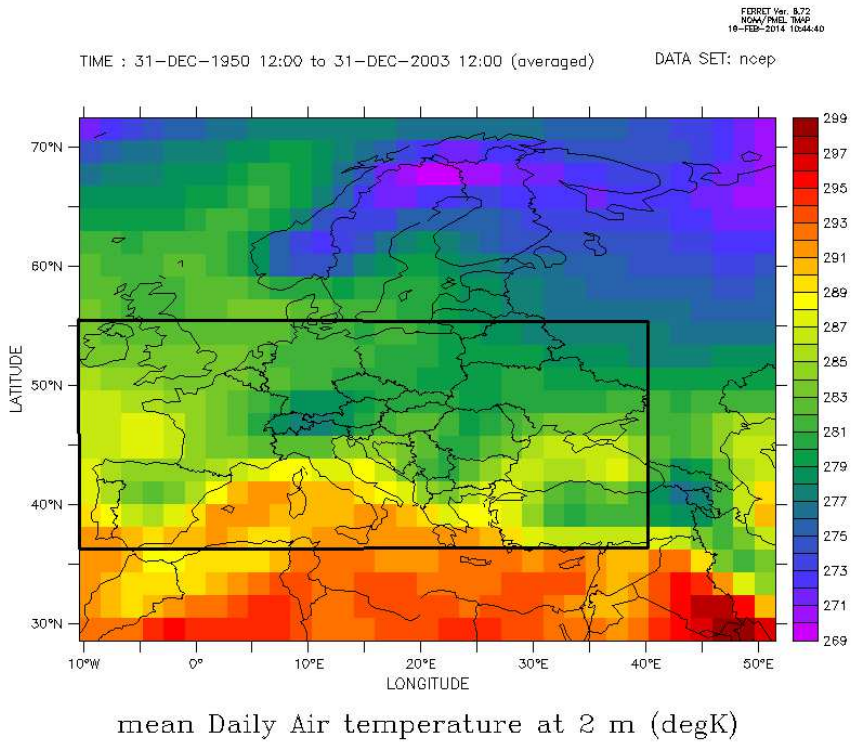


Figure 3.11: Illustration of the cut out of Europe into pixels by the NCEP data; the area of interest is the region included in the black box. The colors of the pixels represent the mean temperature of the corresponding region over the period 1951 to 2003. Image provided by the NOAA-ESRL Physical Sciences Division, Boulder Colorado from their Web site [109].

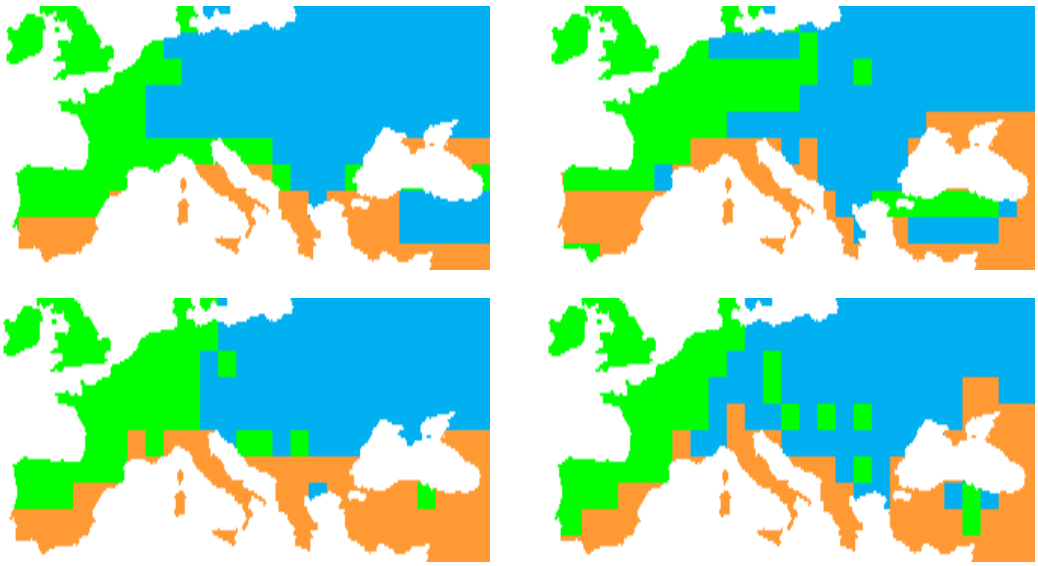

Figure 3.12: Top left (resp. right): Köppen (resp. Hölder)-based climate map obtained with the NCEP/NCAR dataset. The two maps match for 72% of the pixels. Bottom left (resp. right): Köppen (resp. Hölder)-based climate map obtained with air temperature data from ECA&D. The maps match for 85% of the pixels. Note that the Köppen maps (left) have a correspondence of only 78%.

pixel (using Köppen and Hölder-based classifications). In the case where a pixel does not include a weather station, the Hölder exponents, norms, minimum and maximum monthly mean temperatures are kriged to allow the two climate classifications. The resulting maps are represented in Figure 3.12 (bottom left and right) and match for 85% of the pixels. It can also be noted that the Köppen-based maps match for 78% of the pixels only.

## 3.4 Discussion

Let us now take a closer look at the results obtained in section 3.3.2. First, a major observation that stands out from Figure 3.7 is that the type of climate influences the regularity of the air temperature data. Indeed, it appears that Oceanic stations display the lowest Hölder exponents, Continental stations have intermediate values of $H$, and Mediterranean stations have the largest. This implies that, from a daily point of view, the Oceanic climate is more irregular, less stable than the two others, while the Mediterranean one is the most regular, the less variable in some way. It is an interesting fact that a method which does not use mean temperatures matches the Köppen-Geiger classification. They do not even use data at the same scale: we investigated the regularity at a daily scale while Köppen involves monthly mean temperatures. It thus also shows that the WLM is powerful enough to give results about a rather complex mathematical notion that are in good agreement with the intuition that surface air temperature variability is greater in Oceanic regions, whereas consecutive days and weeks are more likely to have the same air temperature in the South part of Europe. This could be explained by the fact that this region is more influenced by stable anticyclonic conditions, whereas the West coast of Europe is more impacted by the North Atlantic Oscillation and is therefore more subject to powerful winds, cold or humid air streams. These tend to trail off while entering the land, such that continental weather is slightly more regular. Such natural parameters affect the variability of air temperature, which is the principal ingredient of the Köppen-Geiger classification in Europe. Similarly, we can see that the Hölder exponent is the most important factor in the Hölder-based classification. If one does not take the norm into account, keeping only columns 1 and 3 of Table 3.1, the classification depends only on $H$: Oceanic if $H < H_1$, Continental if $H_1 < H < H_2$, Mediterranean if $H > H_2$. In this case, 89.6% of the 115 stations of reference and 84.1% of the 69 used for the confirmation test are still correctly associated with their climate type.

This brings us to the discussion about the stations that are not correctly associated with their Köppen climate type, which is the case for 7 out of the 115 initial stations (see Table 3.3). Except for Salzburg and Graz, these stations are located at the confluence of different climate types (see Figure 3.10 and [115]), which makes the climate more difficult to prescribe. As far as these two Austrian stations are concerned, an explanation could be found in the topography of the region. Located at the foot of the Alps, the climate of these stations (Db according to Köppen) is probably highly influenced by the presence

Table 3.3: List of the weather stations for which the prescribed climate type (Hclim) and Köppen climate type do not match among the 115 initial ones. Tmax and Tmin correspond to the maximum and minimum monthly mean temperatures (in Celsius degrees), defining the Köppen climate type of the stations (column "Köppen"). Column "Köp. 0.5°C" corresponds to other possible climate types that can be associated with the stations up to 0.5°C. The values of Hölder exponents and norms give the prescribed climate of the stations following our classification.

| Country | City | Tmax | Tmin | Köppen | Köp. 0.5°C | $H$ | $N$ | Hclim |
|---|---|---|---|---|---|---|---|---|
| Austria | Graz | 19.8 | -1.0 | Db | Db | 1.237 | 14.9 | Cb |
| Austria | Salzburg | 18.6 | -1.1 | Db | Db | 1.184 | 20.8 | Cb |
| France | Carcassonne | 22.1 | 6.1 | Ca | Cb | 1.214 | 17.9 | Db |
| France | Strasbourg | 19.4 | 1.2 | Cb | Cb | 1.202 | 19.5 | Db |
| Spain | Daroca | 22.0 | 4.3 | Ca | Cb | 1.249 | 17.5 | Db |
| Switzerland | Basel | 19.3 | 1.2 | Cb | Cb | 1.203 | 19.1 | Db |
| Ukraine | Askaniia Nova | 22.8 | -2.4 | Da | Da | 1.385 | 21.8 | Ca |

of the mountains nearby and is therefore different from Db-stations in Eastern Europe, which are easily detected by our classification. A comparable analysis can be made about the stations used for the blind test. As seen in Figure 3.9, 8 out of these 69 stations are not associated with their Köppen climate type (see Table 3.4). These errors can be explained by the same arguments as above. Perpignan (close to Carcassonne), Lyon, Mannheim and Rostov-On-Don are located in areas where different types of climates meet (see Figure 3.10). Although it cannot be clearly seen in Figure 3.10 due to the lack of stations in this region, Portugal undergoes both Oceanic and Mediterranean climate (see e.g. [115]), hence the same explanation still holds for Tavira and Lisbon. On the other hand, the cases of Poprad and Deva are similar to Graz and Salzburg since the former is located at the foot of the High Tatra Mountains and the latter is enclaved between the Apunesi Mountains and the Retezat Mountains in the Carpathian Mountains. Nonetheless, with a correspondence of 88.4%, the excellent results obtained in the confirmation test validate the "Hölder-based classification". This is reinforced by the fact that most of these new stations are located in countries in which none of the first 115 stations were situated (e.g. Greece, Portugal, Russia, see Figure 3.10).

The case of stations located above 1000 meters of altitude is interesting since they are all classified as Oceanic due to their low Hölder exponents. It is important to note that, at high altitude, climate is more impacted by the variability from the free atmosphere induced by the general circulation and thus tends to be very irregular, like the Oceanic climate. This feature, embodied by a decrease in the values of $H$ with altitude, is detected with the WLM. In addition, a closer examination at these stations reveals that 7 (out of 10) of them have a Hölder exponent lower than 1.137, which is smaller than 94% of the stations of reference, and a norm higher than 19.6. Only 2 out of the 115 initial stations

Table 3.4: List of the weather stations (among the 69 used for the blind test) for which the prescribed climate type (Hclim) and Köppen climate type do not match.

| Country | City | Tmax | Tmin | Köppen | Köp. 0.5°C | $H$ | $N$ | Hclim |
|---|---|---|---|---|---|---|---|---|
| France | Lyon | 20.9 | 2.8 | Cb | Cb | 1.235 | 19.8 | Db |
| France | Perpignan | 23.8 | 8.1 | Ca | Ca | 1.268 | 18.6 | Db |
| Germany | Mannheim | 19.7 | 1.4 | Cb | Cb | 1.186 | 19.4 | Db |
| Portugal | Lisbon | 22.8 | 11.4 | Ca | Ca | 1.147 | 12.0 | Cb |
| Portugal | Tavira | 23.7 | 11.4 | Ca | Ca | 1.182 | 15.1 | Cb |
| Romania | Deva | 22.3 | -1.9 | Da | Db | 1.246 | 15.4 | Cb |
| Russia | Rostov-On-Don | 23.3 | -4.1 | Da | Da | 1.307 | 24.7 | Ca |
| Slovakia | Poprad | 15.8 | -4.8 | Db | Db | 1.184 | 19.8 | Cb |

have such values for $H$ and $N$. Therefore, it is reasonable to assert that our classification could be enhanced by defining a mountain climate for stations having $H < 1.137$ and $N > 19.6$. Such a category could not have been guessed from the initial results and should be considered with caution due to the restricted number of stations above 1000 meters at our disposal. Besides, among the 3 remaining ones, Navacerrada (Spain) is somehow a nonstandard high altitude location in Europe (see [115]) and Vojsko and Ai Petri are those with the lowest altitude in this category (resp. 1067 and 1180 meters). It is thus probable that the decrease in the value of $H$ due to altitude is limited in their case.

Finally, we can comment the results obtained with the NCEP dataset in section 3.3.3. One can notice that the three types of climate are still well discernible and well located in Figure 3.12. Also, it appears that the Köppen-Hölder correlation between the maps obtained from ECA&D is higher than the correspondence between the Köppen maps from NCEP and ECA&D, which explains the relatively low correspondence percentage between the Köppen-Hölder NCEP maps. However, the global tendencies remain visible and detectable with the NCEP/NCAR data, which emphasizes the independence of the results from the dataset and stresses the fact that surface air temperature variability, through Hölder exponents, is correlated with climate types in Europe.

## 3.5 Conclusion

In conclusion, we first showed that the Hölder exponents from surface air temperature data in Europe obtained with the WLM are anti-correlated with the associated standard deviation of pressure anomalies, while those given by the MFDFA are not. Then, we established a climate classification based on these Hölder exponents that allowed us to recapture the renowned Köppen-Geiger climate classification. It appeared that Oceanic stations display the lowest Hölder exponents, Continental stations have intermediate exponents, and Mediterranean stations have the largest. We performed a blind test to

check the efficiency of our classification and we investigated the particular nature of stations located at high altitude. The computations performed with another dataset confirmed that, as quantified by the notion of Hölder exponent, temperature variability is correlated with climate types in Europe.

The results presented in this chapter, as well as the method used, could be useful to test and compare different climate models. It could help in the detection of abnormalities in reanalyses or could indicate if some factors tend to "smoothen" the temperature curves. Apart from these potential impacts in climate modeling and, to some extend, to weather forecast, the issue of a generalization to other parts of the world can be considered. Indeed, the discussion about stations placed at high altitude raises the question of the detection of completely different types of climates, such as Tropical, Dry, or Polar climates. Of course, the current version of the Hölder-based classification is not able to detect them provided that it is calibrated for Europe and that we do not know which part of the $(H, N)$ plane they would occupy. It is possible that they are not clearly discernible from some European climates from a Hölder point of view. However, is it really relevant to try to contrast the Hölder exponents of Madrid and of Brasilia if they accidentally lie close to each other in the $(H, N)$ plane? Maybe they have a similar regularity although Brasilia is globally much wetter and hotter, so that there would be actually no mistake by placing them in the same area of the plane. The real interesting problem would be to establish a Hölder-based classification specific for e.g. South America that is able to distinguish the different types of climates present in that particular consistent geographic area. In line with this example, we could imagine that the impact of precipitation on daily temperatures could be observed in data from this region, while it is not the case in Europe. Moreover, it is always possible to add new features in relation with $H$ and $N$ if we really want to ramify our classification. Indeed, it may be good to recall that the Köppen-Geiger classification uses a dozen of indicators related to temperature and precipitation to distinguish up to 30 types of climates worldwide. Be that as it may, the results obtained for Europe are more than encouraging and there is clearly an exciting challenge ahead with the study of other continents and with the prospect of mapping the world according to the Hölder regularity of surface air temperature data.

*We acknowledge the data providers in the ECA&D project [136] (data and metadata available at [49]) and in the NCEP/NCAR Reanalysis Project (GHCN Gridded V2 data were provided by the NOAA-OAR-ESRL PSD, Boulder, Colorado, USA, from their Web site at [109]).*

# Appendix

## 3.A Multifractal detrended fluctuation analysis

The main ideas of the MFDFA method applied on a data series $x_k$ of length $N$ are briefly described below. More details can be found in e.g.[81].

1) Compute the "profile"
$$Y(i) = \sum_{k=1}^{i} x_k - \bar{x}$$
where $\bar{x}$ is the mean of the series.

2) For each scale (i.e. "length") $s > 0$, divide the profile into $N_s$ non-overlapping segments of length $s$.

3) For each segment $i = 1, ..., N_s$, compute the variance of the detrended segment, i.e.
$$F^2(s,i) = \frac{1}{s}\sum_{k=1}^{s}(Y((i-1)s+k) - y_i(k))^2$$
where $y_i(k)$ is the least-square fitting polynomial of order $m$ (fixed in advance, $m = 1$ for linear fit, $m = 2$ for quadratic fit, etc.) of the segment.

4) Compute the fluctuation function
$$F_q(s) = \left(\frac{1}{N_s}\sum_{i=1}^{N_s}(F^2(s,i))^{q/2}\right)^{1/q}$$
for each value of $q$.

5) For each value of $q$, compute $\zeta(q)$ as the slope of the linear regression of $s \mapsto \log F_q(s)$.

Then, $\zeta(q)$ plays the same role as $\eta(q)$ in the WLM, i.e. if $\zeta$ is linear, then its slope is the scaling exponent of the signal.

## 3.B Köppen-Geiger classification

Table 3.5 presents the Köppen-Geiger climate classification as given in [115]. The criteria used are the following:

- MAP = mean annual precipitation
- MAT = mean annual temperature

- $T_{hot}$ = temperature of the hottest month[3]
- $T_{cold}$ = temperature of the coldest month
- $T_{mon10}$ = number of months where the temperature is above 10°C
- $P_{dry}$ = precipitation of the driest month
- $P_{sdry}$ = precipitation of the driest month in summer
- $P_{wdry}$ = precipitation of the driest month in winter
- $P_{swet}$ = precipitation of the wettest month in summer
- $P_{wwet}$ = precipitation of the wettest month in winter
- $P_{threshold}$ = varies according to the following rules: if 70% of MAP occurs in winter then $P_{threshold}$ = 2 x MAT, if 70% of MAP occurs in summer then $P_{threshold}$ = 2 x MAT + 28, otherwise $P_{threshold}$ = 2 x MAT + 14
- Summer (winter) is defined as the warmer (cooler) six month period of ONDJFM and AMJJAS.

Figure 3.13 presents the Köppen-Geiger climate map for Europe.

[3]In the sense of maximum monthly mean temperature.

Table 3.5: Description of Köppen climate symbols and defining criteria.

| 1st | 2nd | 3rd | Description | Criteria* |
|---|---|---|---|---|
| A | | | Tropical | $T_{cold} \geq 18$ |
| | f | | - Rainforest | $P_{dry} \geq 60$ |
| | m | | - Monsoon | Not (Af) & $P_{dry} \geq 100 - MAP/25$ |
| | w | | - Savannah | Not (Af) & $P_{dry} < 100 - MAP/25$ |
| B | | | Arid | $MAP < 10 \times P_{threshold}$ |
| | W | | - Desert | $MAP < 5 \times P_{threshold}$ |
| | S | | - Steppe | $MAP \geq 5 \times P_{threshold}$ |
| | | h | - Hot | $MAT \geq 18$ |
| | | k | - Cold | $MAT < 18$ |
| C | | | Temperate | $T_{hot} > 10$ & $0 < T_{cold} < 18$ |
| | s | | - Dry Summer | $P_{sdry} < 40$ & $P_{sdry} < P_{wwet}/3$ |
| | w | | - Dry Winter | $P_{wdry} < P_{swet}/10$ |
| | f | | - Without dry season | Not (Cs) or (Cw) |
| | | a | - Hot Summer | $T_{hot} \geq 22$ |
| | | b | - Warm Summer | Not (a) & $T_{mon10} \geq 4$ |
| | | c | - Cold Summer | Not (a or b) & $1 \leq T_{mon10} < 4$ |
| D | | | Cold | $T_{hot} > 10$ & $T_{cold} \leq 0$ |
| | s | | - Dry Summer | $P_{sdry} < 40$ & $P_{sdry} < P_{wwet}/3$ |
| | w | | - Dry Winter | $P_{wdry} < P_{swet}/10$ |
| | f | | - Without dry season | Not (Ds) or (Dw) |
| | | a | - Hot Summer | $T_{hot} \geq 22$ |
| | | b | - Warm Summer | Not (a) & $T_{mon10} \geq 4$ |
| | | c | - Cold Summer | Not (a, b or d) |
| | | d | - Very Cold Winter | Not (a or b) & $T_{cold} < -38$ |
| E | | | Polar | $T_{hot} < 10$ |
| | T | | - Tundra | $T_{hot} > 0$ |
| | F | | - Frost | $T_{hot} \leq 0$ |

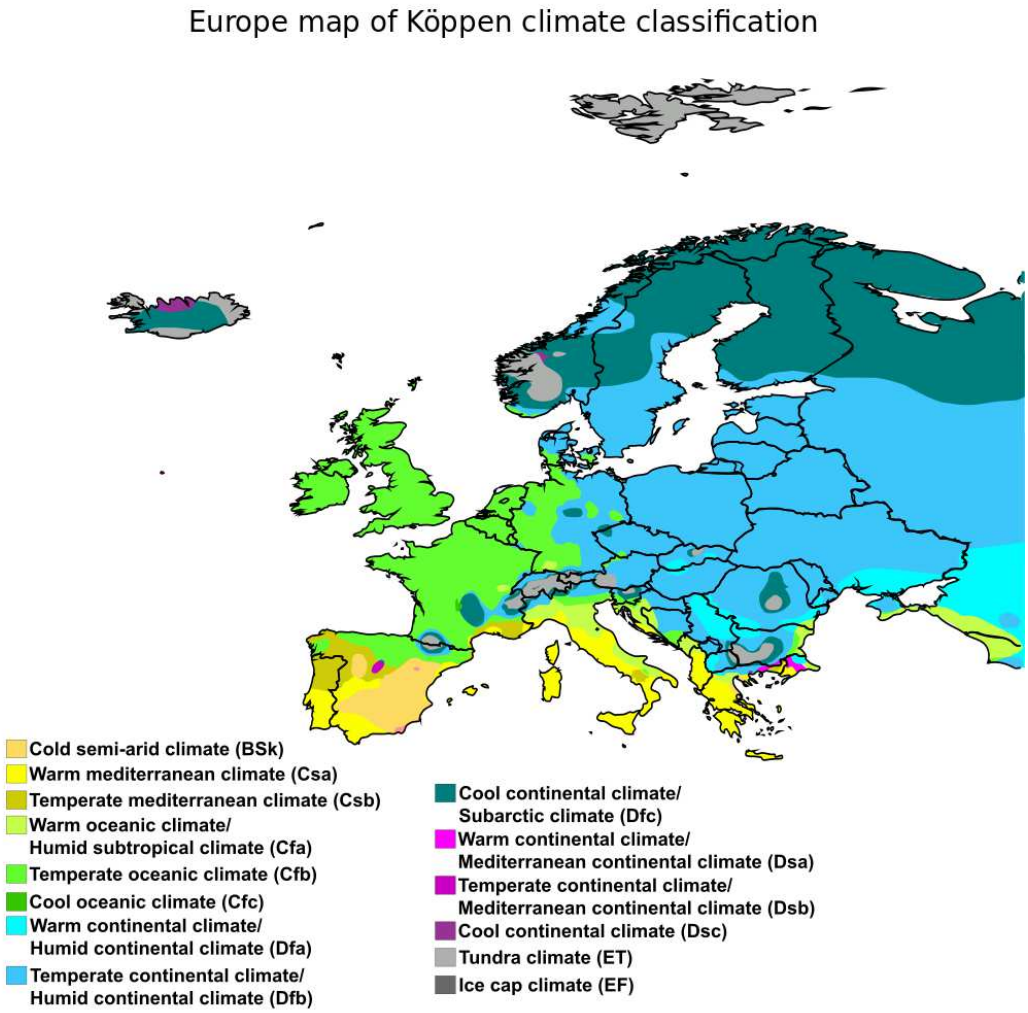


Figure 3.13: Europe map of Köppen-Geiger climate classification, from [115, 156].

# Part II

# Wavelet-based time-frequency analysis

# Chapter 4

# Continuous wavelet transform and border effects

This chapter is somehow the counterpart of chapter 1 for the continuous wavelet transform. It will be used in this thesis in the context of the extraction of oscillating components from a signal. The theoretic part is again reduced to the properties needed in chapters 5 and 6 whereas a major difference between theory and practice - the border effects - is studied more deeply and is the main subject of the chapter. Note that, throughout part II, we consider that every function (including wavelets) is defined on $\mathbb{R}$ unless stated otherwise.

## 4.1 A convenient property

**Notation 4.1.1.** The Fourier transform of a function $f$ is noted $\hat{f}$. If $f \in L^1(\mathbb{R})$, then

$$\hat{f}(\xi) = \int_{\mathbb{R}} e^{-i\xi x} f(x) dx.$$

Given a wavelet $\psi$, the continuous wavelet transform (CWT) of a function $f \in L^2(\mathbb{R})$ at position $b$ and at scale $a > 0$ is defined as

$$W_f^{\psi}(a,b) = \int_{\mathbb{R}} f(x) \bar{\psi}\left(\frac{x-b}{a}\right) \frac{dx}{a} \tag{4.1}$$

where $\bar{\psi}$ is the complex conjugate of $\psi$.

**Remarks 4.1.2.** The superscript $\psi$ will not be written anymore since it does not play any role in the following. Also, as mentioned in chapter 1, more information on the theoretical properties of wavelets can be found in the seminal works [34, 96, 98, 100].

A wavelet $\psi$ is called a progressive wavelet if $\hat{\psi}(\xi) = 0$ if $\xi \leq 0$. Progressive wavelets have the following convenient property ([35]).

**Proposition 4.1.3.** *If $\psi$ is a progressive wavelet and if $f(x) = \cos(\omega x)$ with $\omega > 0$, then*

$$W_f(a,b) = \frac{1}{2} e^{ib\omega} \overline{\hat{\psi}(a\omega)}.$$

*Proof.* From Parseval-Plancherel's theorem, it comes

$$\begin{aligned} W_f(a,b) &= \int_{\mathbb{R}} f(x) \bar{\psi}\left(\frac{x-b}{a}\right) \frac{dx}{a} \\ &= \frac{1}{2\pi} \int_{\mathbb{R}} \hat{f}(\xi) a e^{ib\xi} \overline{\hat{\psi}(a\xi)} \frac{d\xi}{a}. \end{aligned}$$

Since

$$\hat{f}(\xi) = \pi(\delta(\xi - \omega) + \delta(\xi + \omega))$$

where $\delta(.)$ is the Dirac delta-distribution, we get

$$\begin{aligned} W_f(a,b) &= \frac{1}{2} \int_{\mathbb{R}} (\delta(\xi - \omega) + \delta(\xi + \omega)) e^{ib\xi} \overline{\hat{\psi}(a\xi)} d\xi \\ &= \frac{1}{2} (e^{ib\omega} \overline{\hat{\psi}(a\omega)} + e^{-ib\omega} \overline{\hat{\psi}(-a\omega)}) \\ &= \frac{1}{2} e^{ib\omega} \overline{\hat{\psi}(a\omega)} \end{aligned}$$

where the last equality comes from the fact that $\psi$ is a progressive wavelet and that $a\omega > 0$. □

In the context of time-frequency analysis, it is recommended to use a wavelet well-located in the frequency domain ([141]). In this work, we use the Morlet-like wavelet $\psi$ defined by its Fourier transform as

$$\hat{\psi}(\xi) = \sin\left(\frac{\pi\xi}{2\Omega}\right) e^{\frac{-(\xi-\Omega)^2}{2}} \tag{4.2}$$

with $\Omega = \pi\sqrt{2/\ln 2}$, which has one vanishing moment ([104]). In the time domain, we have

$$\psi(x) = \frac{e^{i\Omega x}}{2\sqrt{2\pi}} e^{-\frac{(2\Omega x + \pi)^2}{8\Omega^2}} \left(e^{\frac{\pi x}{\Omega}} + 1\right).$$

Since $\left|\hat{\psi}(\xi)\right| < 10^{-5}$ if $\xi \leq 0$, $\psi$ will be considered as a progressive wavelet. Moreover, it comes that the function[1]

$$a \mapsto |W_f(a,b)| = \frac{1}{2} |\hat{\psi}(a\omega)|$$

[1]Since $\hat{\psi}$ is a real-valued function, we have $\overline{\hat{\psi}} = \hat{\psi}$.

reaches a global maximum at some scale $a^*$ which satisfies $a^* = \Omega/\omega$. As a consequence, if $\omega$ is unknown, it can be obtained as $\omega = \Omega/a^*$ and thus

$$W_f(a^*, b) = \frac{1}{2} e^{ib\omega}.$$

The initial function $f$ can then be easily recovered from the real part of its CWT as

$$\begin{aligned} f(x) &= 2\Re W_f(a^*, x) \\ &= 2|W_f(a^*, x)| \cos(\arg(W_f(a^*, x))). \end{aligned} \tag{4.3}$$

## 4.2 Border effects

### 4.2.1 A practical approach

In practice, the signal has a finite length and thus needs to be padded at its edges to obtain the whole CWT. The chosen padding irremediably flaws a certain proportion of the wavelet coefficients located at the beginning and at the end of the signal, which is known as the "border effects" or "edge effects". While this problem is well-known by practitioners, it is usually simply recommended to be careful about the interpretation of the associated coefficients [113, 141]. Some of the most common possibilities are the zero padding, the constant padding and the symmetrization of the signal. In [134], the authors suggest to pad the signal with a Fourier series extension of the signal, which appears interesting but only one simple example is presented. Be that as it may, it appeared relatively difficult to find interesting works that provide a deeper analysis of border effects. This is why we decided to investigate this topic more closely. Since only the zero padding has a "universal" overtone, in the sense that the padded values are independent of the signal, it will be our main subject of interest. Moreover, "on average", it has the same mean (i.e. zero) as a periodic oscillating component, regardless the period. Therefore, in this section, we try to estimate how the zero padding interferes with the CWT of a cosine in practice.

As a matter of example, we perform the CWT of the 32-units periodic function

$$f(x) = \cos\left(\frac{2\pi}{32} x\right)$$

computed for $x$ ranging from -255 to 0 by steps of 1 unit. For the computation of the CWT, we impose that $f(x) = 0$ for $x < -255$ and for $x > 0$. The function

$$(a, b) \mapsto |W_f(a, b)|$$

is commonly referred to as a time-frequency (TF) representation of $f$ because the variables $b$ and $x$ are usually time variables and a given scale $a$ can be seen as the frequency at which the signal is analyzed (in the same spirit as in the Fourier transform). This

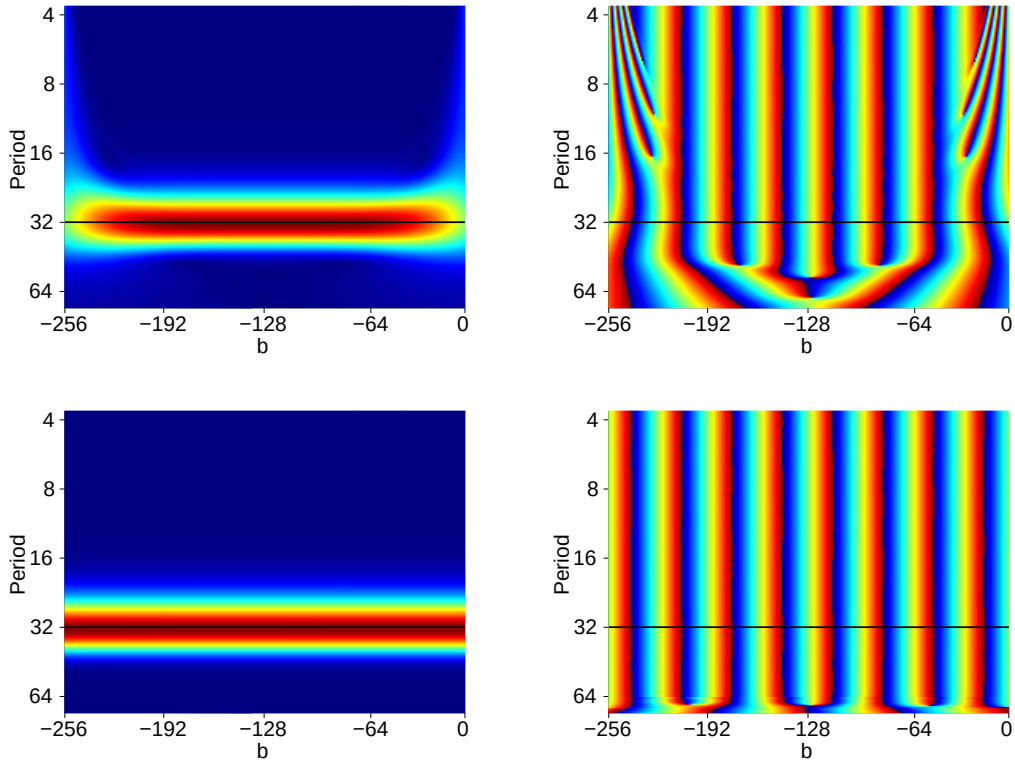


Figure 4.1: Top left: Modulus of the CWT of $f(x) = \cos(2\pi x/32)$ defined on $[-255, 0]$ with the zero padding. The values range from 0 (blue) to 0.5 (red). Top right: Argument of the CWT of $f$; the values range from $-\pi$ (blue) to $\pi$ (red). Bottom: The expected modulus and argument of the CWT of $f$, with no border effects. The black lines indicate the wavelet coefficients at period 32 that will be used to reconstruct $f$ from its CWT.

function thus indicates at which scales/frequencies and time spans the energy of the signal is located, which generally guides the rest of the analysis. It is plotted in Figure 4.1, where the scales $a$ on the vertical axis have been converted into the corresponding periods for the sake of clarity. The function $(a, b) \mapsto \arg(W_f(a, b))$ is also plotted, as well as their unbiased counterparts, i.e. the two expected TF planes with no border effects. While it can be seen that the signal has its energy located around the period 32 (as expected) independently of the value of $b$, the influence of the zero padding is also clearly noticeable.

We can extract the modulus (or amplitude) and argument of the CWT at period 32, i.e. along the black lines in Figure 4.1. They are displayed in Figure 4.2. It can be observed that the influence of the zero padding in the present case is particularly strong as far as the amplitude is concerned, dropping by almost a half at the beginning and

at the end of the signal. This observation makes sense since the zero padding drags the wavelet coefficients down so that they get closer to 0. Regarding the argument on the top right plot, it is not clear how it differs from the expected one. In order to bypass this problem, the argument can be unwrapped by adding appropriate multiples of $2\pi$ each time it decreases. This procedure is conducted for both the obtained and the expected arguments starting from the $128^{\text{th}}$ data point, in the middle of the signal, where they match perfectly. The operation gives the third plot in Figure 4.2, which is still not easy to interpret. However, the difference between these two signals ("obtained minus expected", see last plot) reveals that the argument obtained in the present case with the zero padding increases as $b$ draws closer to the end of the signal. This indicates that the instantaneous frequency "spins" too fast compared to its expected behavior. Again, such an observation can be explained: at the right-hand border, the signal drops abruptly from 1 to 0, which somehow forces a compression of the argument of the wavelet coefficients in order to better replicate this sudden jump.

Using equation (4.3), we can extract the component associated to period 32. Due to the significant decrease in amplitude, it only matches with the initial signal on an interval of the type $[-128-N, -128+N]$ almost unaffected by border effects, where $N$ depends on the width of the wavelet ([141]); this is shown in Figure 4.3. For the wavelet used in this work, numerical experiments showed that when a cosine sampled every unit is analyzed at a scale $a$, corresponding to a period $p$, there are at most $\approx \sqrt{2}p$ coefficients at each border that differ of more than 5% from their correct value. Moreover, the impact of the increasing argument of the so-obtained component is barely noticeable in this case; the amplitude is the dominant source of error. Correcting the amplitude but not the argument reduces the maximum absolute error to 0.03.

### 4.2.2 A more analytical approach

The previous section showed how the border effects influence the CWT of a cosine in practice. Now, we try to estimate these effects from a more analytical point of view and to derive a computable expression for a corrective factor. More precisely, we consider

$$f(x) = \begin{cases} \cos(\omega x) & \text{if } x \leq 0 \\ 0 & \text{if } x > 0 \end{cases}$$

which can be rewritten as $f(x) = \cos(\omega x)H(-x)$ where $H$ is the Heaviside step function. We assume that $\omega$ is known and we naturally investigate the scale $a^* = \Omega/\omega$. From the previous section, it can be conjectured that

$$W_f(a^*, b) = \frac{1}{2} e^{ib\omega} z_\omega^*(b) \tag{4.4}$$

where $z_\omega^* : \mathbb{R} \to \mathbb{C}$ has the following properties:

1) $0 < |z_\omega^*(b)| < 1 \quad \forall b \in \mathbb{R}$,

2) $b \mapsto |z_\omega^*(b)|$ is decreasing,

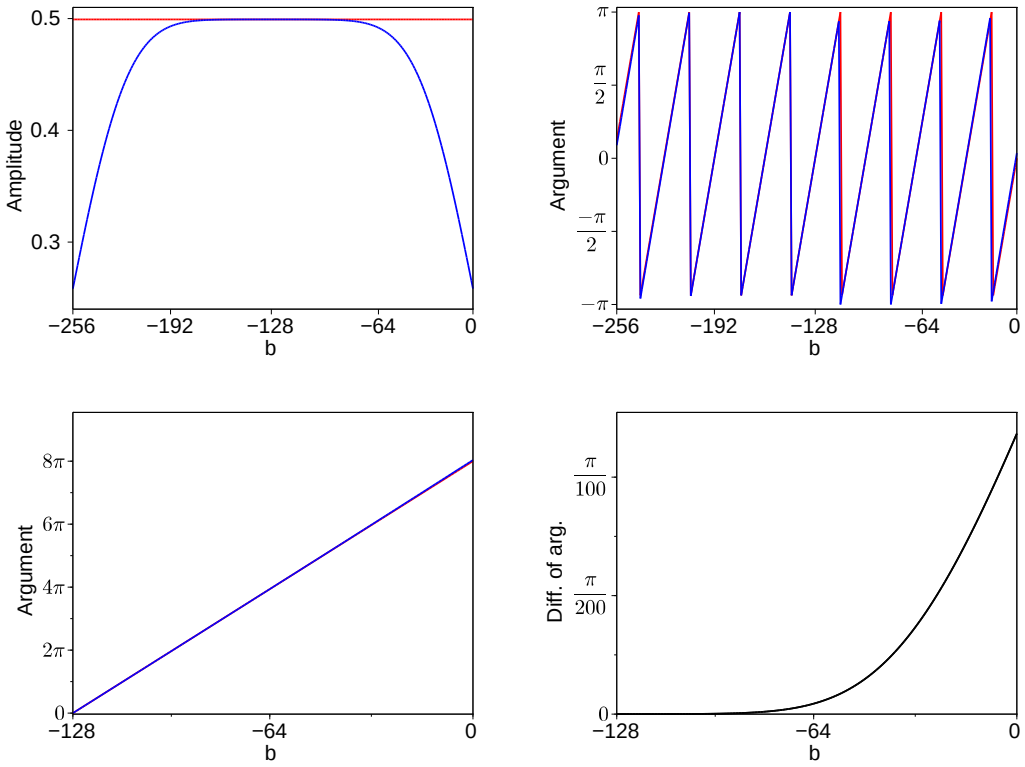


Figure 4.2: Top left: In blue, the modulus of the CWT of $f$ with the zero padding along the black ridge in Figure 4.1. In red, the expected modulus without border effects. Top right: The same with the argument of the CWT of $f$ along the ridge. Bottom left: "Unwrapped" versions of the arguments. The blue one masks the red one. Bottom right: Difference between the obtained unwrapped argument and the expected one.

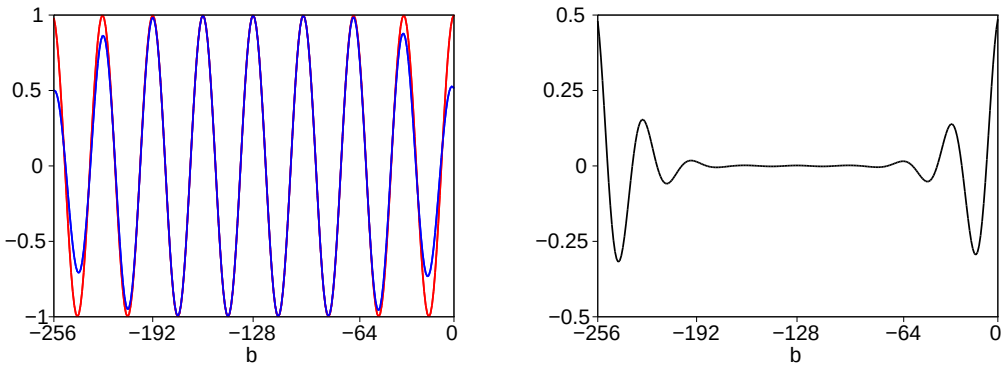


Figure 4.3: Left: The initial signal (red) and the reconstructed one (blue) from the CWT. Right: the difference between them, i.e. the error in the reconstruction.

3) $\arg(z_\omega^*(b)) > 0 \quad \forall b \in \mathbb{R}$,

4) $b \mapsto \arg(z_\omega^*(b))$ is increasing.

Given $b$, we thus try to find an appropriate compensation $z_\omega^*(b)$ with these properties, numerically computable, and such that

$$2\Re\left(\frac{W_f(a^*, b)}{z_\omega^*(b)}\right) = \cos(\omega b)$$

for negative values of $b$.

For that purpose, we mimic the procedure of section 4.1. First, the Fourier transform of $f$ can be obtained as

$$\begin{aligned}
\hat{f}(\xi) &= \frac{1}{2\pi}\left(\pi(\delta(\xi-\omega)+\delta(\xi+\omega)) * \hat{H}(-\xi)\right) \\
&= \frac{1}{2}\left((\delta(\xi-\omega)+\delta(\xi+\omega)) * (\pi\delta(\xi)+\frac{i}{\xi})\right) \\
&= \frac{1}{2}\left(\pi\delta(\xi-\omega)+\frac{i}{\xi-\omega}+\pi\delta(\xi+\omega)+\frac{i}{\xi+\omega}\right) \\
&= \frac{1}{2}\hat{g}(\xi)+\frac{\xi i}{\xi^2-\omega^2}
\end{aligned}$$

where $g(x) = \cos(\omega x)$ for $x \in \mathbb{R}$. Even if the conditions for Parseval-Plancherel's formula do not fully hold, we can hope to have

$$W_f(a,b) \approx \frac{1}{4}e^{ib\omega}\hat{\psi}(a\omega) + \frac{i}{2\pi}\int_{\mathbb{R}} \frac{\xi}{\xi^2-\omega^2}\hat{\psi}(a\xi)e^{ib\xi}d\xi.$$

As mentioned, the scale of interest is $a^* = \Omega/\omega$. With the change of variables $\xi = \omega x$, we thus get

$$W_f(a^*, b) \approx \frac{1}{4}e^{ib\omega} + \frac{i}{2\pi}\int_{\mathbb{R}} \frac{x}{x^2-1}\hat{\psi}(\Omega x)e^{ib\omega x}dx. \tag{4.5}$$

We now consider the remaining integral as a principal value integral and hope it converges, so that we can work with numerically computable quantities. Besides, if we assume that $\psi$ is a progressive wavelet, then $\hat{\psi}$ vanishes for negative arguments, and since $\hat{\psi}$ is symmetric with respect to $\Omega$, we can consider that $\hat{\psi}$ is supported in $[0, 2\Omega]$. It comes that $\hat{\psi}(\Omega x)$ vanishes outside $[0, 2]$. Also, if we write

$$\mathrm{I} = P.V. \int_0^2 \frac{x}{x^2-1}\hat{\psi}(\Omega x)e^{ib\omega x}dx = \lim_{\epsilon\to 0}\left(\int_0^{1-\epsilon}\ldots + \int_{1+\epsilon}^{2}\ldots\right),$$

then with the change of variables $y = 2 - x$ for the second part and given that $\hat{\psi}(\Omega(2-y)) = \hat{\psi}(\Omega y)$, we get

$$\begin{aligned}
\mathrm{I} &= \lim_{\epsilon\to 0}\int_0^{1-\epsilon} \frac{x}{x^2-1}\hat{\psi}(\Omega x)e^{ib\omega x} + \frac{2-x}{(2-x)^2-1}\hat{\psi}(\Omega x)e^{ib\omega(2-x)}dx \\
&= e^{ib\omega}\lim_{\epsilon\to 0}\int_0^{1-\epsilon}\frac{\hat{\psi}(\Omega x)}{x-1}\left(\frac{x}{x+1}e^{-ib\omega(1-x)} + \frac{2-x}{x-3}e^{ib\omega(1-x)}\right)dx \\
&= e^{ib\omega}\lim_{\epsilon\to 0}\int_0^{1-\epsilon}\frac{\hat{\psi}(\Omega x)}{x-1}\left(\frac{-2(x-1)}{(x+1)(x-3)}\cos(b\omega(1-x))\right. \\
&\qquad\qquad \left. + i\frac{-2(x^2-2x-1)}{(x-3)(x+1)}\sin(b\omega(1-x))dx\right) \\
&= 2e^{ib\omega}\left(\int_0^1 \frac{\hat{\psi}(\Omega x)}{(x+1)(3-x)}\cos(b\omega(1-x))dx\right. \\
&\qquad\qquad \left. + i\int_0^1 \frac{(x^2-2x-1)\hat{\psi}(\Omega x)}{(x^2-1)(3-x)}\sin(b\omega(1-x))dx\right).
\end{aligned}$$

As a consequence, we finally get

$$W_f(a^*, b) \approx \frac{1}{2}e^{ib\omega}z_\omega(b) \tag{4.6}$$

with

$$\Re(z_\omega(b)) = \frac{1}{2} - \frac{2}{\pi}\int_0^1 \frac{(x^2-2x-1)\hat{\psi}(\Omega x)}{(x^2-1)(3-x)}\sin(b\omega(1-x))dx \tag{4.7}$$

and

$$\Im(z_\omega(b)) = \frac{2}{\pi}\int_0^1 \frac{\hat{\psi}(\Omega x)}{(x+1)(3-x)}\cos(b\omega(1-x))dx, \tag{4.8}$$

where it can be noted that both integrals make sense. From a numerical point of view, it appears that the complex number $z_\omega(b)$ defined by equations (4.7) and (4.8) has the desired properties, i.e. $|z_\omega(b)| < 1$, $b \mapsto |z_\omega(b)|$ is decreasing, $\arg(z_\omega(b)) > 0$ and $b \mapsto \arg(z_\omega(b))$ is increasing, as shown in Figure 4.4. It can also be seen that $z_\omega(b)$ is close to the expected $z^*_\omega(b)$ of equation (4.4). Besides, drawing on equation (4.6), it

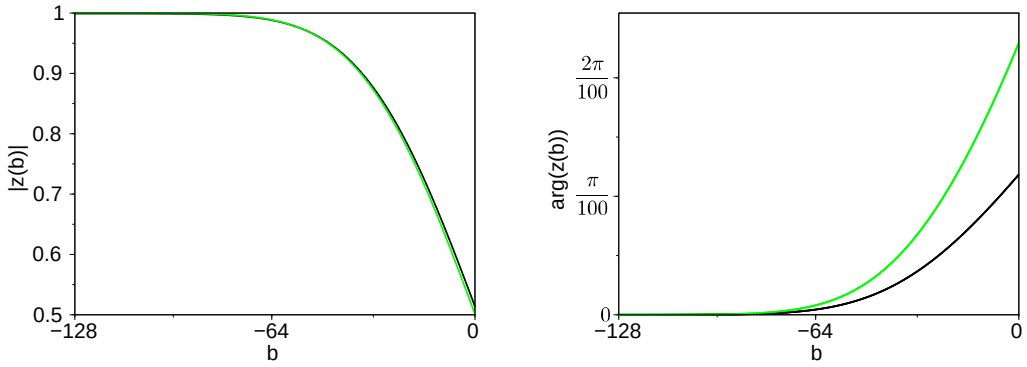


Figure 4.4: Left: $b \mapsto |z^*_\omega(b)|$ (black) and $b \mapsto |z_\omega(b)|$ (green). Right: $b \mapsto \arg(z^*_\omega(b))$ (black) and $b \mapsto \arg(z_\omega(b))$ (green).

appears that $1/z_\omega(b)$ should be an appropriate candidate corrective factor in the sense that

$$f(x) \approx 2\Re\left(\frac{W_f(a^*, x)}{z_\omega(x)}\right),$$

which is confirmed in Figure 4.5. It is also reassuring to observe that the dependency of $z_\omega(b)$ in $\omega$ only manifests through horizontal expansions or compressions of the case $\omega = 1$:

$$z_\omega(b) = z_1(\omega b).$$

### 4.2.3 Influence of the phase

The situation studied so far is the particular case $\varphi = 0$ of the more general one

$$f(x) = \cos(\omega x + \varphi).$$

It goes without saying that the equations established in the theoretical framework of section 4.1 can be adapted effortlessly. As a result, it comes that

$$W_f(a^*, b) = \frac{1}{2} e^{i(b\omega+\varphi)}$$

so that the relation

$$f(x) = 2|W_f(a^*, x)| \cos(\arg(W_f(a^*, x)))$$

still allows to recover $f$. The case involving border effects as above is slightly more challenging. If we consider

$$f(x) = \begin{cases} \cos(\omega x + \varphi) & \text{if } x \leq 0 \\ 0 & \text{if } x > 0 \end{cases}$$

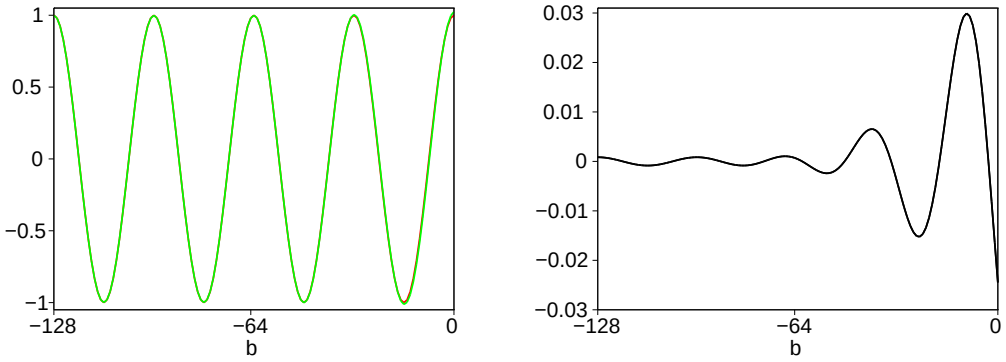


Figure 4.5: Left: The initial signal (red, masked by the green signal) and the reconstructed signal corrected with $1/z_\omega(b)$ (green). Right: the error in the reconstruction.

and if we mimic the procedure used previously, then equation (4.6) becomes

$$W_f(a^*, b) \approx \frac{1}{2} e^{i(b\omega+\varphi)} z_{\omega,\varphi}(b)$$

with

$$z_{\omega,\varphi}(b) = \frac{1}{2} + \frac{2ie^{-i\varphi}}{\pi} \int_0^1 \frac{\hat{\psi}(\Omega x)}{(x^2-1)(x-3)} \big(e^{-i\varphi}(1-x)\cos(b\omega(x-1)) \\ +i(\cos\varphi(x^2-2x-1) - 2i\sin\varphi)\sin(b\omega(x-1))\big)\, dx,$$

i.e.

$$\Re(z_{\omega,\varphi}(b)) = \frac{1}{2} + \frac{2}{\pi} \int_0^1 \frac{\hat{\psi}(\Omega x)}{(x^2-1)(x-3)} (\sin(2\varphi)(1-x)\cos(b\omega(x-1)) \\ +(2\sin^2\varphi - \cos^2\varphi(x^2-2x-1))\sin(b\omega(x-1))\big)\, dx$$

and

$$\Im(z_{\omega,\varphi}(b)) = \frac{2}{\pi} \int_0^1 \frac{\hat{\psi}(\Omega x)}{(x+1)(3-x)} (\cos(2\varphi)\cos(b\omega(x-1)) \\ +\sin\varphi\cos\varphi(1-x)\sin(b\omega(x-1)))\, dx.$$

It can be seen that these quantities are all numerically computable and that the intuitive relations

$$z_{\omega,\varphi}(b) = z_{1,\varphi}(\omega b)$$

and

$$z_{\omega,\varphi+\pi}(b) = z_{\omega,\varphi}(b)$$

hold for all $b, \omega, \varphi$, which indicates that we can assume that $\varphi \in [0, \pi)$. As in equation (4.4), we note $z^*_{\omega,\varphi}(b)$ the complex number such that

$$W_f(a^*, b) = \frac{1}{2} e^{i(b\omega+\varphi)} z^*_{\omega,\varphi}(b). \tag{4.9}$$

Similarly to Figure 4.4, it can be seen in Figure 4.6 that $z_{\omega,\varphi}(b)$ is close to the expected $z^*_{\omega,\varphi}(b)$ in modulus and in argument for all $\varphi \in [0, \pi)$. More precisely, it comes out from Figure 4.7 that

$$\sup_{\varphi\in[0,\pi)} \sup_{b\leq 0} \left\{ \left| 1 - \frac{|z_{\omega,\varphi}(b)|}{|z^*_{\omega,\varphi}(b)|} \right| \right\} < 0.025$$

and that

$$\sup_{\varphi\in[0,\pi)} \sup_{b\leq 0} \left\{ \left| \arg(z_{\omega,\varphi}(b)) - \arg(z^*_{\omega,\varphi}(b)) \right| \right\} < 0.044 < \frac{1.5\pi}{100}.$$

It can also be seen in Figure 4.7 that the skills of $1/z_{\omega,\varphi}(b)$ as corrective factor are of the same order as those already displayed in Figure 4.5 and that

$$\sup_{\varphi\in[0,\pi)} \sup_{b\leq 0} \left\{ \left| 2\Re\left( \frac{W_f(a^*, x)}{z_{\omega,\varphi}(x)} \right) - f(x) \right| \right\} < 0.04,$$

so that the corrected reconstructed signal is always extremely close to the initial one.

Finally, it is interesting to note that, while the interpretation of the decrease in amplitude of $z_{\omega,\varphi}(b)$ with $b$ is the same as in the case $\varphi = 0$, the instantaneous frequency is not necessarily increasing anymore. As a matter of example, for $\varphi = \pi/2$, the last data point is zero, thus the zero padding can be seen as a somehow natural extension of the signal in this case. As a consequence, the arguments of the wavelet coefficients have to "slow down" to better match with this feature, giving an instantaneous frequency lower than expected.

### A brief comparison with the symmetric padding

As mentioned in the introduction of this section, the symmetric padding is commonly used in practice. It consists in completing the signal at both borders with its own mirror. One of the reasons that justify this choice is the fact that it pads the signal while somehow keeping its properties, particularly the spectral content. Contrary to the zero padding, the additional values depend on the signal, which might be double-edged. On the one hand, in the case of $\cos(\omega x)$ defined for $x \leq 0$ (thus $\varphi = 0$), the symmetric padding is actually the perfect way to complete the signal (on the right hand side at least) and thus the CWT gives a flawless reconstruction of the initial signal. On the other hand, in the case of $\cos(\omega x + \pi/2)$, the symmetric padding is probably one of the worse possible choices and leads to major mistakes in the recovery of the signal. It can thus be sensed that this technique is heavily dependent on the phase $\varphi$ at stake. In order to support this claim, we compare the amplitudes and arguments of the extra factors that appear in the CWT with the zero padding and with the symmetric padding for various phases

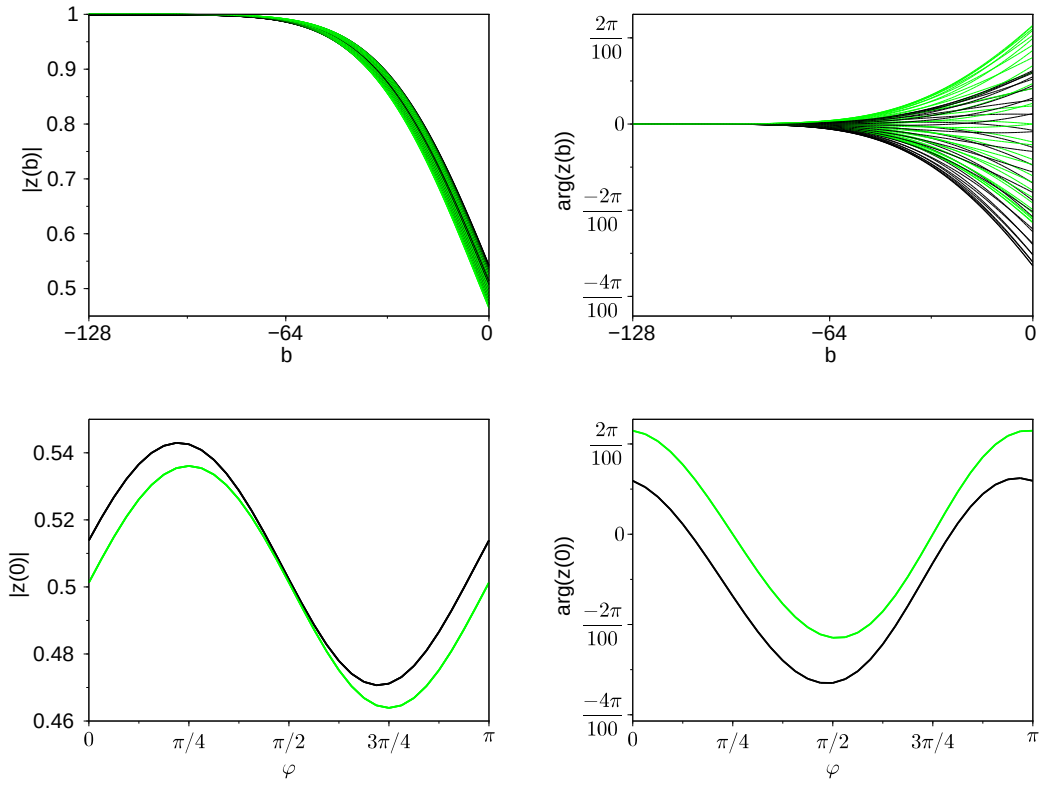


Figure 4.6: Top left: $b \mapsto |z^*_{\omega,\varphi}(b)|$ (black) and $b \mapsto |z_{\omega,\varphi}(b)|$ (green) for $\varphi$ ranging from 0 to $\pi$ (by steps of $\pi/32$). Top right: $b \mapsto \arg(z^*_{\omega,\varphi}(b))$ (black) and $b \mapsto \arg(z_{\omega,\varphi}(b))$ (green) for $\varphi$ ranging from 0 to $\pi$. Bottom left: $\varphi \mapsto |z^*_{\omega,\varphi}(0)|$ (black) and $\varphi \mapsto |z_{\omega,\varphi}(0)|$ (green). Bottom right: $\varphi \mapsto \arg(z^*_{\omega,\varphi}(0))$ (black) and $\varphi \mapsto \arg(z_{\omega,\varphi}(0))$ (green).

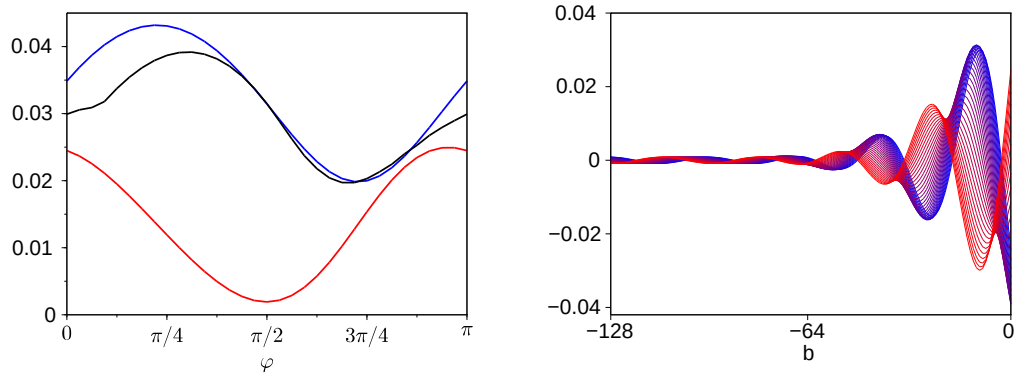


Figure 4.7: Left: maximum values of $\left|\arg(z_{\omega,\varphi}(b)) - \arg(z^*_{\omega,\varphi}(b))\right|$ (blue), $\left|1 - |z_{\omega,\varphi}(b)|/|z^*_{\omega,\varphi}(b)|\right|$ (red) and $|2\Re\left(W_f(a^*, b)/z_{\omega,\varphi}(b)\right) - f(b)|$ (black) for $b \leq 0$, as functions of $\varphi$. Note that it comes out that the blue and red curves are actually obtained exclusively from the case $b = 0$ in Figure 4.6. Right: error in the reconstructions, i.e. $f(x) - 2\Re\left(W_f(a^*, x)/z_{\omega,\varphi}(x)\right)$ as function of $x \leq 0$, for $\varphi$ ranging from 0 (blue) to $\pi$ (red) (by steps of $\pi/32$).

$\varphi$. In other words, we consider $f(x) = \cos(2\pi x/32 + \varphi)$ for $x \leq 0$ as previously, we still note $z^*_{\omega,\varphi}(b)$ the complex number such that equation (4.9) holds for $W_f(a^*, b)$ obtained with the zero padding, and we write $z^s_{\omega,\varphi}(b)$ the counterpart of $z^*_{\omega,\varphi}(b)$ in the case of the symmetric padding. The modulus and argument of $z^*_{\omega,\varphi}$ and $z^s_{\omega,\varphi}$ as functions of $b$ are displayed in Figure 4.8 for $\varphi$ ranging from 0 to $\pi$. This sole figure wholly illustrates a major advantage of the zero padding in a general context, in the sense that the wavelet coefficients are always affected by the border effects in the same way, while it is not the case with the symmetric padding where the influence of the phase can lead to drastically different performances. As a consequence, the symmetric padding should be preferred only in safe and controlled cases, e.g. when the practitioner knows that it is the best option and only wants to illustrate new signal processing techniques on toy examples; this common custom will be used in chapter 6.

### A brief comparison with the constant padding

The last type of padding that we examine is the constant padding, i.e. the last value of the signal is repeated as many times as necessary after the end of the signal (and similarly for the first value for the constant padding on the left-hand side). This technique is also sometimes used in practice because, unlike the zero padding, it never creates a discontinuity at the end of the signal, and unlike the symmetric padding, it does not create a cusp-like singularity either. However, the spectral content of the signal is not preserved and, more importantly, the padded values give a signal which cannot be approximated in terms of oscillatory components (unless the last value is zero, which gives

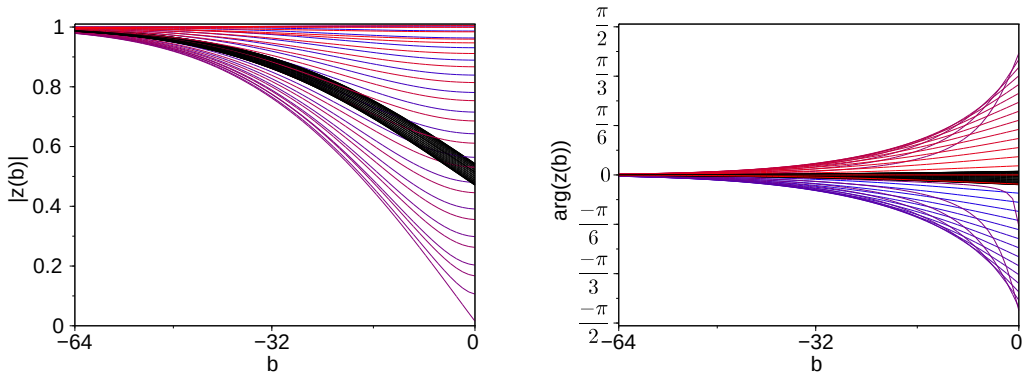


Figure 4.8: Left: $b \mapsto |z^*_{\omega,\varphi}(b)|$ (i.e. zero padding, black) for $\varphi$ ranging from 0 to $\pi$ (by steps of $\pi/32$) and $b \mapsto |z^s_{\omega,\varphi}(b)|$ (i.e. symmetric padding) for $\varphi$ ranging from 0 (blue) to $\pi$ (red). Right: $b \mapsto \arg(z^*_{\omega,\varphi}(b))$ (black) and $b \mapsto \arg(z^s_{\omega,\varphi}(b))$, with the same color code.

back the zero padding). This means that, for a cosine of period $p$, the average of the padded values on an interval of length $p$ is not zero, which is the case in the two previous methods. Intuitively, since the first padded values are close to the last available ones and somehow close to the expected ones, the instantaneous frequency should decrease at the borders so as to replicate this "good" feature as long as possible. Similarly to the zero padding, the amplitudes are likely to decrease since, at some point, the padded values will be far from the natural behavior of the signal. Moreover, in the same context as above, the influence of the phase $\varphi$ should be noticed since, in the case $\varphi = 0$, after half a period the padded values stay at 1 while the signal should be around -1, which is quite a significant difference. On the other hand, the case $\varphi = \pi/2$ (thus the zero padding) will never be that far from the expected values. In the same spirit as in the previous section, these claims are confirmed in Figure 4.9, where $z^c_{\omega,\varphi}(b)$ is the counterpart of $z^*_{\omega,\varphi}(b)$ in the case of the constant padding. It can be seen that the decrease in amplitude is of the same order as in the zero padding, while the instantaneous frequency is always decreasing and this reduction is worse than with the zero padding. The influence of the phase is especially noted in the second plot and raises the following important remark. As mentioned, the zero padding has a "universal" connotation. In some way, the symmetric padding has also this characteristic in the sense that, if the signal is made up of several cosines, the symmetrization will be applied for all of them, with the consequences exposed in the previous section for each of the components. However, in the case of the constant padding, the last value of the signal is generally not the last value of any of the components, which makes the padding less appropriate and may lead to immoderate abnormalities.

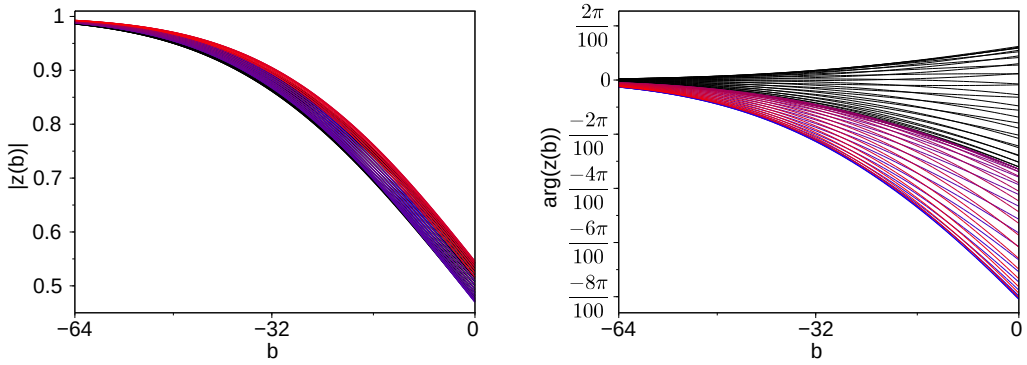


Figure 4.9: Left: $b \mapsto |z^*_{\omega,\varphi}(b)|$ (i.e. zero padding, black) for $\varphi$ ranging from 0 to $\pi$ (by steps of $\pi/32$) and $b \mapsto |z^c_{\omega,\varphi}(b)|$ (i.e. constant padding) for $\varphi$ ranging from 0 (blue) to $\pi$ (red). Note that the blue and red curves mask the black ones; they are always close to each other. Right: $b \mapsto \arg(z^*_{\omega,\varphi}(b))$ (black) and $b \mapsto \arg(z^c_{\omega,\varphi}(b))$, with the same color code.

## 4.3 Countering border effects through iterations

Originally, we initiated the study of the border effects as presented in section 4.2 in an attempt to correct the wavelet coefficients computed at the end of the signal so that they can be extrapolated to make predictions of the ENSO climate index (see chapter 5). While this technique worked reasonably well with corrections inspired by the zero padding with simple stationary harmonic components as in the previous section, the practical case of amplitude modulated-frequency modulated (AM-FM) signals turned out extremely difficult to handle. Not only were the corrected amplitudes sometimes far from the expected values, but also the arguments began to play a non-negligible role in the process. This called for the development of another method to counteract the border effects and improve the reconstruction of the signal at the edges.

It is reasonable to believe that the zero padding should be a suitable asset in this framework (see section 4.2). However, even if Figure 4.8 suggests that it might be possible to find some kind of "universal average" corrective factor with the zero padding, it appears that the exact knowledge of the phase is crucial. Indeed, a corrective factor computed for a phase $\varphi_1$ applied on a cosine with another phase $\varphi_2$ sometimes generates considerable mistakes. In consequence, we are naturally led to develop a safer yet less accurate procedure, which does not involve potentially dangerous treatments of the components. Even if the technique proposed in this section still does not allow a correction of border effects leading to satisfying extrapolations and forecasts, it does always improve the reconstruction of the initial signal through the components extracted from its CWT.

The method is based on the following simple idea. When it comes to extracting

components from a signal $s$ as accurately as possible, the CWT with the zero padding can be used several times to sharpen the desired modes and improve the reconstruction of $s$ progressively. More precisely, if the components of interest are located at the scales $(a_i)_{i\in I}$ (for some set of indices $I$), then at the first iteration we can extract $c_i^1$ for each $i \in I$ as

$$c_i^1(x) = 2\Re(W_s(a_i, x)).$$

With the use of the zero padding, we know from section 4.2 (see e.g. Figure 4.2 and Figure 4.3) that there is still some energy to siphon off the signal at the borders at the scales $(a_i)_{i\in I}$. For this reason, we repeat the process, i.e. the CWT and extraction at the same scales $(a_i)_{i\in I}$ but with

$$s_1 = s - \sum_{i\in I} c_i^1$$

instead of $s$ to get the modes $(c_i^2)_{i\in I}$. The iterative procedure thus consists in the successive extractions of

$$c_i^n(x) = 2\Re(W_{s_{n-1}}(a_i, x))$$

for $n \in \mathbb{N}$ and $i \in I$, where

$$s_n = s_{n-1} - \sum_{i\in I} c_i^n$$

with $s_0 = s$. By construction, the successive sums $(\sum_{i\in I} c_i^n)_{n\in\mathbb{N}}$ carry less and less information as $n$ increases. We thus stop the process when the components extracted are not significant anymore: we chose to finish after the $N^{\text{th}}$ iteration if

$$T(N) = \sup_x \left| \sum_{i\in I} c_i^N(x) \right| < \alpha \sup_x \left| \sum_{i\in I} c_i^1(x) \right| = \alpha T(1),$$

where $\alpha$ is a threshold regulating $N$ and which will usually be set as 0.001. The final components of interest $(c_i)_{i\in I}$ at the scales $(a_i)_{i\in I}$ are then obtained as

$$c_i = \sum_{n=1}^{N} c_i^n.$$

Table 4.1 shows how the number of iterations $N$ varies with $\alpha$ for $f(x) = \cos(2\pi x/32)$ defined on $[-255, 0]$ as in section 4.2.1, where $I$ is naturally reduced to the scale corresponding to the period 32. It also displays the evolution of $T(N)$ (note $T(1) = 1$ in this case), the PCC, the root mean square error (RMSE), and the maximal absolute error (MxAE) in the reconstruction, i.e.

$$\text{MxAE} = \sup_x \left| f(x) - \sum_{i\in I} c_i(x) \right|.$$

The reconstructed signal and the errors for $\alpha = 0.1,\ 0.01,\ 0.001,\ 0.0001$, thus corresponding to $N = 3,\ 10,\ 42$ and 185 iterations, are plotted in Figure 4.10. Compared

Table 4.1: Number of iterations $N$, $T(N)$, PCC, RMSE and MxAE as functions of $\alpha$.

| $\alpha$ | N | T(N) | PCC | RMSE | MxAE |
|---|---|---|---|---|---|
| .1 | 3 | .0632 | .99708 | .05437 | .296 |
| .05 | 4 | .0393 | .99794 | .04558 | .257 |
| .01 | 10 | .00915 | .99929 | .02664 | .162 |
| .005 | 15 | .00489 | .99956 | .02108 | .131 |
| .001 | 42 | .000987 | .99986 | .01190 | .0761 |
| .0005 | 67 | .000499 | .99992 | .00911 | .0588 |
| .0001 | 185 | .0000993 | .99997 | .00531 | .0335 |

to the initial case $N = 1$ displayed in Figure 4.3, it can be seen that only 10 iterations already greatly improve the reconstruction. It can also be seen that the error in the reconstruction can be made arbitrarily small.

**Remark 4.3.1.** The threshold $\alpha$ depends on the purpose of the study. Nevertheless, in all cases, we recommend to perform at least a few iterations not only to improve the reconstruction at the borders but also to sharpen the components extracted from the signal. It is also important to keep in mind that, in practice, this technique does not generally provide a full correction of the border effects. Besides, if one tries to combine the iterations and a "universal average" corrective factor with the zero padding, the results obtained after a few iterations are extremely close to those exposed in this section. For these reasons, the study of the border effects and the ways to counteract them may be useful in the case of components that display a stationary behavior, with only little variations in amplitudes and frequencies. It may also be of some help in works where the wavelet coefficients at the borders do not play a primary role. In the opposite case, such as in the context of time series forecasting, it is strongly advised to avoid the use of the wavelet coefficients at the borders, with or without corrections or iterations. It is then recommended to use different techniques, possibly based on the information that the CWT brings on the general behavior of the components extracted, as in chapter 5.

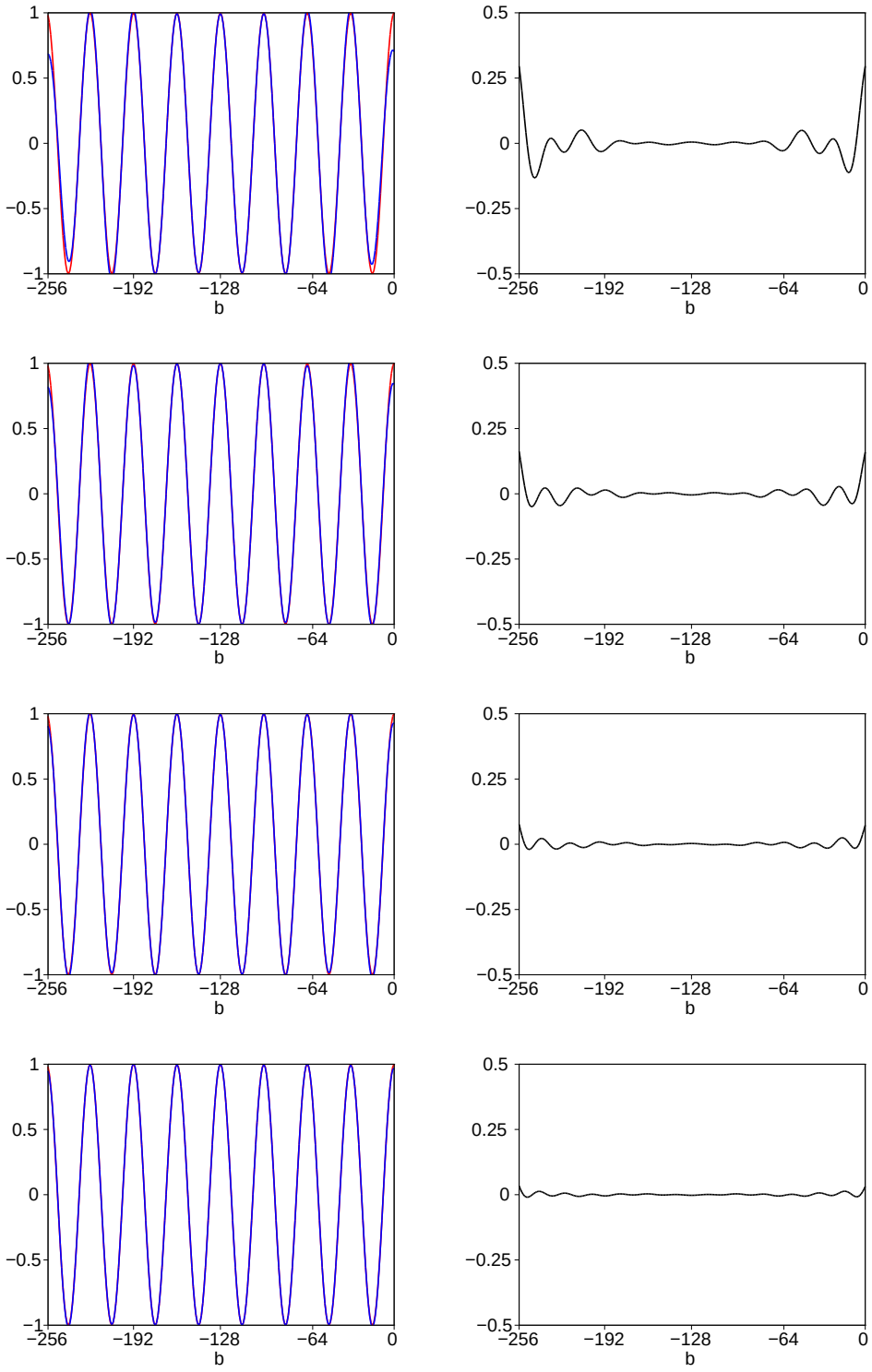


Figure 4.10: Left: The initial signal (red) and the reconstructed one (blue) for 3, 10, 42, 185 iterations. Right: The corresponding errors.

# Chapter 5

# Analysis and forecasting of the Oceanic Niño Index

In this chapter, we investigate the predictability of the El Niño Southern Oscillation (ENSO) index through information obtained with its CWT. Initially, the idea was to develop a wavelet-based algorithm designed to produce forecasts of a given time series by smooth extrapolations of the modulus and arguments of the components extracted with the CWT. We realized that, in the ideal (and artificial) case where border effects were completely annihilated, this simple predicting scheme was able to produce excellent forecasts. Of course, this was not so surprising since a perfect correction of border effects was only possible when the future values of the time series were already known and used. Nonetheless, for the ENSO index, we noticed that the arguments of the components somehow played a more important role than their amplitudes. We thus believed that, in the real case where border effects were present and the future values unknown, the zero padding and the results exposed in chapter 4 would allow us to provide corrections sufficiently accurate so that we could come close enough to the ideal context and provide acceptable extrapolations and forecasts. However, no matter how hard we tried, we found it utterly difficult to implement these ideas in a satisfying way in practice, as mentioned in section 4.3. Therefore, we changed our approach and decided to draw on the information provided by the CWT of the available data (thus mostly unaltered by border effects) to elaborate a forecasting model for the specific ENSO time series. Most of the results presented here have been published in [43].

## 5.1 Introduction

El Niño Southern Oscillation (ENSO) is an irregular climate oscillation induced by sea surface temperature anomalies (SSTA) in the Equatorial Pacific Ocean. An anomalous warming in this area is known as El Niño (EN), while an anomalous cooling bears the name of La Niña (LN). ENSO is well recognized as the dominant mode of interannual variability in the Pacific Ocean and it affects the atmospheric general circulation which transmits the ENSO signal to other parts of world; these remote effects are called teleconnections. Variations in the SSTA between warm and cold episodes induce changes in the occurrence of severe weather events, which dramatically affect human activities and ecosystems worldwide (see e.g.[62, 69]). Therefore, ENSO predictions are of first importance in order to help governments and industries to plan actions before the occurrence of these phenomena.

Over the last two decades, many models have been proposed for forecasting ENSO[1] by focusing on sea surface temperatures in the so-called Niño 3.4 region (5°N-5°S, 170°W-120°W, see e.g. [99, 140, 154, 155] and Figure 5.1). Other variables such as sea level pressure and wind stress data are also used in many dynamical and statistical models (see e.g. [20, 82]). At the Climate Prediction Center (CPC), the official ENSO indicator is the Oceanic Niño Index (ONI), which is a 3 month running SSTA signal with respect to 30 years periods in this Niño 3.4 area and is the principal measure for monitoring, assessing, and predicting ENSO (see Figure 5.1). The EN (resp. LN) events are defined by the CPC as 0.5°C positive (resp. negative) anomalies (called warm (resp. cold) episodes in the following) during at least 5 consecutive overlapping months of ONI. As it can be found in the literature, current predictions of ENSO based on dynamical or statistical models are most often limited to twelve months (e.g.[20, 99, 140, 154, 155]) and have mixed success rates ([20]). While it has been argued that accurate ENSO forecasts at longer lead times are out of reach ([51, 139]), some works provide evidence that long-term predictions are actually achievable ([29, 79, 117]).

The present chapter fits into the category of long-term predictions. Indeed, we use the CWT introduced in chapter 4 to analyze and forecast the ONI signal for lead times ranging from a few months to three years. First, the application of the CWT to ONI is developed in section 5.2. The components extracted for reconstructing the signal of interest carry valuable information which is then exploited to derive a simple predictive scheme for ONI, explained in section 5.3. The prediction skills of the proposed model are then assessed and discussed in section 5.4. Finally, we draw some conclusions and envisage possible future works in section 5.5. Let us underline that the proposed approach is independent of any geophysical principles but is based only on the quasi-periodicity of the ENSO signal; the reader interested in physical considerations should consult [117] and the references therein. The philosophy of this chapter is to provide a glimpse of the practicability of long-term predictions of ONI and to pave the way for further investigation in this direction.

[1] `http://iri.columbia.edu/our-expertise/climate/forecasts/enso/current/`

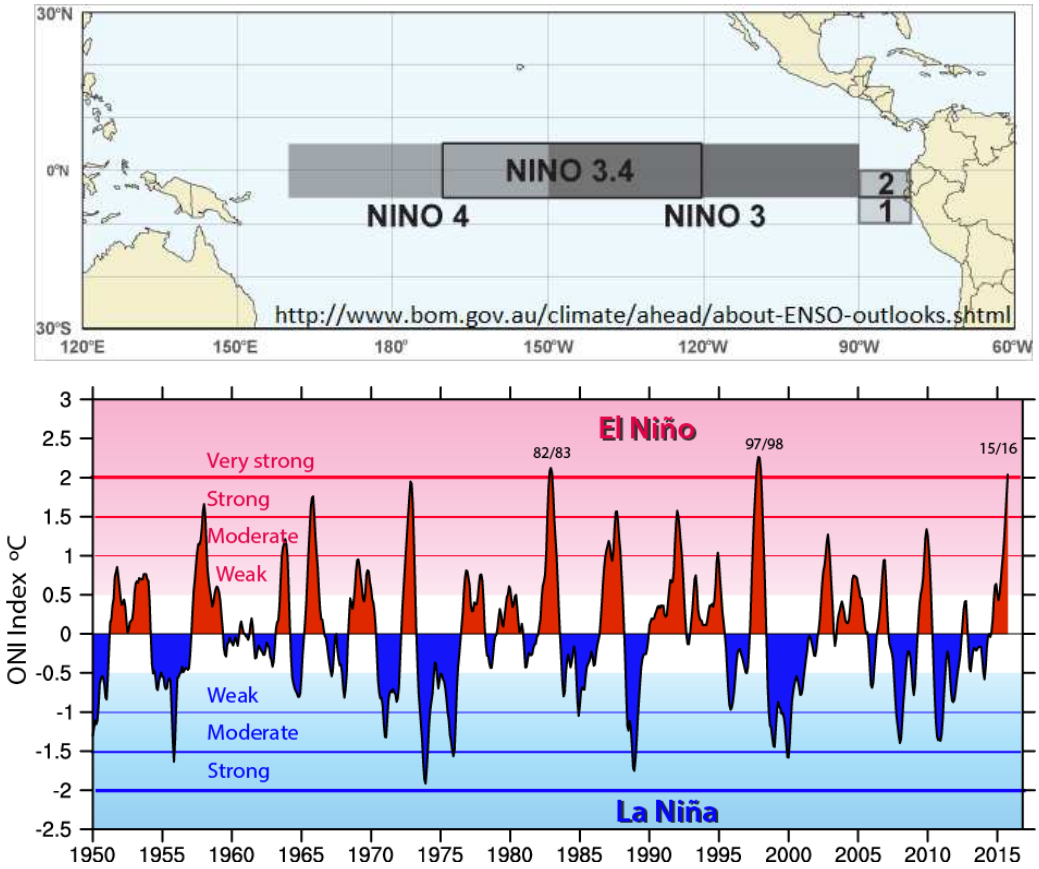


Figure 5.1: Top: Localization of the Niño 3.4 region in the Pacific Ocean. Bottom: ONI index from 1950 and illustration of the strength of El Niño and La Niña events. Retrieved from [143].

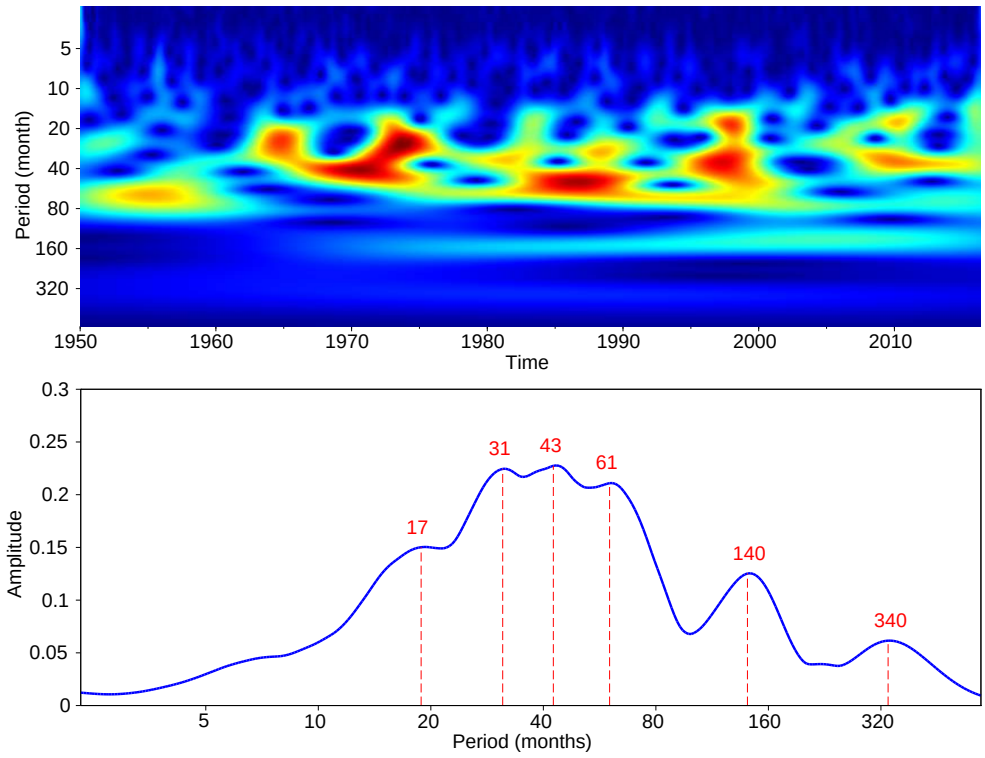


Figure 5.2: Top: Modulus of the CWT of ONI. The values range from 0 (blue) to 0.45 (red). Bottom: Wavelet spectrum of ONI. The main periods governing the signal can be easily identified and correspond to near-annual to decadal modes of variability.

## 5.2 Wavelet Analysis

This section is devoted to a wavelet analysis of ONI, which brings valuable information for modeling and predicting long-term trends of the signal. The principles involved are inspired from [41, 104, 105] as well as section 4.3 of chapter 4. The ONI signal used consists of the usual 3-months running means of monthly SSTA; it can be found at [26] and the last data point considered is the season March-April-May 2016.

The CWT is applied to ONI with the same wavelet $\psi$ defined by equation (4.2) as in chapter 4 and its modulus (i.e. its TF-representation) is represented in Figure 5.2. It can be observed that the energy of the signal is concentrated in periods between $\approx 20$ and $\approx 80$ months. The signal displays the characteristics of an AM-FM signal; we will thus need to capture time-varying amplitudes and periods. In order to determine at which periods we will extract components, the wavelet spectrum (WS) is computed:

$$a \mapsto \Lambda(a) = E_t \left| W_f(a,t) \right| \tag{5.1}$$

where $E_t$ denotes the mean over time (see Figure 5.2). It can be observed that $\Lambda$

displays a significant amount of energy at periods of $\approx 17, 31, 43, 61, 140$ and 340 months, which is globally consistent with previous studies (see [117] and references therein). The associated components are extracted from the CWT using the iterating scheme explained in section 4.3. They are named $c_{17}, ..., c_{340}$ and are plotted in Figure 5.3 along with the high-frequency seasonal and annual modes $c_6$ and $c_{12}$. We can note that, as desired, the CWT allows a "flexible" representation of the signal, i.e. these components are AM-FM signals. The components $c_{17}, c_{31}, c_{43}, c_{61}$ are near-annual, quasi-biannual and two quasi-quadriennal modes of variability of ENSO and are largely discussed in [117] whereas $c_{140}$ and $c_{340}$ are likely linked with the tropical decadal and interdecadal Pacific variability (see e.g. [110]). Let us also mention that, while we were investigating if these components could be related to the variations of solar activity through the monthly sunspot number signal, we found out a few particularities which are briefly exposed in appendix 5.A.

The contribution of a given component $c$ in the signal can be assessed through several indicators. First, the relative energy of $c$ with respect to ONI (denoted $s$) is computed as

$$\epsilon_{rel} = \frac{\|c\|}{\|s\|},$$

where $\|.\|$ denotes the energy of a signal from the signal analysis point of view, i.e. as the square of the $L^2$ norm (sum of the squares of the data points). In order to ensure that $c$ contains pertinent information, we also compute the relative accretion of energy that can be attributed to $c$ as

$$\lambda_{rel} = \frac{\|s\| - \|s - c\|}{\|s\|}.$$

Finally, we compute the PCC between $c$ and $s$. These indicators can be found in Table 5.1 and confirm that $c_{17}$, $c_{31}$, $c_{43}$, $c_{61}$ and $c_{140}$ contain most of the information about the variability of ONI. We also calculated these indicators for the reconstructed signal $srec_8$ (sum of the 8 components extracted) and for $srec_4 = c_{31} + c_{43} + c_{61} + c_{140}$. The first ones indicate that the reconstruction is almost perfect; we can add that the root mean square error (RMSE) is 0.04. Those related to $srec_4$ show that the low-frequency components capture a significant part of the variability of ONI (with RMSE= 0.349). This observation is actually the one suggesting that long-term forecasts of ONI should be achievable.

The CWT brings other valuable information that turn out useful for conceiving a model for long-lead forecasts of ONI. Indeed, if we look at Figure 5.3, it appears that $c_{31}, c_{43}, c_{61}$ and $c_{140}$ regulating the long-term variations of ONI are relatively stationary and should thus be easily modeled. Regrettably, since the high-frequency components $c_6, c_{12}$ and $c_{17}$ are quite volatile and unpredictable and as the nature of $c_{340}$ is uncertain, these will not be taken into account. Neglecting the high-frequency components can be seen as a "lesser of two evils" choice. On the one hand, trying to model and use them for long-term forecasting is overly hard; our attempts resulted in predictions that were globally worse than without using them because of their variability. On the other hand, omitting them inevitably leads to a loss of accuracy in the timing and intensity of EN

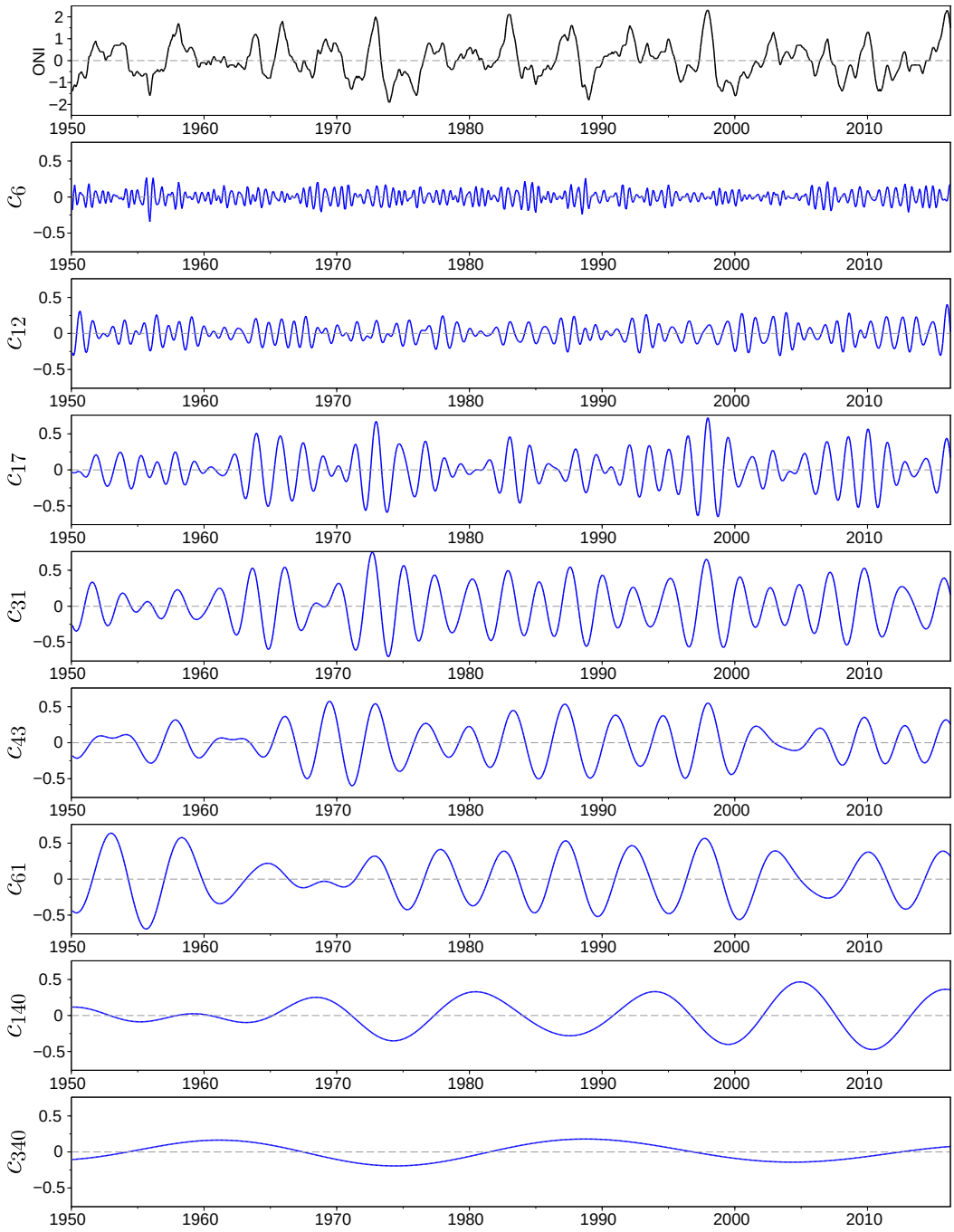


Figure 5.3: ONI signal and the components extracted with the CWT.

Table 5.1: Relative energy, relative accretion of energy and correlation associated with the components with respect to ONI. These indicators are also given for $srec_8$ which stands for the reconstructed signal as the sum of the 8 components and $srec_4$ defined as the sum of $c_{31}, c_{43}, c_{61}, c_{140}$.

| Signal | $\epsilon_{rel}$ | $\lambda_{rel}$ | PCC |
|---|---|---|---|
| $c_6$ | .013 | .017 | .131 |
| $c_{12}$ | .026 | .073 | .306 |
| $c_{17}$ | .095 | .190 | .462 |
| $c_{31}$ | .147 | .326 | .617 |
| $c_{43}$ | .108 | .321 | .653 |
| $c_{61}$ | .159 | .284 | .555 |
| $c_{140}$ | .086 | .101 | .319 |
| $c_{340}$ | .021 | .028 | .168 |
| $srec_8$ | .996 | .997 | .999 |
| $srec_4$ | .731 | .801 | .896 |

and LN events. Besides leaving room for improvements, this second option turned out to be the most appropriate in the context of long-term forecasting of ONI. In consequence, we are led to build initial guesses on future values of the signal based on oscillating components with periods of $31, 43, 61$ and $140$ months. Their amplitude will be estimated through the wavelet spectrum and considered constant throughout the signal, whereas their phases will be evaluated for each prediction. When the first guess is made, the CWT will be applied to recover amplitude and frequency modulations and to provide a forecast in a natural way. This is detailed in the next section.

## 5.3 Forecasting method

In the present study, we focus on forecasting the last two decades of ONI, i.e. from January 1995 to April 2016. Data prior to 1995 is used as training set to calibrate the method. As mentioned, the idea is to construct components $y_i$ ($i \in I = \{31, 43, 61, 140\}$) of the form

$$y_i(t) = A_i \cos\left(2\pi t/i + \phi_i(t)\right)$$

that can then be extrapolated effortlessly. The amplitudes $(A_i)_{i\in I}$ can be estimated easily with data until 1995. The calculation of the phases $(\phi_i)_{i\in I}$ is more challenging and needs to be done as accurately as possible to have efficient forecasts. The main ideas of the algorithm proposed for the whole procedure are described below and appendix 5.B shows a more detailed prototype of the code used to construct $y_{43}$. In the following, the values of the initial discrete ONI signal are noted $s(t)$ for $t = 1, ..., T$, where $s(T)$ is the last data available for the considered forecast.

1. First, we model the decadal oscillation. The amplitude $A_{140}$ is estimated with the WS of $s$ (always until 1995 for the amplitudes) as 0.35 and we set
$$y_{140}(t) = A_{140}\cos(2\pi t/140 + 2.02)$$
so that it is phased with the solar maximum and $c_{140}$ in the 70's.

2. We now work with $s_1 = s - y_{140}$. The WS of $s_1$ gives $A_{61} = 0.435$. The idea is to phase $y_{61}$ with the strongest warm events of $s_1$, which occur approximately every 5 years, and anti-phase $y_{61}$ with the weaker warm events occurring in between. More precisely, for each time $t \leq T$, we find the position $p$ of the last local maximum of $s_1$ such that $s_1(p) > 0.5$. If $s_1(p) > 0.9$ then we set
$$y_{61}(t) = A_{61}\cos(2\pi(t-p)/61);$$
else
$$y_{61}(t) = -A_{61}\cos(2\pi(t-p)/61).$$

3. We now work with $s_2 = s_1 - y_{61}$. The WS of $s_2$ gives $A_{31} = 0.42$. Now, the idea is to phase $y_{31}$ with the cold events of $s_2$, which occur approximately every 2.5 years. More precisely, for each time $t \leq T$, we find the position $p$ of the last local minimum of $s_2$ such that $s_2(p) < -0.5$ and we set
$$y_{31}(t) = -A_{31}\cos(2\pi(t-p)/31).$$

4. We now work with $s_3 = s_2 - y_{31}$. The WS of $s_3$ gives $A_{43} = 0.485$. We set that $y_{43}$ has to explain the remaining warm and cold events of $s_3$ and we proceed as follows. For each time $t \leq T$, we find the position $p$ of the last local maximum of $s_3$ such that $s_3(p) > 0.5$ and we set
$$y^1_{43}(t) = A_{43}\cos(2\pi(t-p)/43).$$
Then we find the position $p$ of the last local minimum of $s_3$ such that $s_3(p) < -0.8$ and we set
$$y^2_{43}(t) = -A_{43}\cos(2\pi(t-p)/43).$$
Finally, we define
$$y_{43} = (y^1_{43} + y^2_{43})/2.$$

5. We extend the signals $(y_i)_{i\in I}$ up to $T+N$ for $N$ large enough (at least the number of data to be predicted). Then
$$y = \sum_{i\in I} y_i$$
stands for a first reconstruction (for $t \leq T$) and forecast (for $t > T$) of $s$.

6. We set $s(t) = y(t)$ for $t > T$, perform the CWT of $s$ and extract the components $\hat{c}_j$ at scales $j$ corresponding to 6, 12, 17, 31, 43, 61 and 140 months. These are considered as our final AM-FM components and $\hat{c} = \sum_j \hat{c}_j$ both reconstructs (for $t \leq T$) and forecasts (for $t > T$) the initial ONI signal in a smooth and natural way.

## 5.4 Predictive skills

The predictive skills of the proposed model for the period 1995-2016 are tested in two ways. First, we show that El Niño and La Niña events that occurred during this period could have been anticipated years in advance. Then, we show that the PCC and RMSE of the retrospective forecasts as functions of the lead time are encouraging regarding long-term forecasts.

The predictions of EN and LN events 6, 12, 18, 24, 30 and 36 before the peak of the episode are displayed in Figure 5.4 and Figure 5.5. It can clearly be seen that the trend of the ONI curve can be predicted in advance and thus major EN and LN events can be forecasted long before they happen. One of the most interesting results is about the famous strong event of 1997/98, which is foreseen up to 3 years in advance with a lag of only 3 months. A similar observation can be made regarding the 2009/10 EN for which El Niño conditions are anticipated 2 to 3 years in advance with a lag of 3 to 6 months. Our model also suggests that the recent strong EN event of 2015/16 might have been forecasted at least 18 months in advance and even classified as "strong EN" in mid 2014. However, it can be seen that the intensity of the most extreme EN events, e.g. 1997/98 and 2015/16, is underestimated. Nevertheless, since the occurrence of strong EN events seems to depend mainly on the local maxima of $c_{61}$, predicting that this component is about to reach a peak could be sufficient to warn of an upcoming strong event. Comparable observations can be made regarding the predictions of LN events, though the lags are generally delays of 3-6 months in this case. It is important to recall that seasonality is not taken into account, which contributes to explain the delays and the underestimation of the intensities to some extent. The fact that we use constant amplitudes in the model plays a role as well since the real ONI components are actually AM-FM. This calls for further investigation in the modulations of the amplitudes and their potential phase-locking with their associated component. Even though there is an exciting challenge in trying to incorporate high-frequency components in the model and to modulate the amplitudes, the long-term trends are recovered and our predictions are satisfying, especially given the long-lead times considered and the simplicity of the model.

In a more "global" approach, we can now focus on the prediction skills of our model as functions of the lead time. For that purpose, the retrospective forecasts at 6, 12, 18, 24, 30 and 36 months lead times are plotted in Figure 5.6. As a matter of information, they are computed and displayed from 1975 to show that the model also explains ONI variability prior to 1995 if the values of the amplitudes got in section 5.3 had been obtained in the mid-70's (the rest of the algorithm does not depend on the training data). As already observed, most EN and LN events can be foreseen from 1 to 3 years in advance. The overall trend of the curve is almost always in agreement with observations, confirming that long-term predictions are possible. Using data until April 2016, we issued a forecast of ONI (plotted in Figure 5.6), which predicts a relatively strong LN event during 2017.

Finally, the prediction skills of the model are measured with the RMSE and PCC

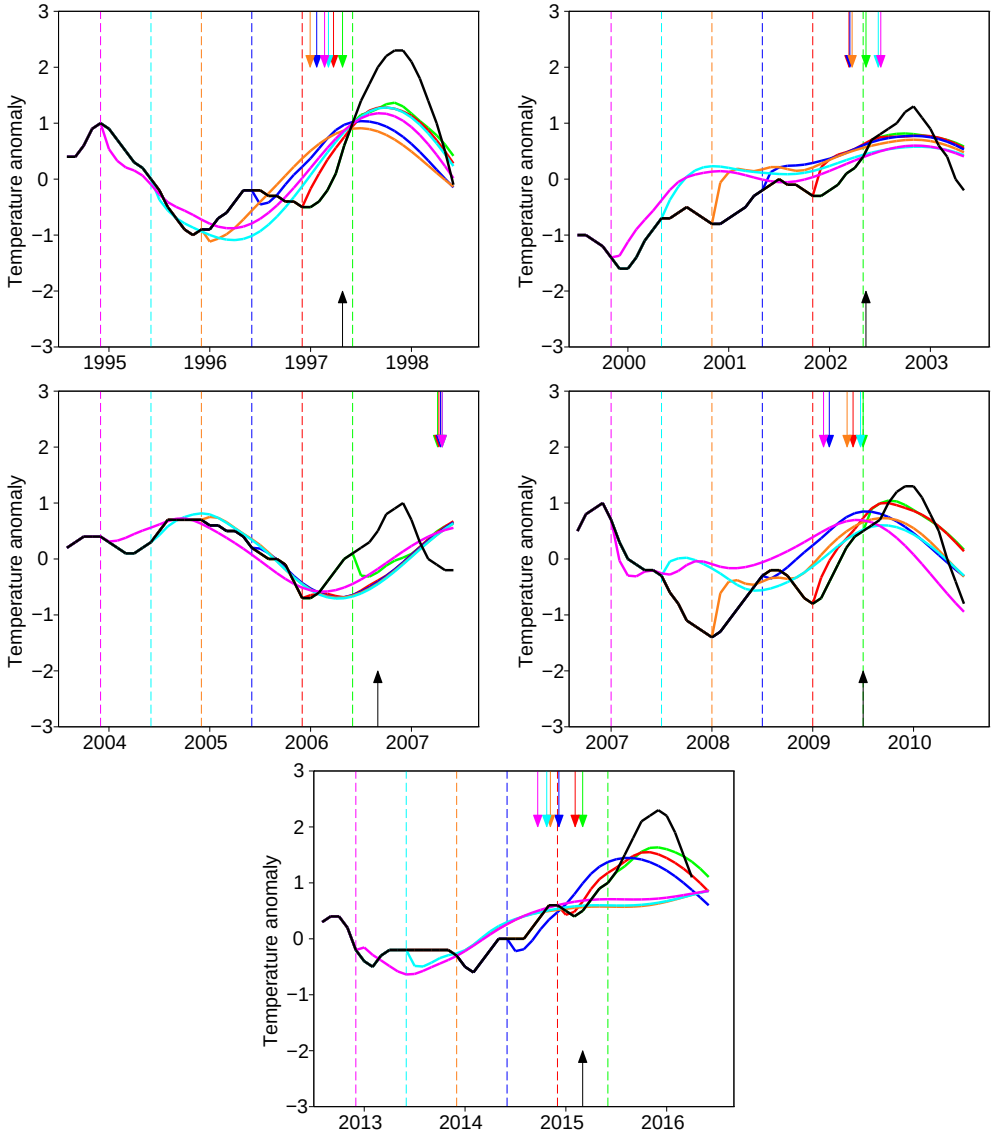


Figure 5.4: Forecasts of El Niño events 6 (green), 12 (red), 18 (blue), 24 (orange), 30 (cyan), 36 (magenta) months before the peak of the event. The black curve is the ONI signal. The arrows indicate the moment at which the El Niño condition (SSTA $> 0.5$°C) is reached.

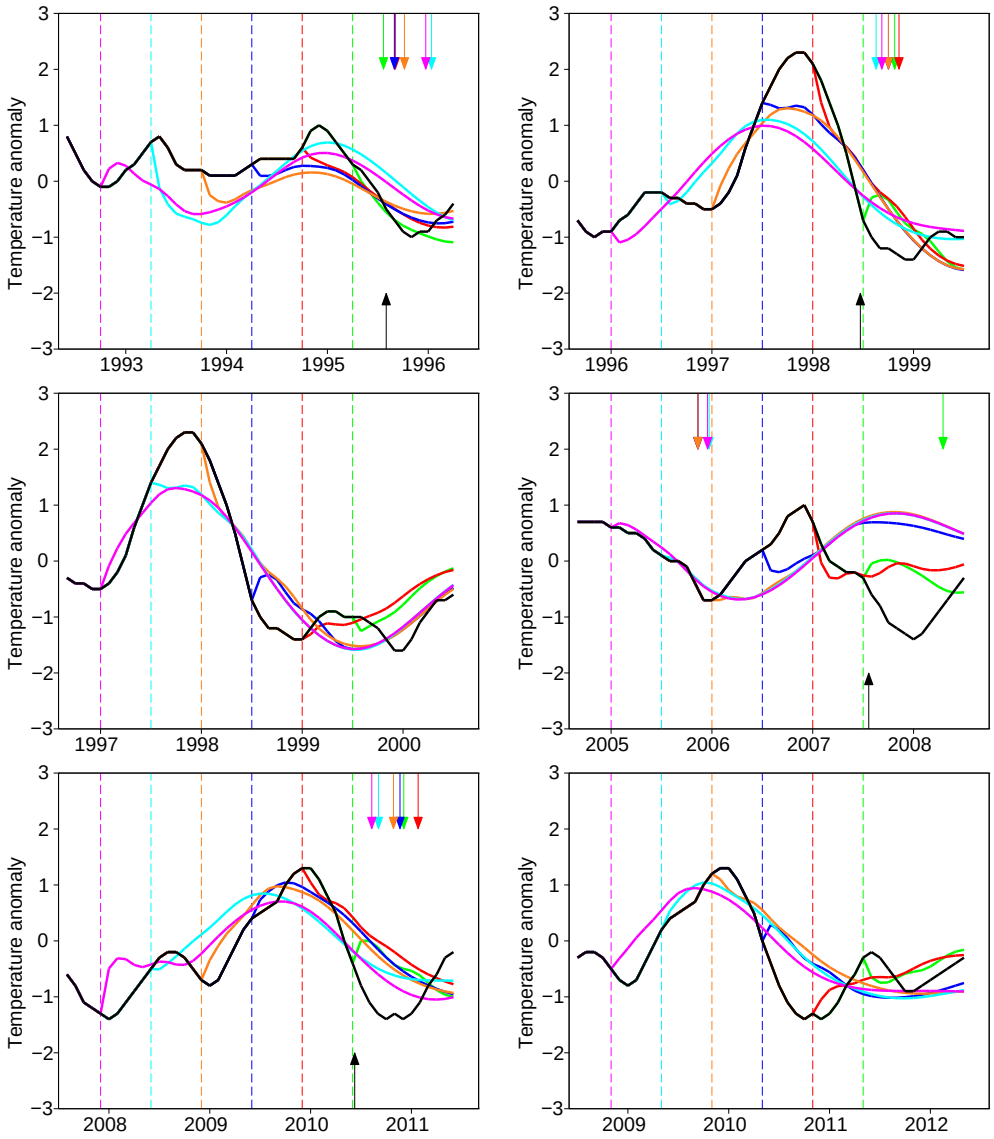


Figure 5.5: Forecasts of La Niña events 6 (green), 12 (red), 18 (blue), 24 (orange), 30 (cyan), 36 (magenta) months before the peak of the event. The black curve is the ONI signal. The arrows indicate the moment at which the La Niña condition (SSTA $< -0.5$°C) is reached. Note that the LN event of 2000 is a remnant of the one that occurred in 1999; SSTA do not even reach 0°C in between. The same observation holds for LN events of 2011 and 2012. Therefore, it does not make any sense to draw the arrows as in the other panels.

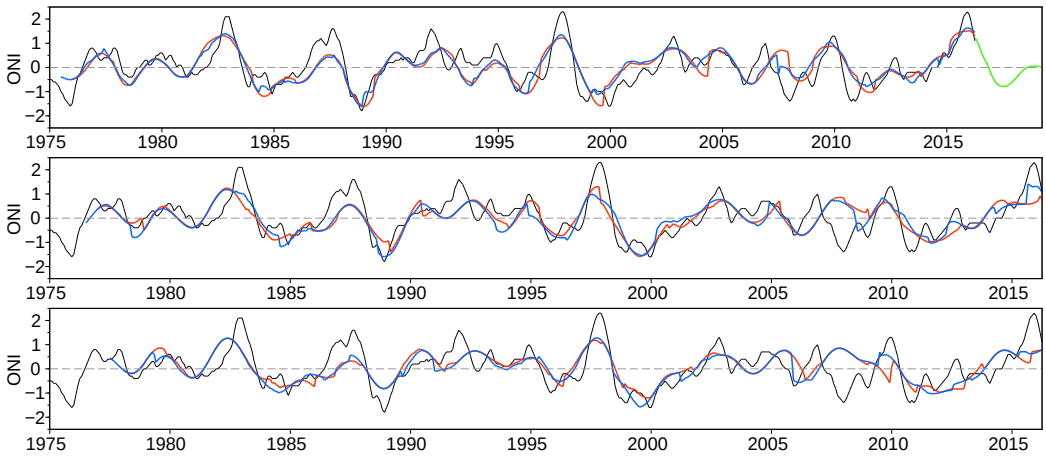


Figure 5.6: Retrospective forecasts of ONI at 6 (blue) and 12 (red) (then 18 and 24, 30 and 36) months lead time. On the first panel, the green curve is our forecast of ONI (issued in April 2016).

between the forecasted values and the initial signal as functions of the lead time; these indicators are plotted in Figure 5.7. An indicative comparison with the skills of the models from [20] and [117] is discussed in appendix 5.C. It appears that the skills of our model remain relatively stable and decrease slowly rather than abruptly compared to some other methods (see Figure 5.9 and Figure 5.10 in appendix 5.C). Although the performances are acceptable but not remarkable at short lead times in comparison with [20, 117], the most interesting fact is that they are excellent at long lead times ($> 12$ months). This is because it is designed to capture and predict the long-term variability of the signal. Let us also note that, since ONI has almost zero mean ($= 0.03$), its standard deviation ($= 0.84$) can be viewed as the RMSE-skill of a model for which all the predictions are set to zero. As seen in Figure 5.7, our model remains below this threshold while Figure 5.10 suggests that it would not necessarily be the case for other models. Consequently, it is necessary to underline that the proposed model should be used in complement with other methods because it brings helpful benefits regarding the long-term predictability of ONI.

## 5.5 Conclusion

We carried out a wavelet analysis of the Oceanic Niño Index to detect the main periods governing the signal and to extract the components underlying its variability. The periods and modes in question appeared globally in agreement with previous studies and brought valuable information for the elaboration of a model predicting the long-term trends of the signal. The proposed model fits in the growing body of evidence suggesting that long-term predictions of ONI are much more possible than previously

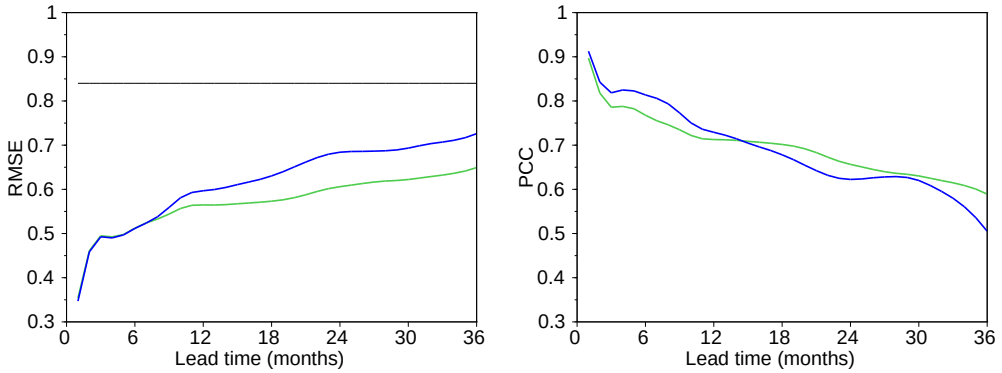


Figure 5.7: RMSE and PCC between the forecasted values and the signal as functions of the lead time. The results for the period 1995-2015 are in blue. The green curve represents the results for the period 1975-2015 for the curious minds wondering what would be the skills if the model was applied as it is for a longer period of time. The black line in the first panel is the standard deviation of ONI. Since it has zero mean, this line can be viewed as the skill of a model where all the forecasted values are set to zero.

thought and showed that early signs of major EN and LN events can be detected years in advance. This model could improve our understanding and forecasting skills of EN and LN. More importantly, the proposed technique or, at least, the essence of the algorithm (i.e. phasing appropriate components with warm or cold events), could be combined with other models which are more accurate for short-term predictions. This complementarity could give rise to models able to predict ONI at a large range of lead times.

Future work will consist in incorporating the seasonal (near-annual and annual) variability to improve short-term predictions and the timing and intensity of EN and LN events in long-term forecasts, which remains the main strength of the model. Moreover, we will continue to work on the development of the prediction of the peaks of the components extracted from the CWT, which are the cornerstones of the model and dictate its forecasting skills. The time variations in the periods, phases and amplitudes will also be studied in more detail to improve the predictions. Due to the effects that EN and LN events induce worldwide, predictions 1-2 years ahead could be intelligently used to better prepare for the consequences.

*We acknowledge the Climate Prediction Center (CPC) for providing the ONI signal ([26]) and the WDC-SILSO, Royal Observatory of Belgium, Brussels for the sunspot number signal ([131]). We also wish to thank Dr. Desislava Petrova for providing fruitful discussions and suggestions that improved the quality of the work presented in this chapter.*

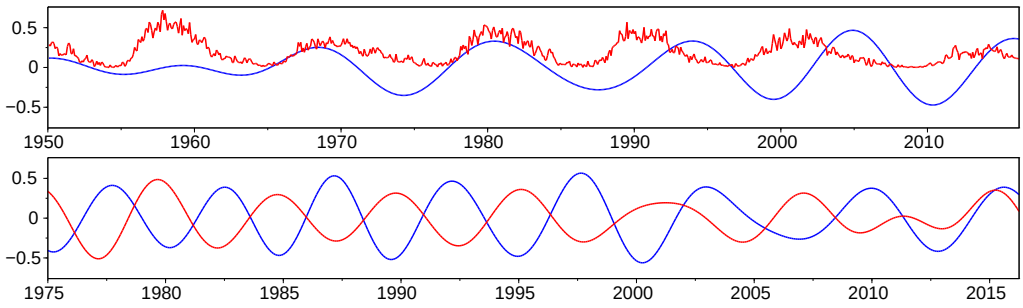


Figure 5.8: Top: Sunspot number signal (red) and $c_{140}$ (blue) plotted from 1950 for better visualization. Bottom: Components with period of $\approx 61$ months extracted from the sunspot number signal (red) and from ONI (blue). The anti-phase between them is striking. The red curve has been divided by 500 on the first panel and by 50 on the second one for a better visualization.

# Appendix

## 5.A Comparison with sun-induced components

We briefly investigated if the components extracted from ONI could be related to similar components extracted from the sunspot number signal (SN). This is purely for information purposes. It could be of interest for some specialists and deserves more examination. However, we do not expand on that subject since it is far beyond the purpose of this chapter.

First, it turns out that $c_{140}$ is moderately correlated with SN given the correlation coefficient of 0.43 from 1962 to 2012, where $c_{140}$ is the most reliable (see Figure 5.8). This may imply that a solar forcing occurs in the tropical decadal Pacific variability and could contribute for a non-negligible part of ONI. Moreover, when the 11 years cycle is removed from SN, the CWT reveals that the highest peak of the WS of the so-obtained signal is located at a period of $\approx 64$ months (giving the mode $s_{64}$), which calls for a comparison with $c_{61}$. As shown in Figure 5.8, it appears that $s_{64}$ and $c_{61}$ are completely anti-phased for the years between 1975 and 2000, with a correlation coefficient of $-0.85$. If we consider a left shift of $c_{61}$ by half its period (30 months), the correlation between the curves extends to 2008 with a coefficient reaching 0.90 for the 1975-2008 period. This intriguing observation is reinforced by the fact that they even anti-phase during their anomalously long oscillation in the years 1998-2005 for SN and 2000-2007 for $c_{61}$. This could deserve a deeper examination by specialists.

## 5.B Details for $y_{43}^1$

For simplification, let us write $s$ instead of $s_3$ and $y$ instead of $y_{43}^1$. If $y$ is already known up to time $t-1$, here are the steps describing how to obtain $y(t)$. We note $p(t-1)$ the position of the peak used to generate $y(t-1) = A_{43}\cos(2\pi(t-1-p(t-1))/43)$. We use a variable called *lock* to prevent abrupt changes from $p(t-1)$ to $p(t)$. To obtain $p(t)$, proceed as follows.

```
if lock=1 then
   if s(t)>s(t-1) and s(t-1)>0 then p(t)=p(t-1)+1
   else p(t)=p(t-1); if s(t-1)>0 and s(t)<0 then lock=0
else
   a=abscissa of the last local max of s
   if s(a)>0.5 then
      if p(t-1)+floor(period/2) > a then p(t)=p(t-1)
      else p(t)=a; lock=1
   else p(t)=p(t-1)
```

Then $y(t) = A_{43}\cos(2\pi(t-p(t))/43)$. Special mention for $y_{61}$: if it comes that $y_{61}$ reaches a peak before $s_1$, impose that $y_{61}$ stays at $A_{61}$.

## 5.C An informative comparison with other models

### Skills of state-of-the-art dynamical and statistical models

Many dynamical and statistical models are evaluated in [20]; Figure 5.9 displays the results relevant in our work.

### Comparison with our model

The skills of our model (Figure 5.7) are compared to those of [117] and [20] in Figure 5.10. It is important to note that this comparison is for information purposes only, it should not be considered as an official result. Indeed, authors in [117] make forecasts of the raw Niño 3.4 time series (not the anomalies or the smoothed ONI) which displays more high-frequency variability. The results provided in [20] are computed for the period 2002-2011 and they are operational forecasts, meaning that the forecasts are not retrospective, but issued in real time. Therefore, Figure 5.10 only gives indications (rather than accurate quantitative measurements) that our model is performing well compared to state-of-the-art methods.

Unsurprisingly, it appears that the other models display slightly better performances at short lead times than ours because they involve more parameters than the sole ONI

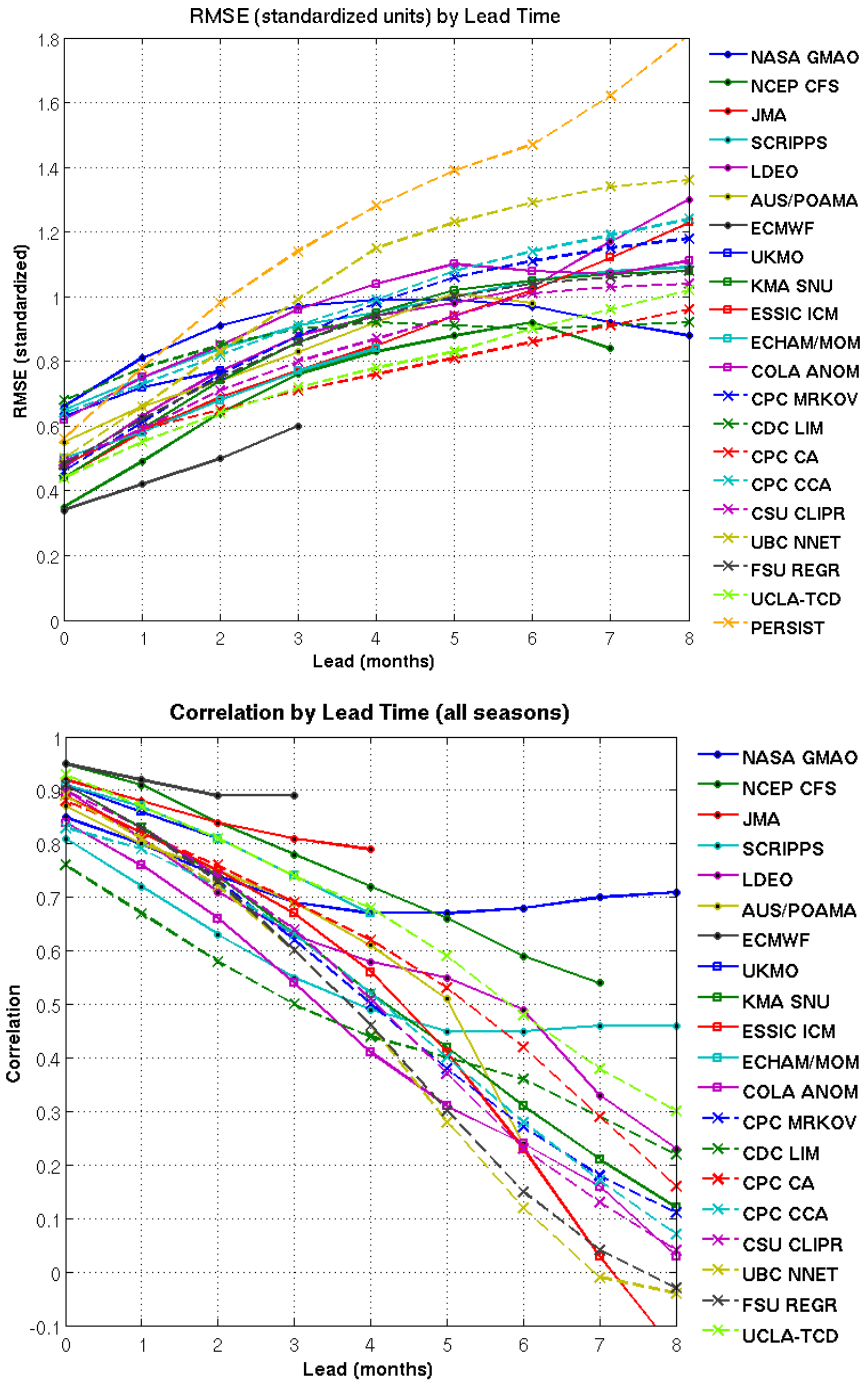


Figure 5.9: Skills (RMSE and PCC) for several dynamical and statistical models as functions of the lead time, from [20]. Dashed lines and cross symbols represent the statistical models. The other lines correspond to the dynamical ones.

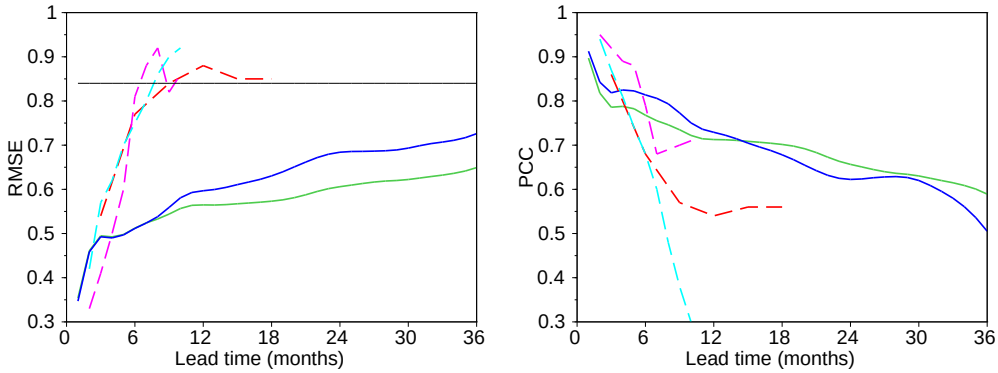


Figure 5.10: Comparison between our results (blue and green curves from Figure 5.7) and other models. The red dashed line corresponds to the results exposed in [117], the cyan one represents the skills of the best statistical models from Figure 5.9 and the magenta one is for the best dynamical models of Figure 5.9 (the best data point from each set of models is taken for each lead time).

index and they take some dynamical principles and high-frequency variability into account. However, it seems that our model outperforms the others at longer lead times ($> 6$ months) and, as mentioned, decays more slowly. Also, the RMSE of the other models is above the standard deviation threshold for lead times exceeding $\approx 6 - 8$ months, which indicates excessively large deviations from the observed data for mid-term predictions.

# Chapter 6

# Wavelet-Induced Mode Extraction

After completing our study of the ENSO index, it appeared to us that the decomposition technique used in chapter 5 would not be appropriate to extract AM-FM components from much trickier signals. Several well-established techniques (see below) seemed better suited for that particular task. However, despite exhibiting various strengths, they also have different kinds of weaknesses. As a consequence, we decided to implement our own wavelet-based mode decomposition method while trying to resolve these problems. The result of this thought is presented in this chapter and an article on this method is currently under review ([42]).

## 6.1 Introduction

Extracting the components that constitute a given amplitude modulated-frequency modulated (AM-FM) signal is undoubtedly a subject of primary importance in many areas involving signal processing and analysis. Among the multiple benefits of such decompositions, one can mention that it allows to better understand the underlying mechanisms governing the signal, to extract its main frequencies and their temporal variations and to rule out noisy parts or irrelevant information for the study carried out. These aspects are generally encapsulated in a time-frequency (TF) representation of the signal and/or of the extracted components, which helps visualize the information contained in the signal from a time, energy and frequency point of view simultaneously [54].

One of the most popular ways to tackle such a task is called the Empirical Mode Decomposition (EMD [55, 71, 124]), which is described in appendix 6.A. It is a complete adaptive algorithm that decomposes a signal into "intrinsic mode functions" (IMFs)

that are, roughly speaking, AM-FM signals with slowly time-varying amplitudes and frequencies (i.e. they can be viewed as locally harmonic [35]). The EMD has proven its effectiveness in many situations (such as medicine [31, 33], climatology [153], finance [72], geophysics [70]) despite its lack of mathematical background, which is often mentioned as its main drawback [35, 61]. Moreover, by using the EMD, one has little control over the results since no parameter can be tuned in this rather hermetic heuristic algorithm. Even though it has been shown to act as an adaptive filter bank [55] and that many other studies have investigated its properties, methods that can be analytically described are also needed.

Wavelet transforms are now well-established tools for signal analysis and are provided with a rather strong mathematical theoretical background and with an inverse transform, which is the backbone of reconstruction procedures (see e.g. [34, 35, 98]). However, in the classic CWT analysis, all (or, in practice, many) wavelet coefficients are needed to accurately rebuild the original signal and the area of the TF plane needed for the reconstruction has to be manually selected (as in e.g. [35, 60]). Approaches such as in [104] resolve that problem by giving an automated way to determine which wavelet coefficients to use, but it appears that this method is relatively rigid and cannot deal with close frequencies nor with non-stationary signals. Other techniques such as in [61] consist in performing a segmentation of the Fourier spectrum of the signal in order to isolate the highest local maxima and then build a wavelet basis associated with each so-obtained segment. Some kind of inverse wavelet transform allows the extraction of a component per segment. The results presented in [61] are interesting and the idea of segmenting the Fourier domain is appealing, but it turns out that the procedure described is rather complicated and is not well-suited for the analysis of e.g. "highly" non-stationary signals having an "erratic" Fourier spectrum. Let us also mention works such as [127], in which some curves called "skeletons" are extracted from the wavelet transform by considering stationary points in the "time-phase"[1] plane that satisfy some properties. The idea is interesting as well but it does not necessarily lead to components that can be viewed as signals (i.e. functions of time).

In this chapter, we develop a wavelet-based mode decomposition that we call Wavelet-Induced Mode Extraction (WIME). This method aims to extract automatically signal-length AM-FM components that are present in a signal. It is inspired by some of the above-mentioned techniques and attempts to resolve most of their problems. The rest of the chapter is organized as follows. We first explain the concepts and the main ideas that animate WIME, before describing the algorithm in detail. We then apply WIME on toy examples and on two homemade signals that illustrate its advantages over the other methods, we compare its skills with the EMD, test its tolerance to noise and discuss the results. Finally, we apply it with two real-life signals (electrocardiogram and ONI index) and draw some conclusions.

[1] Understand "time-frequency-argument" plane, i.e. $(a, b) \mapsto \arg(W_f(a, b))$.

## 6.2 Wavelet-Induced Mode Extraction

In this section we first give the intuitive ideas that relate to WIME before going into further details. As a preliminary remark, one has to be aware of the class of functions that can be handled while developing a specific tool for signal analysis. Without going into technical details, it appears obvious that we aim to deal with real-valued AM-FM signals of the type:

$$f(t) = \sum_{k=1}^{K} a_k(t) \cos(\phi_k(t)), \tag{6.1}$$

where some conditions as in [35] may be imposed on $a_k(t)$, $\phi_k(t)$ or $\phi'_k(t)$. As far as we are concerned, we will only assume that the amplitudes, frequencies and their derivatives are "smooth" in an intuitive sense. In [35], such functions are called a "superposition of well-separated intrinsic mode components" and the conditions in question are examined minutely. It is clear that this class of functions is relatively large and that many real-life signals can be (at least partly) approximated by AM-FM components, even though pre-/postprocessing treatments may be required.

### 6.2.1 Main ideas of the method

Basically, the first step is to perform a CWT of the signal using a Morlet-like wavelet as in chapters 4 and 5, which has proven to be well-suited for TF analysis of oscillating functions ([104, 141]). Let us remind that the modulus of this CWT can be seen as a TF representation of the signal. The wavelet spectrum (WS) is computed following equation (5.1) and segmented in order to isolate its largest local maximum in a frequency band.

Then, we choose a starting point with high energy in the TF plane in the selected time-frequency band and determine a ridge of high energy forward and backward from this point up to the edges of the plane while adapting the frequency window as we go along the ridge. A component modulated in amplitude and frequency by the modulus and argument of the CWT along that ridge can be extracted with equation (4.3) used throughout chapter 4 (i.e. two times the real part of the CWT along the ridge).

Finally, we subtract this component from the signal in order to unveil information potentially hidden by the dominant mode and repeat the whole process with this newly obtained signal. The procedure is iterated until the components extracted are no longer relevant.

Let us briefly comment some of the aspects of the proposed algorithm and contrast them with other methods. First, the use of equation (4.3) in the case of AM-FM signals is motivated by the following idea. If $f(t) = A(t)\cos(\phi(t))$, then around a given time $t_0$ one has

$$f(t) \approx A(t_0)\cos(\phi(t_0) + \phi'(t_0)(t - t_0))$$

by truncated Taylor series ([35]). Now, if we simply mimic the procedure explained in chapter 4, we get that if $a^*(t_0)$ denotes the scale at which $a \mapsto |W_f(a, t_0)|$ reaches its

maximum, then the instantaneous frequency $\phi'(t_0)$ can be recovered from the fact that $a^*(t_0) = \Omega/\phi'(t_0)$ and Eq. (4.3) evaluated at $t_0$ and $a^*(t_0)$ gives back a value close to $f(t_0)$. Using the same process at each time $t$, AM-FM signals can thus be recaptured as

$$f(t) \approx 2|W_f(a^*(t), t)| \cos(\arg(W_f(a^*(t), t))).$$

Then, segmenting the wavelet spectrum instead of the Fourier spectrum (as in [61]) has the advantage of being easier since the wavelet spectrum is usually much smoother. For example, chirps will generally be handled comfortably with WIME while their Fourier spectra are extremely irregular and are therefore more difficult to segment. Also, unlike skeletons computed in [127], the ridges considered here can be viewed as functions of time and thus allow to derive signal-length components. Moreover, regarding [124], the EMD extracts the IMFs of a signal one after another, sorting these by decreasing frequency. However, such an approach does not take into account the energetic hierarchical order of the components that build the signal. WIME resolves that problem by extracting the components successively by sorting them with respect to their energy level, starting with the most energetic ones. In this way, some kind of natural order is respected for the extraction, which is particularly useful when the TF representation of the signal displays, for example, intersecting curves.

### 6.2.2 Description of the algorithm

We now describe in detail the WIME algorithm. The wavelet $\psi$ used in this study is still the one used in chapters 4 and 5 defined by equation (4.2).

The algorithm of WIME applied on a signal $f$ defined on a time interval $T$ consists in the following steps:

1) Perform the CWT of $f$:

$$W_f(t, a) = \int_T f(x)\bar{\psi}\left(\frac{x-t}{a}\right)\frac{dx}{a}$$

as in chapter 4[2].

2) Compute the wavelet spectrum $\Lambda$ associated with $f$:

$$a \mapsto \Lambda(a) = E_t\,|W_f(t, a)|$$

where $E_t$ denotes the mean over time, as in chapter 5.

3) Locate the scale $a^*$ at which $\Lambda$ reaches its highest local maximum and isolate it between the scales $a_1$ and $a_2$ at which $\Lambda$ displays the left and right local minima that are the closest to $a^*$. Set $A = [a_1, a_2]$.

[2]Note that we choose to write $W_f(t, a)$ instead of $W_f(a, t)$ so that the ridge $(t, a(t))_{t\in T}$ can actually be seen as the function $t \mapsto a(t)$ in the TF plane.

4) Define $(t_0, a(t_0))$ in the time-frequency band $T \times A$ of the TF plane as:

$$(t_0, a(t_0)) = \underset{(t,a)\in T\times A}{\operatorname{argmax}} |W_f(t,a)|,$$

which is the starting point for the ridge detection step.

5) Compute[3] the ridge $(t, a(t))_{t\in T}$ forward and backward that stems from $(t_0, a(t_0))$:

   a) Compute $b_1$ and $b_2$ such that $b_2 - b_1 = a_2 - a_1$ and $a(t_0) = (b_1 + b_2)/2$, i.e. center $a(t_0)$ in a frequency band of the same length as the initial one.

   b) Among the scales at which the function $a \mapsto |W_f(t_0 + 1, a)|$ with $a \in [b_1, b_2]$ reaches a local maximum, define $a(t_0+1)$ as the closest one to $a(t_0)$. If there is no local maximum, then $a(t_0 + 1) = a(t_0)$.

   c) Repeat step 5) with $(t_0 + 1, a(t_0 + 1))$ instead of $(t_0, a(t_0))$ until the end of the signal.

   d) Proceed in the same way backward from $(t_0, a(t_0))$ until the beginning of the signal.

6) Extract the component associated with the ridge:

$$t \mapsto 2|W_f(t, a(t))| \cos(\arg W_f(t, a(t))),$$

7) Subtract this component (say $c_1$ at the first iteration) from $f$ to get the rest $r_1 = f - c_1$ and repeat steps 1 to 7 with $r_1$ instead of $f$. Obtain $c_2$, repeat with $r_2 = r_1 - c_2$, etc.

8) Stop the process (iterating steps 1 to 7) when enough energy has been drained from the signal. More precisely, if the components already extracted are denoted by $(c_i)_i$ for $i = 1, ..., N$ then stop if

$$\|r_N\| < \alpha \|f\|,$$

where we set the threshold $\alpha = 0.05$ and $\|.\|$ denotes the energy of a signal from the signal analysis point of view as in chapter 5 (i.e. as the square of the $L^2$ norm).

The so-obtained components successively extracted are the counterparts of the IMFs from the EMD and their sum provides an accurate reconstruction of $f$. The signal $c_0 = f - \sum_{i=1}^{N} c_i$ is considered as the remaining "noise" and therefore the decomposition of $f$ can be completed with this component, i.e. $f = \sum_{i=0}^{N} c_i$. Let us note that the ridge extraction can be made more difficult if many components of similar energy and frequency are added together within the signal. To overcome these difficulties, reallocation methods ([17, 28, 27]) such as synchrosqueezing ([35, 36]) that sharpen the TF representation of the signal might be useful before the computation of the ridge.

[3]For this step, keep in mind that we are working with signals, i.e. discrete time series and not functions defined on $\mathbb{R}$. We can thus move from "one point to the next", i.e. the points located around $t_0$ can be considered as located at times $..., t_0 - 2, t_0 - 1, t_0, t_0 + 1, t_0 + 2, ....$

Table 6.1: Comparison of the extraction and reconstruction skills of WIME and the EMD for the signal used in section 6.3.1. The signal $s_n$ corresponds to the $n^{\text{th}}$ component $c_n$ (displayed in Figure 6.1) in the case of WIME and to the $n^{\text{th}}$ IMF in the case of the EMD. The last line compares the initial signal $f$ and the reconstructed signal $f_r$ defined as the sum of the components $(s_n)_n$ related to each case.

| Signals | WIME | | EMD | |
|---|---|---|---|---|
| | RMSE | PCC | RMSE | PCC |
| $s_1, f_1$ | .261 | .987 | .163 | .995 |
| $s_2, f_2$ | .070 | .998 | .171 | .989 |
| $f_r, f$ | .267 | .991 | .151 | .997 |

## 6.3 Experiments

### 6.3.1 Basic example

We now apply WIME on several signals in order to prove its effectiveness in various situations and depict some of its properties. We also compare its performances with the EMD. For that purpose, the first example illustrates how WIME actually works. We consider the function $f = f_1 + f_2$ defined on $[0, 1]$ as the sum of two AM-FM components:

$$f_1(t) = (2 + \sin(5\pi t)) \cos(100(t - 0.5)^3 + 100t)$$
$$f_2(t) = \begin{cases} (1.5 + t) \cos(0.2e^{10t} + 350t) & \text{if } t \leq 0.5 \\ t^{-1} \cos(-300t^2 + 1000t) & \text{if } t > 0.5 \end{cases}$$

The signal and the steps of WIME applied to $f$ are represented in Figure 6.1. One can see that the first TF representation (i.e. $(t, a) \mapsto |W_f(t, a)|$) shows very distinctly the bricks used to build $f$. At the first step, the wavelet spectrum displays more energy (highest peak) around the 20Hz frequency. The component $c_1$ extracted in that region clearly corresponds to $f_1$. At the next step, only the footprint of $f_2$ remains in the TF plane; the corresponding component $c_2$ clearly matches with $f_2$. Naturally, the reconstruction of $f$ thanks to $c_1$ and $c_2$ is highly accurate, as shown in Figure 6.1. Quantitative measurements through RMSE and PCC of the extraction and reconstruction skills of WIME and of the EMD can be found in Table 6.1. It appears that both methods display excellent skills, as expected for this basic example.

### 6.3.2 A more intricate example

The second example considered is taken from [124] and is one of the classic examples that prove the effectiveness of the EMD. The signal consists of the sum of two FM sinusoidal signals and a Gaussian wavepacket (see [124]). The FM components are

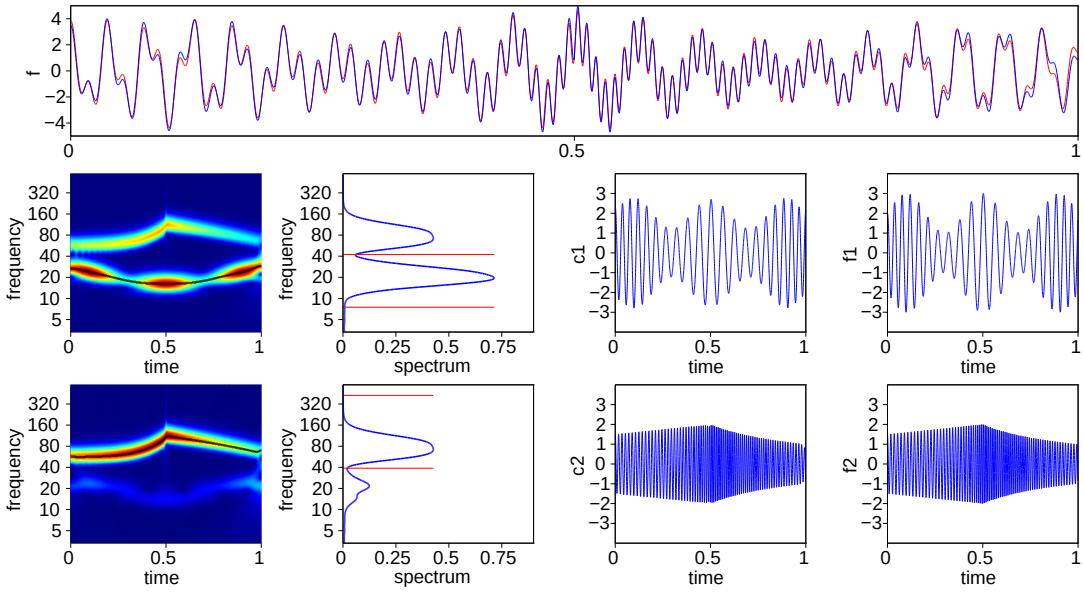


Figure 6.1: Top row: original signal $f$ (blue) and reconstructed signal (red) of section 6.3.1. Second row, from left to right: $|W_f(t,a)|$ (stands for the TF representation of $f$) and the corresponding ridge detected (black line), wavelet spectrum of $f$ and its segmentation (red lines) to isolate the highest local maximum (used to set a starting point for the ridge), first component $c_1$ extracted following the ridge, original first component $f_1$. Last row: the same figures with $f - c_1$ instead of $f$. Clearly, $c_1$ and $c_2$ successively extracted match $f_1$ and $f_2$.

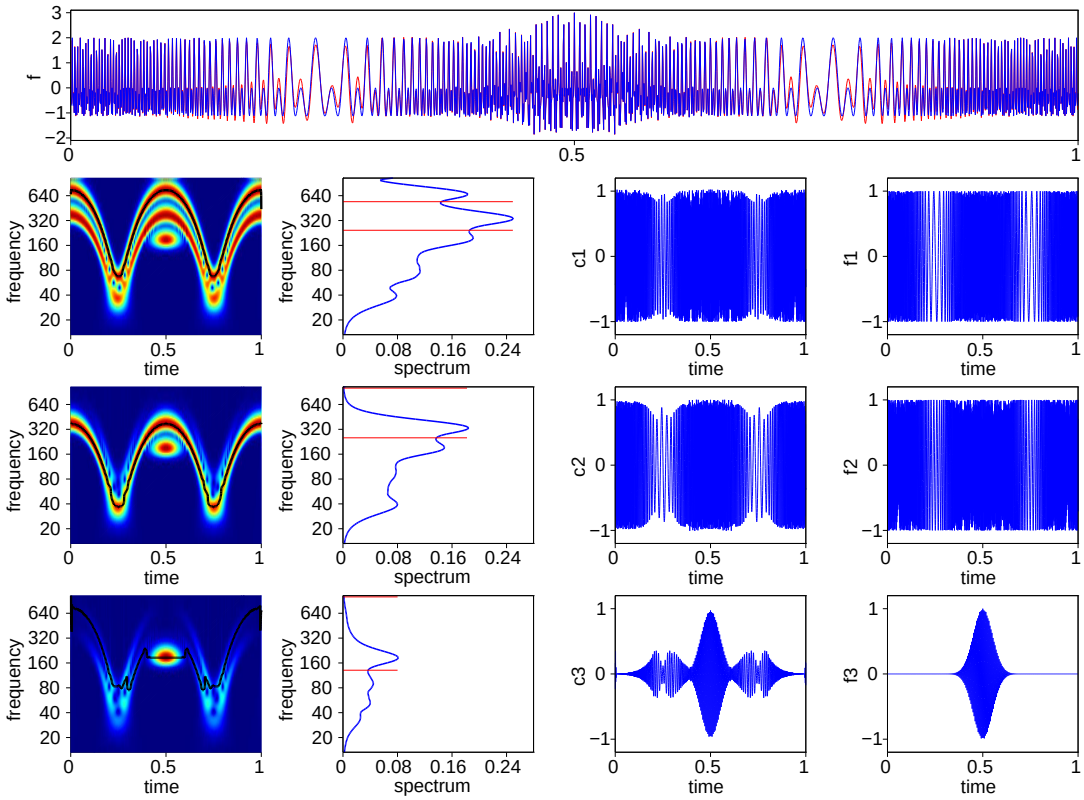


Figure 6.2: Top row: original signal $f$ (blue) from the EMD test examples [124] and reconstructed signal (red) (section 6.3.2). As for Figure 6.1, the other rows are, for the successive signals under consideration: $|W_f(t,a)|$ and ridges (black line), wavelet spectra and their segmentations (red lines), components extracted following the ridges, original components.

Table 6.2: Extraction and reconstruction skills of WIME for the signal used in section 6.3.2, with the same notations as in Table 6.1. The fourth line compares $c_3$ and $f_3$ on the interval $[0.35, 0.65]$.

| Signals | WIME | | EMD | |
|---|---|---|---|---|
| | RMSE | PCC | RMSE | PCC |
| $s_1, f_1$ | .128 | .984 | .125 | .985 |
| $s_2, f_2$ | .194 | .963 | .100 | .990 |
| $s_3, f_3$ | .128 | .846 | .076 | .933 |
| $s_3^*, f_3^*$ | .058 | .988 | .095 | .970 |
| $f_r, f$ | .174 | .986 | .048 | .998 |

"highly" non-stationary, as seen in the TF representation in Figure 6.2. Nevertheless, since the three components are somehow "well-separated" in the TF plane, WIME is able to deal with the non-stationarity and extracts more than satisfyingly the original components of $f$, as seen in Figure 6.2. Note that, during the extraction step of $c_3$, since WIME is programmed to extract a signal-length component by default, superfluous parts are kept outside the support of the Gaussian wavepacket (which is not exactly of the form of equation 6.1); simple postprocessing treatments could resolve that problem if needed. Again, the reconstructed signal is extremely close to $f$, which shows the effectiveness of WIME in decomposing thorny non-stationary signals. Its extraction and reconstruction skills are presented in Table 6.2 and compared to the EMD. It appears that both techniques display remarkable aptitudes in the present case, with a slight advantage for the EMD.

### 6.3.3 Crossings in the time-frequency plane

We now apply WIME and the EMD to homemade toy examples for which the TF plane displays features not studied in [61] nor in [124]. We consider a function made of three FM signals whose TF representations display some crossings and with constant amplitudes of $1.25, 1, 0.75$. We consider $f(t) = f_1(t) + f_2(t) + f_3(t)$ for $t \in [0, 10]$ with

$$
\begin{aligned}
f_1(t) &= 1.25 \cos\Big( -(t-3)^3 + 180t \Big) \\
f_2(t) &= \cos\left(1.8^t + 20t\right) \\
f_3(t) &= \begin{cases} 0.75\cos(-1.6\pi t^2 + 20\pi t) & (t < 5) \\ 0.75\cos(4\pi t) & (t \geq 5) \end{cases}
\end{aligned}
$$

and we then set $f(10+t) = f(10-t)$ for every $t \in [0, 10]$ (i.e. $f$ is concatenated with its mirror).

The TF representation of this signal displays, as wanted, multiple crossings between the patterns associated with each component (see Figure 6.3). However, as it can be seen

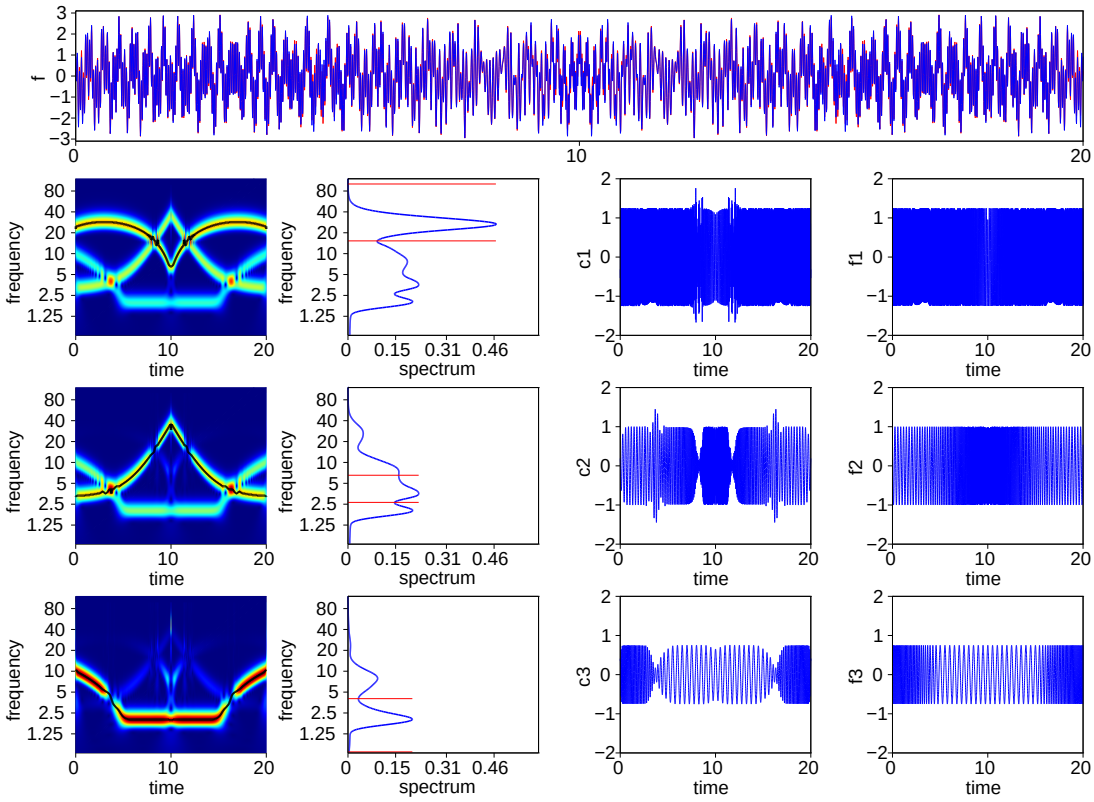


Figure 6.3: As for the previous figures, the top row displays the original signal $f$ (blue) and the reconstructed one (red) of section 6.3.3 and the other rows are, for the successive signals under consideration: $|W_f(t,a)|$ and ridges (black line), wavelet spectra and their segmentations (red lines), components extracted following the ridges, original components. Clearly the influence of the multiple crossings in the TF plane remains limited because WIME respects the energy-based hierarchical order of the components.

in Figure 6.3, the energy corresponding to each component allows WIME so successfully retrieve the original components; the influence of the crossings remains extremely low. Naturally, when a crossing occurs, WIME follows the "first come, first served" principle: the energy is consumed by the first component that has the crossing on its way, and when another component reaches that point, there is no energy left for it even though it should have been the case. This phenomenon can be clearly seen in Figure 6.3 and is unavoidable without treating/adjusting a component before extracting the next one. Nevertheless, the components obtained respect the hierarchical order imposed by their energy level and remain easily interpretable from a physical point of view.

This example also shows how the EMD proceeds to extract successive components, and why it is not well-adapted in that type of case. The EMD acts as a bandpass

Table 6.3: Extraction and reconstruction skills of WIME for the signal used in section 6.3.3, with the same notations as previously. In this case, since the components are not recovered by the EMD, the comparison is only possible with the reconstructed signal.

| Signals | WIME | | EMD | |
|---|---|---|---|---|
| | RMSE | PCC | RMSE | PCC |
| $s_1, f_1$ | .156 | .984 | N/A | N/A |
| $s_2, f_2$ | .193 | .962 | N/A | N/A |
| $s_3, f_3$ | .131 | .970 | N/A | N/A |
| $f_r, f$ | .111 | .996 | .133 | .994 |

filter [55], filtering components following a frequency-decreasing order, i.e. high frequencies IMFs are extracted first, regardless their energy level. From a TF representation perspective, this corresponds to successively extract components related to the "upper ridge" present in the considered signal, then subtracting it, extracting the next "upper ridge", and so on. This is illustrated in Figure 6.4, which displays the first three IMFs obtained with the EMD from $f$ and their CWT-based TF representation[4]. This also depicts why the EMD has such effective reconstruction skills: at the end of the process, as for WIME, all the energy of the TF plane has been drained, ridge after ridge. This can be seen in Table 6.3 which displays the skills of the methods. The problem lies in the fact that the hierarchical order imposed by the amplitudes of the three components is not respected at all with the EMD, which thus gives IMFs that are not as easily interpretable from a physical point of view. Even though it is probably useful to have such a filtering approach in some cases (e.g. for denoising purposes), something is clearly wrong in this case. Besides, the EMD has no choice but following that order of filtering whereas WIME is more flexible and could be adapted to perform a similar task if needed.

The first two examples showed that WIME successfully retrieves components that are "well-separated" in the TF plane, where the intuitive conditions to be "well-separated" (avoiding crossings) could be defined with frequency-based formulas as in [35]. However, the third signal clearly shows that when the components are not "well-separated" with respect to their frequencies but are distinguishable by their amplitudes, then WIME still manages to recover the original sources of the signal, while methods such as the EMD or [61] cannot.

[4]The TF-representation by default of the IMFs extracted from the EMD is performed with the Hilbert transform, see e.g. [71]. We used the CWT to facilitate comparison with the other signals analyzed in this chapter.

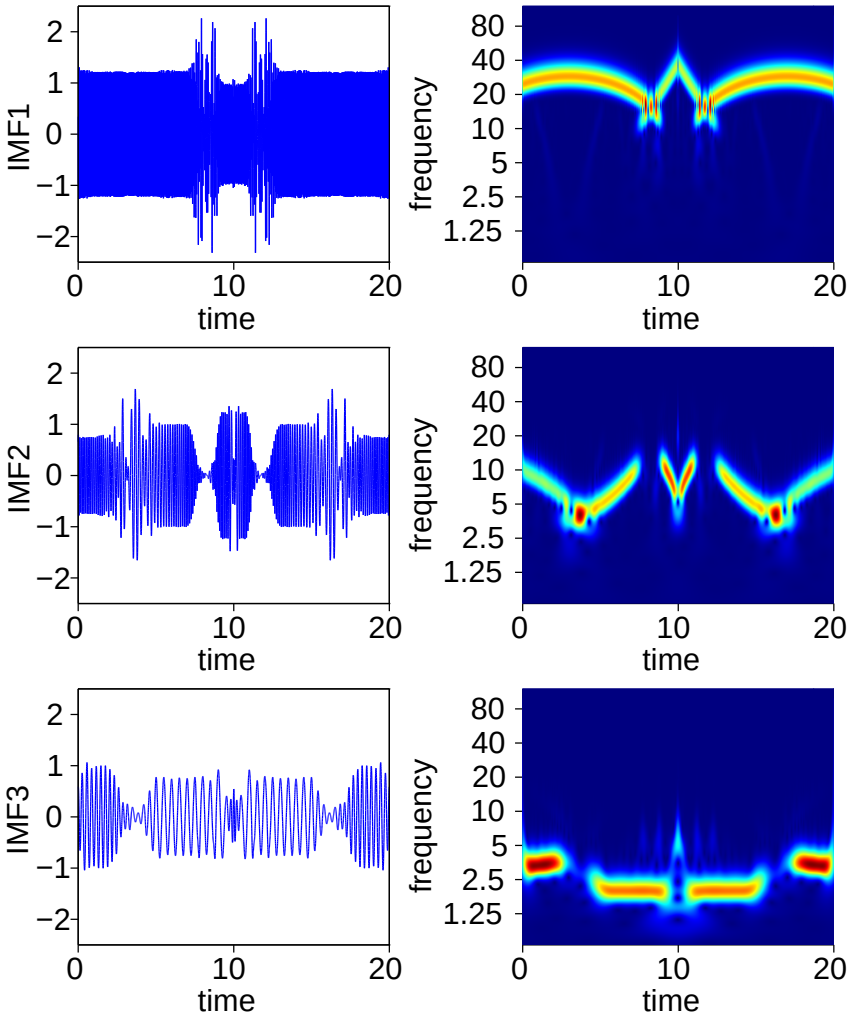


Figure 6.4: Left column: IMFs extracted with the EMD from the signal of section 6.3.3. Right column: their TF representation obtained with the CWT. It can clearly be seen that the EMD works following a decreasing-frequency based approach, regardless the amplitudes of the components/IMFs to be extracted. Consequently, the IMFs only match the original components piecewise.

### 6.3.4 Mode-mixing problem

We now address the mode-mixing problem that occurs when a signal is made of AM-FM components whose frequencies are relatively close to each other, i.e. the components are not "well-separated" with respect to their frequency nor with their amplitudes. In this example, the primary objective is not to recover exactly the original components of the signal (such a thing is arduous whatever the method used) but rather to show that, despite the complexity of the signal and the mixing modes, the main frequencies present within the original components can be easily recovered with WIME while the EMD is not able to do so. The signal $f$ considered for that purpose is made of one AM-FM component and three AM components ($t$ takes integer values from 1 to 800):

$$
\begin{aligned}
f_1(t) &= \left(1 + 0.5\cos\left(\frac{2\pi}{200}t\right)\right)\cos\left(\frac{2\pi}{47}t\right) \\
f_2(t) &= \frac{\ln(t)}{14}\cos\left(\frac{2\pi}{31}t\right) \\
f_3(t) &= \frac{\sqrt{t}}{60}\cos\left(\frac{2\pi}{65}t\right) \\
f_4(t) &= \frac{t}{2000}\cos\left(\frac{2\pi}{23 + \cos\left(\frac{2\pi}{1600}t\right)}t\right),
\end{aligned}
$$

so that the target frequencies to detect are respectively 1/47, 1/31, 1/65, and $\approx$ 1/23 Hz[5].

A peculiarity of this example is that the first component clearly dominates the signal (see Figure 6.5), with a mean energy much higher than the others. This has the effect of eclipsing the other components at first sight and, looking at the first wavelet spectrum, it is complicated to tell which frequencies are present in the signal. In the case of WIME though, the successive subtractions of the components unveil the less powerful ones, as shown in Figure 6.5 and so allow to detect almost exactly the target frequencies. The fact that hidden information may appear when dominant modes are correctly identified and taken off the signal may be useful in real-life data analysis such as daily temperature signals with a dominant mode of 365 days. Therefore, even though the components retrieval is satisfying but not as accurate as in the previous examples, substantial information can still be obtained with WIME.

As for the previous example, the EMD does not perform so well in this case. The first four IMFs extracted with the EMD are represented in Figure 6.6. While the components extracted with WIME are somehow close to the real ones, with the target frequencies unquestionably recovered, the IMFs have clearly nothing in common with the original components. With a PCC with $f$ close to 0.93, the first IMF is almost the initial signal itself and with estimated frequencies of $\approx$ 1/41, 1/75, 1/165, 1/284 Hz (instead of $\approx$ 1/23, 1/31, 1/47, 1/65), we can safely conclude that the EMD fails the frequency detection

[5]The perspicacious reader will notice (intentional) similarities with the ONI index used in chapter 5.

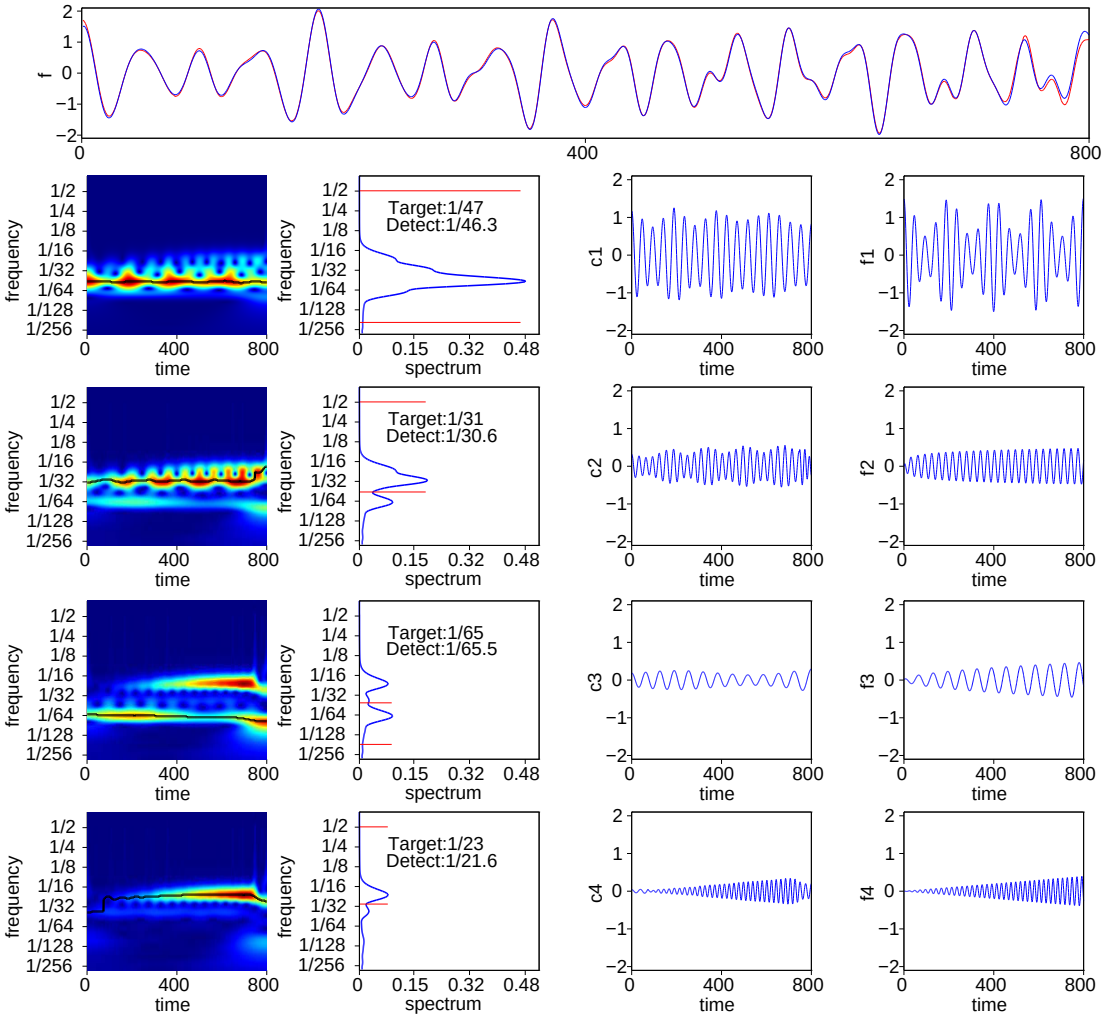


Figure 6.5: As for previous figures, the top row displays the original signal $f$ (blue) and the reconstructed one (red) (section 6.3.4); the other rows are, for the successive signals under consideration: $|W_f(t,a)|$ and ridges (black line), wavelet spectra and their segmentations (red lines), components extracted following the ridges, original components. Even though the amplitudes of the extracted components do not match the original ones as close as in the other cases, the period detection skill of WIME is high. The identification of the main periods present within the signal is effective.

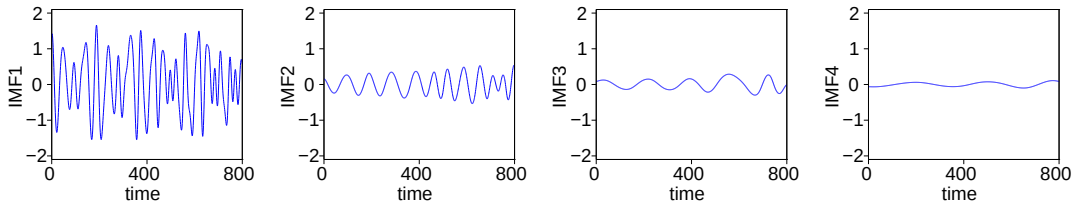


Figure 6.6: IMFs obtained with the EMD from the signal of section 6.3.4. Clearly, they are considerably different from the original components; the first IMF itself represents almost the whole signal. The estimated frequencies ($\approx$ 1/41, 1/75, 1/165, 1/284 Hz) are far from the targets ($\approx$ 1/23, 1/31, 1/47, 1/65).

Table 6.4: Extraction and reconstruction skills of WIME for the signal used in section 6.3.4. In the third line $s_3^*$ corresponds to $\mathrm{IMF}_2$ for the EMD. The components are not recovered by the EMD, the comparison is only possible in some cases.

| Signals | WIME | | EMD | |
|---|---|---|---|---|
| | RMSE | PCC | RMSE | PCC |
| $s_1, f_1$ | .205 | .962 | .458 | .831 |
| $s_2, f_2$ | .109 | .932 | N/A | N/A |
| $s_3^*, f_3$ | .170 | .694 | .259 | .462 |
| $s_4, f_4$ | .070 | .902 | N/A | N/A |
| $f_r, f$ | .064 | .997 | .068 | .998 |
| $\mathrm{IMF}_1, f$ | N/A | N/A | .316 | .925 |
| $\mathrm{IMF}_1 + \mathrm{IMF}_2, f$ | N/A | N/A | .170 | .980 |

test. As in the previous cases, a comparison of the skills of the methods is presented in Table 6.4, which illustrates the nice performance of WIME compared to the EMD.

### 6.3.5 Tolerance to noise

Finally, we perform a resistance to noise test with WIME. Given the intrinsic nature of WIME, more precisely the CWT part which involves convolutions with a smooth kernel, it can be expected that WIME displays some kind of natural tolerance to noise. In the same spirit as in [35], we consider a chirp $f$ defined on $[0, 1]$ by

$$f(t) = \cos(70t + 30t^2),$$

we generate a Gaussian white noise $X$ of zero mean and variance 1 and we run WIME on $f$, $f+X$, $f+2X$ and $f+3X$. For the noisy signals $f+nX$ with $n > 0$, the corresponding signal-to-noise ratio (SNR) is defined as in [35] by

$$\mathrm{SNR[dB]} = 10 \log_{10} \left( \frac{\mathrm{Var}(f)}{\mathrm{Var}(nX)} \right).$$

Table 6.5: Reconstruction skills of WIME in the presence of noise with the only component extracted.

| Signals | SNR | RMSE | PCC |
|---|---|---|---|
| $f_r, f + X$ | -2.792 | .129 | .983 |
| $f_r, f + 2X$ | -8.812 | .193 | .962 |
| $f_r, f + 3X$ | -12.330 | .263 | .929 |

In the present case, the SNRs considered are respectively -2.792, -8.812 and -12.330 dB, indicating a particularly high level of noise in the last two cases. The results obtained on these noisy signals are displayed in Figure 6.7. It can be noted that WIME successfully extracts $f$ from the signals despite the high level of noise, especially in the third and fourth cases. This capacity is quantified more in detail in Table 6.5. It is important to note that such excellent results are obtained with no extra computational cost, i.e. WIME does not need to be adapted in any way to deal with noise. On the contrary, the EMD is not able to properly handle such erratic signals, improved versions of this method such as the Ensemble Empirical Mode Decomposition [153] and the Complete Ensemble Empirical Mode Decomposition with Adaptive Noise [142] should be preferred in this context. For the record, when performing the EMD on $f + X$, the IMF which is the closer to $f$ in terms of RMSE and PCC has a RMSE of 0.35 and a PCC of 0.869, which is well below the results presented in Table 6.5. Therefore, the natural tolerance to noise of WIME is part of its key assets.

### 6.3.6 Test on real-life signals

#### Electrocardiogram

In this last section, we first revisit the classic real-life example of the electrocardiogram (ECG), as in several studies such as [35, 61]. Rather than providing an accurate reconstruction of the signal, the point of this example is merely to show that WIME still gives coherent components for real-life noisy data. Of course, it would be interesting to run WIME on hundreds of ECGs from healthy and non-healthy subjects and compare the main frequencies and components obtained, as well as their amplitudes or their variations in order to establish criteria that help the detection of particular illnesses. This is obviously far beyond the scope of this section though.

The ECG signal analyzed in [61] is used; the results are presented in Figure 6.8. It can be seen that the heartbeat frequency is recovered with the first component extracted and that the third one allows an accurate detection of the heartbeat impulses. Both of them could be used in real-life applications (e.g. measuring the time between consecutive maxima and the intensity of the peaks), as detailed in [35]. It is important to note that this signal, due to its Dirac-like impulses, is not really characterized as those of the form of equation (6.1). Therefore, WIME only provides an approximation of $f$ with AM-FM

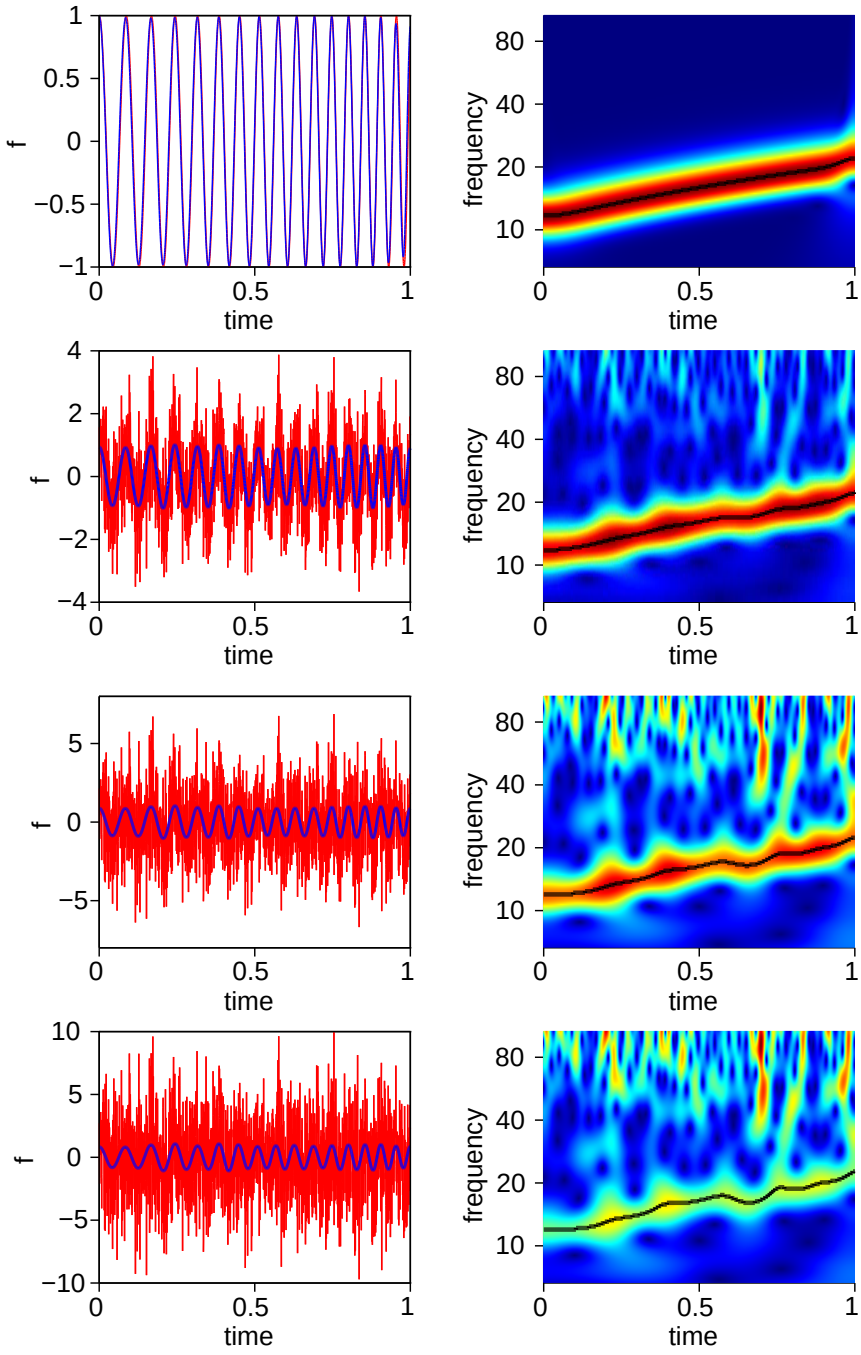


Figure 6.7: Top row: (left) original chirp (red) and extracted component (blue) associated with the ridge of the TF representation of the signal (right). Remaining rows: the same with $f + X$, $f + 2X$, $f + 3X$, where $X$ is a Gaussian white noise with zero mean and variance 1. One can see that, despite the high level of noise, WIME is still able to retrieve the initial chirp. Moreover, it does not require any pre/post-processing treatments nor extra computational power.

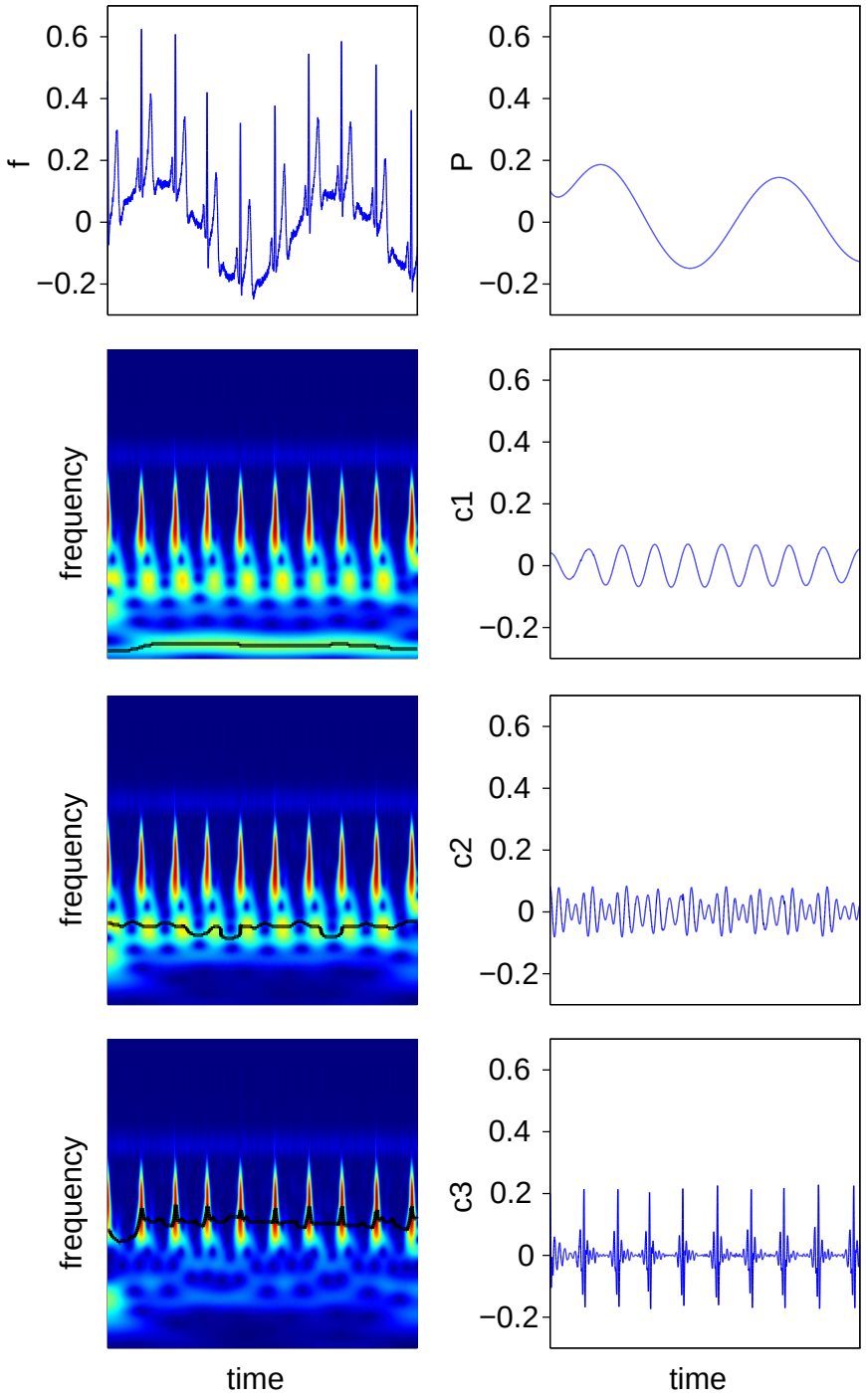


Figure 6.8: Top: the ECG signal (left) and a polynomial trend (right) extracted as a preprocessing of the signal. Then, the first three successive TF representations and components obtained with WIME. It can be noted that $c_1$ corresponds to the heartbeat frequency and that $c_3$ allows to identify instantly the heartbeat impulses.

components but still manages to perform reasonably well. Be that as it may, the opinion of a cardiologist would be useful for a proper interpretation of the results.

### ONI index

As a final test, we apply WIME on the ONI index analyzed in chapter 5, which is closer to equation (6.1) than the ECG. The components extracted with WIME are presented in Figure 6.9 and Figure 6.10. It can be seen that WIME still gives consistent results with this signal. The ridges extracted are not chaotic, and the components associated are representative of the signal, with periods similar to those obtained in chapter 5. The energy of the TF plane is drained so that the reconstruction appears smooth but accurate: the RMSE equals 0.22 and the PCC 0.96. We recall that these results are obtained with no pre/post-processing treatment or adaptation of WIME; it is thus reasonable to assert that it can be used in the context of real-life data analysis.

## 6.4 Conclusion

We introduced a new method within the framework of time-frequency analysis termed Wavelet-Induced Mode Extraction (WIME), whose main purpose is to extract automatically the intrinsic components that form AM-FM-like signals. This technique borrows some characteristics of excellent mode decomposition procedures while trying to resolve some of their defects. The underlying philosophy consists in successively deriving components from high-energy ridges of the TF plane initiated by a segmentation of the wavelet spectrum.

When applied to toy examples, WIME displayed accurate decomposition skills. Indeed, the components retrieval involving chirps or other non-stationary sources was carried out almost flawlessly. Compared to the EMD, the results appeared as good in the simple cases and better in the trickier ones chosen here. As a matter of example, components that were well-separated with respect to their amplitude but with intersecting trajectories in their TF representations were definitely recovered, while the EMD failed to do so. Besides, when the focus was on the recapture of known frequencies in a mode-mixing problem, WIME outperformed the EMD. It also appeared that the natural tolerance to noise of WIME makes it suitable to study natural time series. As a matter of example, the application to an ECG and the ONI index showed that sound results are still obtained with real-life data.

This chapter consists in the first results that we obtained with WIME. It goes without saying that we aim at developing this method as much as possible, studying its properties in more detail and comparing its skills with many other techniques. Besides, we have recently released a practical easy-to-use Scilab toolbox[6] so that non-specialist researchers get to know better wavelets and time-frequency analysis and can carry out their own mode decomposition experiments.

[6] `https://atoms.scilab.org/toolboxes/toolbox_WIME/0.1.0`

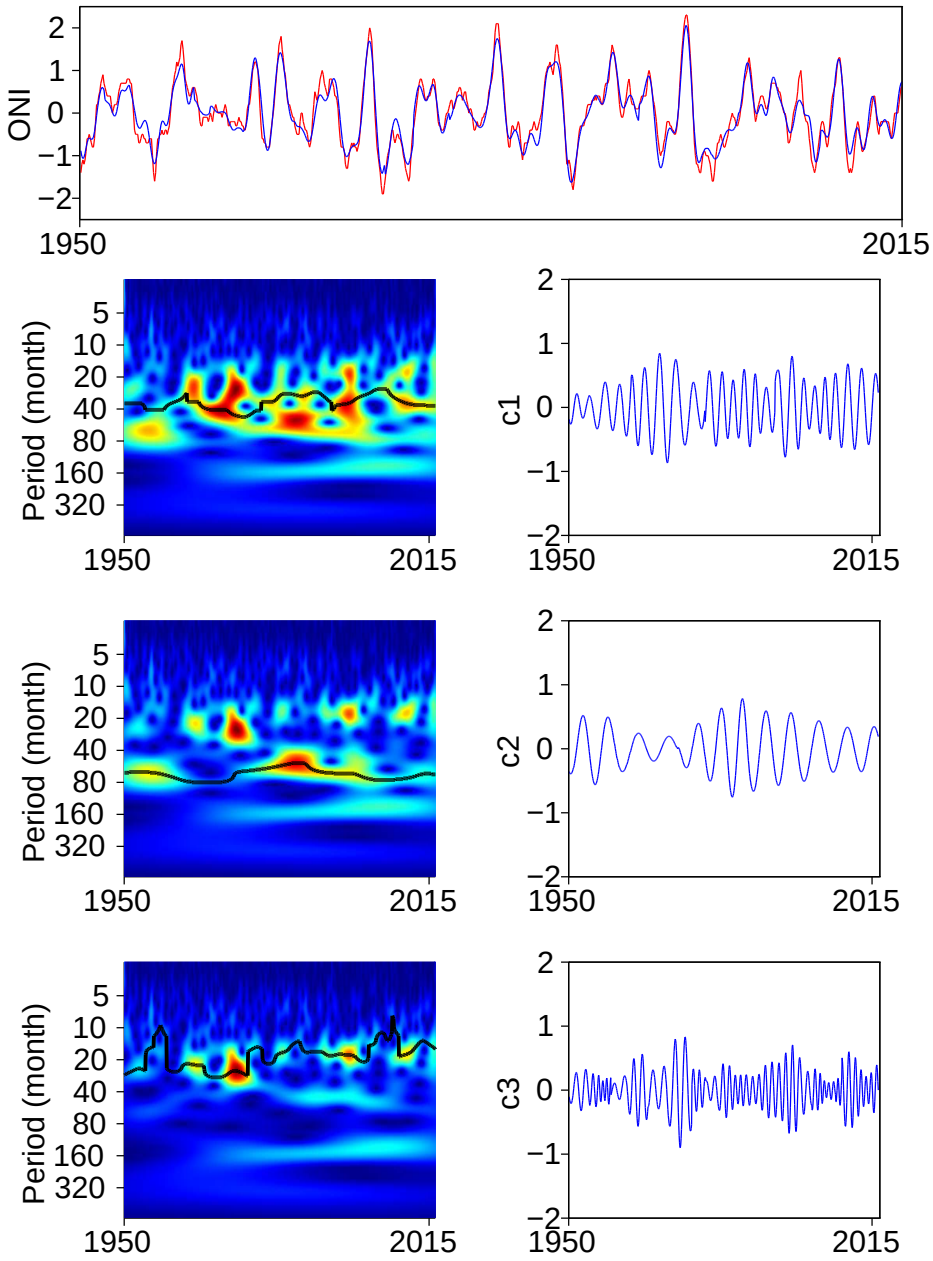


Figure 6.9: Top: original ENSO signal (red) and reconstructed signal (blue). Then, the first three successive TF representations and components obtained with WIME.

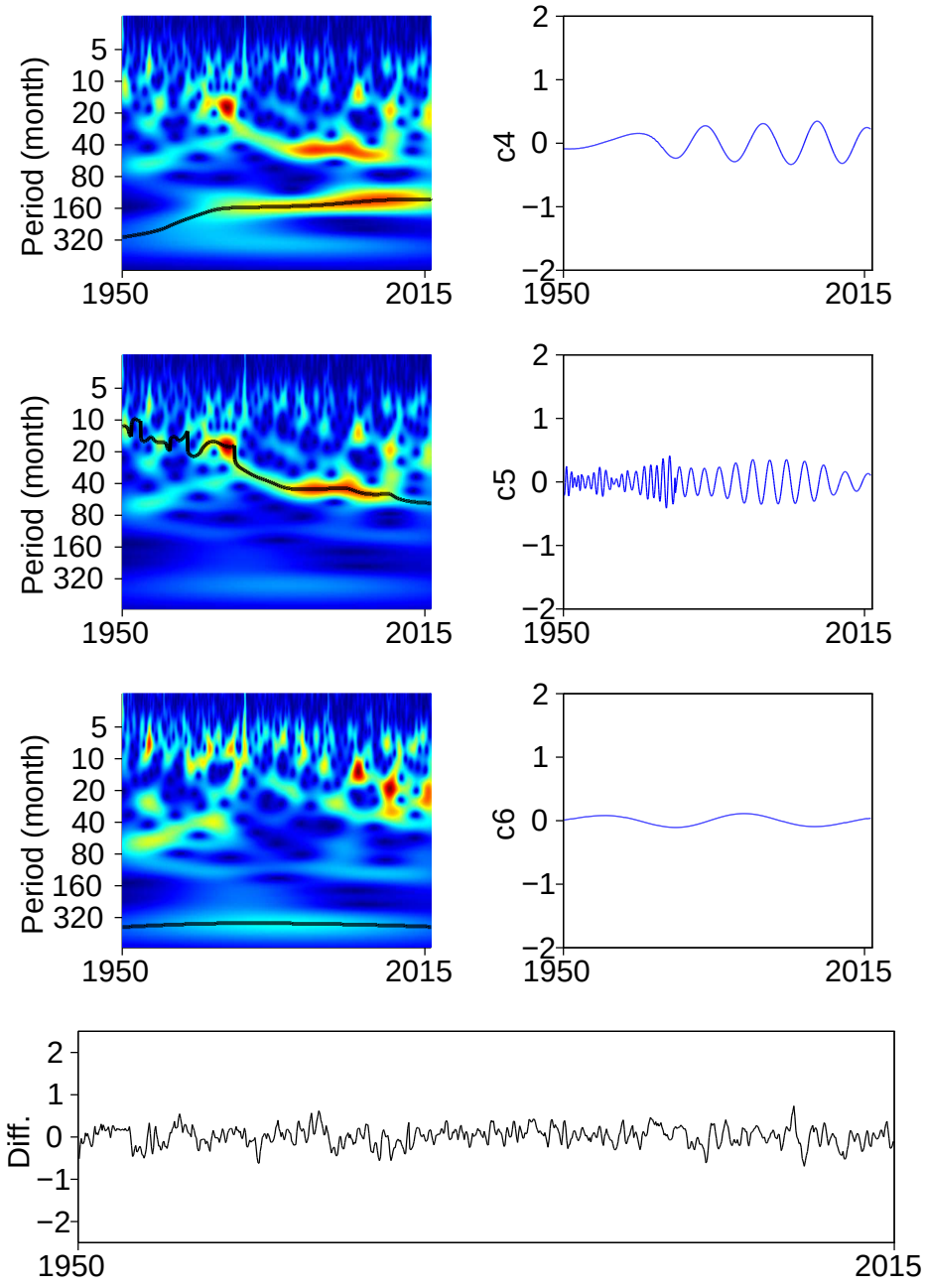


Figure 6.10: The last three TF representations and components obtained with WIME. Then, the difference between the original ONI signal and the reconstruction.

# Appendix

## 6.A Empirical Mode Decomposition

The basic idea of the EMD is simple and consists in the following steps. More details can be found in e.g. [55, 71, 124].

1) For a signal $X(t)$, let
$$m_{1,0}(t) = \frac{u_{1,0}(t) + l_{1,0}(t)}{2}$$
be the mean of its upper and lower envelopes $u(t)$ and $l(t)$ as determined from a cubic-spline interpolation of local maxima and minima.

2) Compute $h_{1,0}(t)$ as:
$$h_{1,0}(t) = X(t) - m_{1,0}(t).$$

3) Now $h_{1,0}(t)$ is treated as the data, $m_{1,1}(t)$ is the mean of its upper and lower envelopes, and the process is iterated ("sifting process"):
$$h_{1,1}(t) = h_{1,0}(t) - m_{1,1}(t).$$

4) The sifting process is repeated $k$ times, i.e.
$$h_{1,k}(t) = h_{1,k-1}(t) - m_{1,k}(t),$$
until a stopping criterion is satisfied (see below).

5) Then $h_{1,k}(t)$ is considered as the component $c_1(t)$ of the signal and the whole process is repeated with the rest
$$r_1(t) = X(t) - c_1(t)$$
instead of $X(t)$. Get $c_2(t)$ then repeat with $r_2(t) = r_1(t) - c_2(t)$,...

By construction, the number of extrema is decreased when going from $r_i$ to $r_{i+1}$, and the whole decomposition is guaranteed to be completed with a finite number of modes.

The stopping criterion for the sifting process is the following. When computing $m_{i,j}(t)$, also compute
$$a_{i,j}(t) = \frac{u_{i,j}(t) - l_{i,j}(t)}{2} \quad \text{and} \quad \sigma_{i,j}(t) = \left| \frac{m_{i,j}(t)}{a_{i,j}(t)} \right|.$$
The sifting is iterated until $\sigma(t) < 0.05$ for 95% of the total length of $X(t)$ and $\sigma(t) < 0.5$ for the remaining 5%.

# Conclusion

This thesis fits in the growing body of works that promote the use of wavelet techniques in geosciences. In the first part, we focused on the WLM in the context of multifractal analysis. We described the method in detail and explained carefully the differences that occur between theory and practice. Since these differences often lead to misunderstandings in the literature, we believe that chapter 1 could prove helpful for practitioners in their research. In chapter 2, we carried out an extensive analysis of Mars topography with the WLM. We showed that this technique is at least as useful in the one-dimensional case as other methods. However, contrary to most of the approaches used in the literature, its generalization to the two-dimensional case is straightforward and appeared sharp enough to provide exploitable results on the surface roughness of Mars topography in a 2D framework. We know that this issue (the 2D analysis) is investigated by other teams, and we thus hope that the present study can pave the way for deeper analyses and for the characterization of the surface roughness of other celestial bodies. Then, in chapter 3, we used the WLM to examine the regularity of surface air temperature recorded in weather stations spread across Europe. This time, we showed that the WLM allowed to connect the Hölder exponents of the stations with the associated pressure anomalies, which was not the case with another well-known method (MFDFA). It also appeared that the clusters of exponents obtained with the k-means algorithm were often strongly correlated with a particular type of climate, which led us to investigate this relation in detail. We managed to establish simple criteria that connect Hölder exponents and the associated climate types. The results obtained were discussed and confirmed through a blind test and also with another dataset. It kept bringing consistent information: the different types of climates (Oceanic, Continental, Mediterranean) manifest through air temperature variability. In addition to the possibility to investigate more connections between other climate types in different regions of the world and their Hölder regularity, we showed that the WLM was also able to bring accurate information that turn out useful in a context of classification.

In the second part, we were concerned with the CWT in the domain of time-frequency analysis. In chapter 4, we discussed in detail the border effects problems that occur because of the finite nature of the signals studied in practice. We provided a theoretical approach, which was then completed with numerical experiments. We showed that the zero-padding seemed to be the most reasonable choice in the present context but the border effects were still hard to counteract. Therefore, we also gave an original iterative technique that allows to limit them in the reconstruction procedure of a given signal. For simple examples, the accuracy of the reconstruction could be made arbitrarily small. Then, in chapter 5, we studied the ENSO signal through the CWT to extract the main periods and components governing the signal. As for the WLM, the CWT turned out consistent with previous works for this task. We then took it a step further and used the components extracted to produce a forecasting procedure which predicts El Niño and La Niña events up to three years in advance. This result is particularly encouraging given the fact that most current models cannot make predictions more than one year ahead. However, these have better forecasting skills at short lead times, which is the reason why we believe our model could be used as a complement to other approaches for forecasting ENSO. Its simplicity motivates us to keep working on it to improve its forecasting skills. Finally, in chapter 6, the technique used to extract components from a signal was enhanced to better handle the non-stationary behavior of AM-FM modes. We established an algorithm called WIME that detects the ridges of maxima in the time-frequency plane and extracts components iteratively until a stopping criterion is met. We compared this procedure with the EMD in several situations. It appeared that the reconstruction skills of the two methods were comparable but the information provided by WIME was more consistent with reality in the most twisted cases. Let us add that a Scilab toolbox has been created so that researchers can conduct their own time-frequency experiments with WIME.

The two parts of this work seem to be independent from each other but chances are it is actually possible to combine them. This idea comes from the fact that new multifractal formalisms have been recently derived from a mixed use of both the EMD and existing multifractal methods, with satisfying success rates. More precisely, some of them (e.g. [25, 122]) consist in performing the EMD on each segment considered in the MFDFA procedure and use the last rest as the trend to remove from the segment, instead of a polynomial. Another technique, detailed in [146], constructs multiresolution quantities similar to wavelet coefficients from the envelopes of the IMFs extracted with the EMD. Each IMF is associated with a mean scale so that the coefficients can be organized in a hierarchical way. Using the largest coefficients in exactly the same spirit as the WLM, a structure function and a scaling function are obtained, which then leads to usual conclusions. Consequently, it would be particularly exciting to try to adapt such a method while staying in a wavelet context throughout the whole process: we could first use the Morlet time-frequency approach to extract components of interest and then switch to a Meyer multiresolution framework in which we could use a Daubechies-based WLM on these components and on the "detrended, irregular" rest of the signal. Hopefully we will be able to investigate this idea in detail in a near future and to come up with an algorithm that allies two of the main uses of wavelets. It would be an exhilarating way to honor the rich heritage left by the above-mentioned illustrious scientists.

# Bibliography


[1] P. Abry, M. Clausel, S. Jaffard, S.G. Roux, and B. Vedel. The hyperbolic wavelet transform: an efficient tool for multifractal analysis of anisotropic fields. *Revista Matemática Iberoamericana*, 31:313–348, 2015.

[2] P. Abry, P. Flandrin, M.S. Taqqu, and D. Veitch. *Wavelets for the Analysis, Estimation, and Synthesis of Scaling Data*, pages 39–88. John Wiley & Sons, Inc., 2002.

[3] P. Abry, S. Jaffard, and H.Wendt. A bridge between geometric measure theory and signal processing: Multifractal analysis. In *Operator-Related Function Theory and Time-Frequency Analysis*, volume 9 of *Abel Symposia*. Springer, 2012.

[4] P. Abry, S. Jaffard, and H. Wendt. *Benoit Mandelbrot: a life in many dimensions*, chapter Irregularities and scaling in signal and image processing: multifractal analysis, pages 31–117. World Scientific Publishing Company, 2014.

[5] P. Abry, S.G. Roux, H. Wendt, P. Messier, A.G. Klein, N. Tremblay, P. Borgnat, S. Jaffard, B. Vedel, J. Coddington, and L.A. Daffner. Multiscale anisotropic texture analysis and classification of photographic prints: Art scholarship meets image processing algorithms. *IEEE Signal Processing Magazine*, 32(4):18–27, July 2015.

[6] P. Abry, H. Wendt, S. Jaffard, H. Helgason, P. Gonçalves, E. Pereira, C. Charib, P. Gaucherand, and M. Doret. Methodology for multifractal analysis of heart rate variability: From lf/hf ratio to wavelet leaders. In *Nonlinear Dynamic Analysis of Biomedical Signals EMBC conference (IEEE Engineering in Medicine and Biology Conferences)*, 2010.

[7] O. Aharonson, M.T. Zuber, and D.H. Rothman. Statistics of Mars' topography from the Mars Orbiter Laser Altimeter: Slopes, correlations, and physical models. *Journal of Geophysical Research*, 106(E10):23723–23735, 2001.

[8] J. Alvarez-Ramirez, E. Rodriguez, I. Cervantes, and J.C. Echeverria. Scaling properties of image textures: A detrending fluctuation analysis approach. *Physica A: Statistical Mechanics and its Applications*, 361:677–698, 2006.

[9] A.-M. Ampère. Recherche sur quelques points de la théorie des fonctions dérivées qui conduisent à une nouvelle démonstration du théorème de Taylor, et à l'expression finie des termes qu'on néglige lorsqu'on arrête cette série à un terme quelconque. *Journal de l'École Polytechnique*, 6(13):148–181, 1806.

[10] A. Arneodo, B. Audit, N. Decoster, J.F. Muzy, and C. Vaillant. *The Science of Disasters: Climate Disruptions, Heart Attacks, and Market Crashes*, chapter Wavelet Based Multifractal Formalism: Applications to DNA Sequences, Satellite Images of the Cloud Structure, and Stock Market Data, pages 27–102. Springer, Berlin, 2002.

[11] A. Arneodo, B. Audit, P. Kestener, and S.G. Roux. Wavelet-based multifractal analysis. *Scholarpedia*, 3(3):4103, 2008. Revision 121431.

[12] A. Arneodo, E. Bacry, P.V. Graves, and J.F. Muzy. Characterizing long-range correlations in DNA sequences from wavelet analysis. *Physical Review Letters*, 74 (16):3293–3297, 1995.

[13] A. Arneodo, E. Bacry, and J.F. Muzy. The thermodynamics of fractals revisited with wavelets. *Physica A: Statistical Mechanics and its Applications*, 213:232–275, 1995.

[14] A. Arneodo, Y. d'Aubenton Carafa, E. Bacry, P.V. Graves, J.F. Muzy, and C. Thermes. Wavelet based fractal analysis of DNA sequences. *Physica D: Nonlinear Phenomena*, 96(1–4):291 – 320, 1996. Measures of Spatio-Temporal Dynamics.

[15] A. Arneodo, N. Decoster, and S.G. Roux. A wavelet-based method for multifractal image analysis. I. Methodology and test applications on isotropic and anisotropic random rough surfaces. *The European Physical Journal B - Condensed Matter and Complex Systems*, 15(3):567–600, 2000.

[16] D. Arthur and S. Vassilvitskii. K-means++: The Advantages of Careful Seeding. In *Proceedings of the Eighteenth Annual ACM-SIAM Symposium on Discrete Algorithms*, SODA'07, pages 1027–1035, Philadelphia, PA, USA, 2007. Society for Industrial and Applied Mathematics.

[17] F. Auger and P. Flandrin. Improving the readability of time-frequency and time-scale representations by the reassignment method. *IEEE Transactions on Signal Processing*, 43(5):1068–1089, May 1995.

[18] E. Bacry, J. Delour, and J. F. Muzy. Multifractal random walk. *Physical Review E: Statistical, Nonlinear, and Soft Matter Physics*, 64:026103, Jul 2001.

[19] E. Bacry, J. F. Muzy, and A. Arneodo. Singularity spectrum of fractal signals from wavelet analysis: Exact results. *Journal of Statistical Physics*, 70(3):635–674, 1993.

[20] A.G. Barnston, M.K. Tippett, M.L. L'Heureux, S. Li, and D.G. DeWitt. Skill of real-time seasonal ENSO model predictions during 2002-11: Is our capability increasing? *Bulletin of the American Meteorological Society*, 93(5):631–651, 2012.

[21] I. Bartos and I.M. Jánosi. Nonlinear correlations of daily temperature records over land. *Nonlinear Processes in Geophysics*, 13(5):571–576, 2006.

[22] R. Benzi and U. Frisch. Turbulence. 5(3):3439, 2010. revision 137205.

[23] T. Blenkinsop, J. Kruhl, and M. Kupkova. *Fractals and Dynamic Systems in Geoscience*. Springer, 2000.

[24] A. Bunde, S. Havlin, J.W. Kantelhardt, T. Penzel, J.-H. Peter, and K. Voigt. Correlated and uncorrelated regions in heart-rate fluctuations during sleep. *Physical Review Letters*, 85:3736–3739, Oct 2000.

[25] P. Caraiani. Evidence of multifractality from emerging european stock markets. *PLOS ONE*, 7(7):1–9, 07 2012.

[26] Climate Prediction Center. Oceanic Niño Index. `http://www.cpc.ncep.noaa.gov/products/analysis_monitoring/ensostuff/ensoyears2011.shtml`.

[27] E. Chassande-Mottin, F. Auger, and P. Flandrin. *Time-Frequency/Time-Scale Reassignment*, pages 233–267. Birkhäuser Boston, Boston, MA, 2003.

[28] E. Chassande-Mottin, I. Daubechies, F. Auger, and P. Flandrin. Differential reassignment. *IEEE Signal Processing Letters*, 4(10):293–294, Oct 1997.

[29] D. Chen, M.A. Cane, A. Kaplan, S.E. Zebiak, and D. Huang. Predictability of El Niño over the past 148 years. *Nature*, 428(6984):733–736, 2004.

[30] L. Cohen. *Time-Frequency analysis*. Prentice-Hall, 1995.

[31] M. Costa, A. A. Priplata, L.A. Lipsitz, Z. Wu, N.E. Huang, A.L. Goldberger, and C.-K. Peng. Noise and poise: Enhancement of postural complexity in the elderly with a stochastic-resonance-based therapy. *Europhysics Letters*, 77(6):68008, 2007.

[32] A.A. Cournot. *Écrits de jeunesse et pièces diverses*. 2010.

[33] D. Cummings, R. Irizarry, N.E. Huang, T. Endy, A. Nisalak, K. Ungchusak, and D. Burke. Travelling waves in the occurrence of dengue haemorrhagic fever in Thailand. *Nature*, 427:344–347, 2004.

[34] I. Daubechies. *Ten Lectures on Wavelets*. SIAM, 1992.

[35] I. Daubechies, J. Lu, and H.-T. Wu. Synchrosqueezed wavelet transforms: An empirical mode decomposition-like tool. *Journal of Applied and Computational Harmonic Analysis*, 30(2):243–261, 2011.

[36] I. Daubechies and S. Maes. *A nonlinear squeezing of the continuous wavelet transform based on auditory nerve models*, chapter Wavelets in Medicine and Biology, pages 527–546. CRC Press, 1996.

[37] N. Decoster, S.G. Roux, and A. Arneodo. A wavelet-based method for multifractal image analysis. II. Applications to synthetic multifractal rough surfaces. *The European Physical Journal B - Condensed Matter and Complex Systems*, 15(4):739–764, 2000.

[38] A. Deliège, T. Kleyntssens, and S. Nicolay. Mars topography investigated through the wavelet leaders method: A multidimensional study of its fractal structure. *Planetary and Space Science*, 136C:46–58, 2017.

[39] A. Deliège and S. Nicolay. A wavelet leaders-based climate classification of European surface air temperature signals. In *Proceedings ITISE 2014: International work-conference on Time Series Analysis*, volume 1, pages 40–51, 2014.

[40] A. Deliège and S. Nicolay. Köppen–Geiger climate classification for Europe recaptured via the Hölder regularity of air temperature data. *Pure and Applied Geophysics*, 173(8):2885–2898, 2016.

[41] A. Deliège and S. Nicolay. *A New Wavelet-Based Mode Decomposition for Oscillating Signals and Comparison with the Empirical Mode Decomposition*, chapter Information Technology: New Generations: 13th International Conference on Information Technology, pages 959–968. Springer International Publishing, Cham, 2016.

[42] A. Deliège and S. Nicolay. Extracting oscillating components from nonstationary time series: A wavelet-induced method. *Physical Review E: Statistical, Nonlinear, and Soft Matter Physics*, 2017. Submitted for publication.

[43] Adrien Deliège and Samuel Nicolay. Analysis and indications on long-term forecasting of the Oceanic Niño Index with wavelet-induced components. *Pure and Applied Geophysics*, 174(4):1815–1826, 2017.

[44] J. Delour, J.F. Muzy, and A. Arneodo. Intermittency of 1D velocity spatial profiles in turbulence: a magnitude cumulant analysis. *European Physical Journal B: Condensed Matter Physics*, 23(2):243–248, 2001.

[45] L. Duval. Where is the starlet? `http://www.laurent-duval.eu/siva-wits-where-is-the-starlet.html`.

[46] A. Eke, P. Herman, L. Kocsis, and L.R. Kozak. Fractal characterization of complexity in temporal physiological signals. *Physiological Measurement*, 23(1):R1, 2002.

[47] C. Esser. *Regularity of functions: Genericity and multifractal analysis*. PhD thesis, Université de Liège, 2014.

[48] C. Esser, T. Kleyntssens, and S. Nicolay. A multifractal formalism for non-concave and non-increasing spectra: The leaders profile method. *Applied and Computational Harmonic Analysis*, 2016.

[49] European Climate Assessment and Dataset. `http://ecad.eu`.

[50] K.J. Falconer. *The Geometry of Fractal Sets*. Cambridge Tracts in Mathematics. Cambridge University Press, 1986.

[51] A.V. Fedorov, S.L. Harper, S.G. Philander, B. Winter, and A. Wittenberg. How predictable is El Niño? *Bulletin of the American Meteorological Society*, 84(7):911–919, 2003.

[52] P. Flandrin. Temps-fréquence et ondelettes. `http://perso.ens-lyon.fr/patrick.flandrin/tfond2.html`.

[53] P. Flandrin. *Temps-fréquence*. Hermes, 1998.

[54] P. Flandrin. Time-frequency/Time-scale analysis. In *Wavelet Analysis and its Applications*, volume 10. Academic Press, 1999.

[55] P. Flandrin, G. Rilling, and P. Gonçalves. Empirical mode decomposition as a filter bank. *IEEE Signal Processing Letters*, 11(2):112–114, 2004.

[56] J. Fourier. *Théorie analytique de la chaleur*. Firmin Didot Père et Fils, 1822.

[57] U. Frisch. Turbulence: The legacy of A.N. Kolmogorov. *Journal of Fluid Mechanics*, 317:407–410, 1996.

[58] U. Frisch and G. Parisi. Fully developed turbulence and intermittency. In *Proc. Int. Summer School Turbulence and Predictability in Geophysical Fluid Dynamics and Climate Dynamics*, 1985.

[59] D. Gabor. Theory of communication : Part 1: The analysis of information. *Journal of the Institute of Electrical Engineering*, 93-3(26):429–457, 1946.

[60] U. Gebhardt and M. Hiete. Continental upper carboniferous red beds in the variscan intermontane saale basin, central germany: orbital forcing detected by wavelet analysis. *Geological Society, London, Special Publications*, 376(1):177–199, 2013.

[61] J. Gilles. Empirical wavelet transform. *IEEE Transactions on Signal Processing*, 61(16):3999–4010, 2013.

[62] M.H. Glantz. *Currents of Change: Impacts of El Niño and La Niña on climate society*. Cambridge University Press, 2001.

[63] A. Grossmann and J. Morlet. Decomposition of Hardy functions into square integrable wavelets of constant shape. *SIAM Journal on Mathematical Analysis*, 15(4):723–736, 1984.

[64] G.-F. Gu and W.-X. Zhou. Detrended fluctuation analysis for fractals and multifractals in higher dimensions. *Physical Review E: Statistical, Nonlinear, and Soft Matter Physics*, 74(6):061104, 2006.

[65] A. Haar. Zur theorie der orthogonalen funktionensysteme. *Mathematische Annalen*, 69(3):331–371, 1910.

[66] G.H. Hardy. Weierstrass's non-differentiable function. *Transactions of the American Mathematical Society*, 17(3):301–325, 1916.

[67] J.A. Hartigan and M.A. Wong. Algorithm AS 136: A k-means clustering algorithm. *Journal of the Royal Statistical Society. Series C (Applied Statistics)*, 28(1):100–108, 1979.

[68] C. Hermite. *Correspondance d'Hermite et de Stieltjes*, chapter Lettre 374 d'Hermite à Stieljtes du 20 mai 1893, pages 317–319. Gauthier-Villars, 1905.

[69] S.M. Hsiang, K.C. Meng, and M.A. Cane. Civil conflicts are associated with the global climate. *Nature*, 476(7361):438–441, 2011.

[70] N. E. Huang and Z. Wu. A review on Hilbert-Huang transform: Method and its applications to geophysical studies. *Reviews of Geophysics*, 46:RG2006, June 2008.

[71] N.E. Huang, Z. Shen, S.R. Long, M.C. Wu, H.H. Shih, Q. Zheng, N.-C. Yen, C.C. Tung, and H.H. Liu. The empirical mode decomposition and the Hilbert spectrum for nonlinear and non-stationary time series analysis. *Proceedings of the Royal Society of London A*, 454:903–995, 1998.

[72] N.E. Huang, M.-L. Wu, W. Qu, S. Long, S. Shen, and J. Zhang. Applications of Hilbert-Huang transform to non-stationary financial time series analysis. *Applied Stochastic Models in Business and Industry*, 19:245–268, 2003.

[73] S. Jaffard. Wavelet techniques in multifractal analysis. *Proceedings of symposia in pure mathematics*, 72:91–152, 2004.

[74] S. Jaffard, P. Abry, H. Wendt, S.G. Roux, and B. Vedel. The contribution of wavelets in multifractal analysis. In *Series in Contemporary Applied Mathematics*. Higher Education Press, World Scientific Publishing, 2009.

[75] S. Jaffard, B. Lashermes, and P. Abry. *Wavelet Leaders in Multifractal Analysis*, pages 201–246. Birkhäuser Basel, Basel, 2007.

[76] S. Jaffard and S. Nicolay. Pointwise smoothness of space-filling functions. *Applied and Computational Harmonic Analysis*, 26:181–199, 2009.

[77] L. Jiang, N. Li, Z. Fu, and J. Zhang. Long-range correlation behaviors for the 0-cm average ground surface temperature and average air temperature over China. *Theoretical and Applied Climatology*, 119(1):25–31, 2015.

[78] L. Jiang, N. Yuan, Z. Fu, D. Wang, X. Zhao, and X. Zhu. Subarea characteristics of the long-range correlations and the index $\chi$ for daily temperature records over China. *Theoretical and Applied Climatology*, 109(1):261–270, 2012.

[79] F.-F. Jin, J.D. Neelin, and M. Ghil. El Niño on the devil's staircase: Annual subharmonic steps to chaos. *Science*, 264(5155):70–72, 1994.

[80] J.W. Kantelhardt, E. Koscielny-Bunde, H.A. Rego, S. Havlin, and A. Bunde. Detecting long-range correlations with detrended fluctuation analysis. *Physica A: Statistical Mechanics and its Applications*, 295(3–4):441 – 454, 2001.

[81] J.W. Kantelhardt, S.A. Zschiegner, E. Koscielny-Bunde, A. Bunde, S. Havlin, and H.E. Stanley. Multifractal detrended fluctuation analysis of nonstationary time series. *Physica A: Statistical Mechanics and its Applications*, 316:87–114, 2002.

[82] D. Kondrashov, S. Kravtsov, A.W. Robertson, and M. Ghil. A hierarchy of data-based ENSO models. *Journal of Climate*, 18(21):4425–4444, 2005.

[83] W. Köppen. *Das geographische System der Klimate*. Gebrüder Borntraeger, Berlin, 1936.

[84] E. Koscielny-Bunde, A. Bunde, S. Havlin, and Y. Goldreich. Analysis of daily temperature fluctuations. *Physica A: Statistical Mechanics and its Applications*, 231:393–396, 1996.

[85] E. Koscielny-Bunde, A. Bunde, S. Havlin, H.E. Roman, Y. Goldreich, and H.-J. Schellnhuber. Indication of a universal persistence law governing atmospheric variability. *Physical Review Letters*, 81:729–732, 1998.

[86] D. Kreit and S. Nicolay. Some characterizations of generalized Hölder spaces. *Mathematische Nachrichten*, 285(17-18):2157–2172, 2012.

[87] D. Kreit and S. Nicolay. Generalized pointwise Hölder spaces. *ArXiv e-prints*, July Submitted for publication.

[88] M.A. Kreslavsky and J.W. Head. Kilometer-scale roughness of Mars: Results from MOLA data analysis. *Journal of Geophysical Research*, 105(E11):26695–26711, 2000.

[89] A. Kucharski. Math's beautiful monsters: How a destructive idea paved the way for modern math. Online, April 2014.

[90] F. Landais, F. Schmidt, and S. Lovejoy. Universal multifractal Martian topography. *Nonlinear Processes in Geophysics*, 22(6):713–722, 2015.

[91] B. Lashermes. *Analyse multifractale pratique : coefficients dominants et ordres critiques. Applications à la turbulence pleinement développée. Effets de nombre de Reynolds fini.* PhD thesis, École Normale Supérieure de Lyon, 2005.

[92] B. Lashermes, S.G. Roux, P. Abry, and S. Jaffard. Comprehensive multifractal analysis of turbulent velocity using wavelet leaders. *European Physical Journal B: Condensed Matter Physics*, 61 (2):201–215, 2008.

[93] P.G. Lemarié and Y. Meyer. Ondelettes et bases hilbertiennes. *Revista Matemática Iberoamericana*, 2(1-2):1–18, 1986.

[94] S. Lovejoy and D. Schertzer. *The Weather and Climate: Emergent Laws and Multifractal Cascades.* Cambridge University Press, 2013.

[95] B.D. Malamud and D.L. Turcotte. Wavelet analyses of Mars polar topography. *Journal of Geophysical Research*, 106(E8):17497–17504, 2001.

[96] S.G. Mallat. Multiresolution approximations and wavelet orthonormal bases of L2(R). *Transactions of the American Mathematical Society*, 315(1):69–87, 1989.

[97] S.G. Mallat. A theory for multiresolution signal decomposition: the wavelet representation. *IEEE Transactions on Pattern Analysis and Machine Intelligence*, 11(7):674–693, Jul 1989.

[98] S.G. Mallat. *A Wavelet Tour of Signal Processing.* Academic Press, 1999.

[99] S.J. Mason and G.M. Mimmack. Comparison of some statistical methods of probabilistic forecasting of ENSO. *Journal of Climate*, 15(1):8–29, 2002.

[100] Y. Meyer. *Wavelets and Operators*, volume 1. Cambridge University Press, Cambridge, 1993.

[101] Y. Meyer and R. Coifman. *Wavelets: Calderon-Zygmund and Multilinear Operators*. Cambridge University Press, 1997.

[102] J.F. Muzy, E. Bacry, and A. Arneodo. Wavelets and multifractal formalism for singular signals: Application to turbulence data. *Physical Review Letters*, 67:3515–3518, Dec 1991.

[103] J.F. Muzy, E. Bacry, and A. Arneodo. Multifractal formalism for fractal signals: The structure-function approach versus the wavelet-transform modulus-maxima method. *Physical Review E: Statistical, Nonlinear, and Soft Matter Physics*, 47:875–884, Feb 1993.

[104] S. Nicolay. A wavelet-based mode decomposition. *European Physical Journal B: Condensed Matter Physics*, 80:223–232, 2011.

[105] S. Nicolay, G. Mabille, X. Fettweis, and M. Erpicum. 30 and 43 months period cycles found in air temperature time series using the Morlet wavelet method. *Climate dynamics*, 33(7):1117–1129, 2009.

[106] V. Nikora and D. Goring. Mars topography: Bulk statistics and spectral scaling. *Chaos, Solitons and Fractals*, 19:427–439, 2004.

[107] V. Nikora and D. Goring. Martian topography: Scaling, craters, and high-order statistics. *Mathematical Geology*, 37(4):337–355, 2005.

[108] V. Nikora and D. Goring. Spectral scaling in Mars topography: Effect of craters. *Acta Geophysica*, 54(1):102–112, 2006.

[109] NOAA Earth System Research Laboratory. NCEP/NCAR Reanalysis Project. `http://www.esrl.noaa.gov/`.

[110] Y.M. Okumura. Origins of tropical pacific decadal variability: Role of stochastic atmospheric forcing from the South Pacific. *Journal of Climate*, 26(24):9791–9796, 2013.

[111] R. Orosei, R. Bianchi, A. Coradini, S. Espinasse, C. Federico, A. Ferriccioni, and A.I. Gavrishin. Self-affine behavior of Martian topography at kilometer scale from Mars Orbiter Laser Altimeter data. *Journal of Geophysical Research*, 108(E4):8023, 2003.

[112] S.-A. Ouadfeul, editor. *Fractal Analysis and Chaos in Geosciences*. InTech, 2012.

[113] E.R. Pacola, V.I. Quandt, F.K. Schneider, and M.A. Sovierzoski. *World Congress on Medical Physics and Biomedical Engineering, IFMBE Proceedings (IFMBE)*, volume 39, chapter The Wavelet Transform Border Effect in EEG Spike Signals, pages 593–596. Springer Berlin Heidelberg, Berlin, Heidelberg, 2013.

[114] G. Parisi and U. Frisch. On the singularity structure of fully developed turbulence. In *Proceedings of the International Summer School in Physics Enrico Fermi*, pages 84–87. edited by M. Ghil, R. Benzi, and G. Parisi, New York: Elsevier, 1985.

[115] M.C. Peel, B.L. Finlayson, and T.A. McMahon. Updated world map of the Köppen-Geiger climate classification. *Hydrology and Earth System Sciences*, 11(5):1633–1644, 2007.

[116] C.-K. Peng, S.V. Buldyrev, S. Havlin, M. Simons, H.E. Stanley, and A.L. Goldberger. Mosaic organization of DNA nucleotides. *Physical Review E: Statistical, Nonlinear, and Soft Matter Physics*, 49:1685–1689, 1994.

[117] D. Petrova, S.J. Koopman, J. Ballester, and X. Rodó. Improving the long-lead predictability of El Niño using a novel forecasting scheme based on a dynamic components model. *Climate Dynamics*, pages 1–28, 2016.

[118] C.A. Pickover. *The Math Book: From Pythagoras to the 57th Dimension, 250 Milestones in the History of Mathematics*. Sterling, 2009.

[119] H. Poincaré. *Théorie analytique de la propagation de la chaleur*, 1895. Notes de cours rédigées par Rouyer et Baire.

[120] H. Poincaré. *Science et Méthode*. Flammarion, 1908.

[121] A. Pommerol, S. Chakraborty, and N. Thomas. Comparative study of the surface roughness of the Moon, Mars and Mercury. *Planetary and Space Science*, 73:287–293, 2012.

[122] X.-Y. Qian, G.-F. Gu, and W.-X. Zhou. Modified detrended fluctuation analysis based on empirical mode decomposition for the characterization of anti-persistent processes. *Physica A: Statistical Mechanics and its Applications*, 390(23–24):4388 – 4395, 2011.

[123] M. Riley, S. Bonnette, N. Kuznetsov, S. Wallot, and J. Gao. A tutorial introduction to adaptive fractal analysis. *Frontiers in Physiology*, 3:371, 2012.

[124] G. Rilling, P. Flandrin, and P. Gonçalves. On empirical mode decomposition and its algorithms. In *IEEE-EURASIP Workshop Nonlinear Signal Image Processing (NSIP)*, 2003.

[125] S.G. Roux, P. Abry, B. Vedel, S. Jaffard, and H. Wendt. Hyperbolic wavelet leaders for anisotropic multifractal texture analysis. In *2016 IEEE International Conference on Image Processing (ICIP)*, pages 3558–3562, Sept 2016.

[126] S.G. Roux, M. Clausel, B. Vedel, S. Jaffard, and P. Abry. Self-similar anisotropic texture analysis: The hyperbolic wavelet transform contribution. *IEEE Transactions on Image Processing*, 22(11):4353–4363, Nov 2013.

[127] G. Saracco, P. Guillemain, and R. Kronland-Martinet. Characterization of elastic shells by the use of the wavelet transform. *IEEE Ultrasonics*, 2:881–885, 1990.

[128] D. Schertzer and S. Lovejoy. *Non-Linear Variability in Geophysics: Scaling and fractals*. Springer Netherlands, 1991.

[129] D. Schertzer, S. Lovejoy, and P. Hubert. An introduction to stochastic multifractal fields. In *ISFMA Symposium on Environmental Science and Engineering with related Mathematical Problems*, 2002.

[130] M.K. Shepard, B.A. Campbell, M.H. Bulmer, T.G. Farr, L.R. Gaddis, and J.J. Plaut. The roughness of natural terrain: A planetary and remote sensing perspective. *Journal of Geophysical Research*, 106(E12):32777–32795, 2001.

[131] SILSO World Data Center. The International Sunspot Number. *International Sunspot Number Monthly Bulletin and online catalogue*, 2016.

[132] D. Smith, G. Neumann, R.E. Arvidson, E.A. Guinness, and S. Slavney. Mars global surveyor laser altimeter mission experiment gridded data record, mgs-m-mola-5-megdr-l3-v1.0. Technical report, NASA Planetary Data System, 2003.

[133] D.E. Smith, M.T. Zuber, H.V. Frey, J.B. Garvin, J.W. Head, et al. Mars orbiter laser altimeter: Experiment summary after the first year of global mapping of Mars. *Journal of Geophysical Research*, 106(E10):23689–23722, 2001.

[134] H. Su, Q. Liu, and J. Li. Alleviating border effects in wavelet transforms for nonlinear time-varying signal analysis. *Advances in Electrical and Computer Engineering*, 11(3):55–60, 2011.

[135] P. Talkner and R.O. Weber. Power spectrum and detrended fluctuation analysis: Application to daily temperatures. *Physical Review E: Statistical, Nonlinear, and Soft Matter Physics*, 62:150–160, Jul 2000.

[136] K. Tank and Coauthors. Daily dataset of 20th-century surface air temperature and precipitation series for the European Climate Assessment. *International Journal of Climatology*, 22:1441–1453, 2002.

[137] Y. Tessier, S. Lovejoy, and D. Schertzer. Universal multifractals: Theory and observations for rain and clouds. *Journal of Applied Meteorology*, 1993.

[138] J. Thim. Continuous Nowhere Differentiable Functions. Master's thesis, Lulea University of Technology, 2003.

[139] C.J. Thompson and D.S. Battisti. A linear stochastic dynamical model of ENSO. Part II: Analysis. *Journal of Climate*, 14(4):445–466, 2001.

[140] M.K. Tippett and A.G. Barnston. Skill of multimodel ENSO probability forecasts. *Monthly Weather Review*, 136(10):3933–3946, 2008.

[141] C. Torrence and G. Compo. A practical guide to wavelet analysis. *Bulletin of the American Meteorological Society*, 79:61–78, 1998.

[142] M.E. Torres, M.A. Colominas, G. Schlotthauer, and P. Flandrin. A complete ensemble empirical mode decomposition with adaptive noise. In *IEEE International Conference on Acoustic, Speech and Signal Processing (ICASSP)*, 2011.

[143] K. Trenberth. The climate data guide: Niño SST indices (Niño 1+2, 3, 3.4, 4; ONI and TNI). Online, February 2016.

[144] K. Weierstrass. *Abhandlungen aus der Functionenlehre*. Julius Springer, 1886.

[145] K. Weierstrass. *Königlich Preussichen Akademie der Wissenschaften, Mathematische Werke von Karl Weierstrass*, chapter Über continuirliche Functionen eines reellen Arguments, die für keinen Wert des letzteren einen bestimmten Differentialquotienten besitzen., pages 71–74. Berlin, Germany: Mayer & Mueller, 1895.

[146] G.S. Welter and P.A.A. Esquef. Multifractal analysis based on amplitude extrema of intrinsic mode functions. *Physical Review E: Statistical, Nonlinear, and Soft Matter Physics*, 87:032916, Mar 2013.

[147] H. Wendt. *Contributions of Wavelet Leaders and Bootstrap to Multifractal Analysis: Images, Estimation Performance, Dependence Structure and Vanishing Moments. Confidence Intervals and Hypothesis Tests.* PhD thesis, École Normale Supérieure de Lyon, 2008.

[148] H. Wendt, P. Abry, and S. Jaffard. Bootstrap for Empirical Multifractal Analysis. *IEEE Signal Processing Magazine*, 24:38–48, July 2007.

[149] H. Wendt, P. Abry, S. Jaffard, H. Ji, and Z. Shen. Wavelet leader multifractal analysis for texture classification. In *Proc IEEE conf. ICIP*, 2009.

[150] H. Wendt, P. Abry, S.G. Roux, S. Jaffard, and B. Vedel. Analyse multifractale d'images: l'apport des coefficients dominants. *Traitement du Signal*, 25(4-5):47–65, 2009.

[151] H. Wendt, S.G. Roux, S. Jaffard, and P. Abry. Wavelet leaders and bootstrap for multifractal analysis of images. *Signal Processing*, 89(6):1100 – 1114, 2009.

[152] N. Wiener. *I Am a Mathematician*. MIT Press, 1956.

[153] Z. Wu and N.E. Huang. Ensemble empirical mode decomposition: A noise-assisted data analysis method. *Advances in Adaptative Data Analysis*, 1:1–41, 2009.

[154] F. Zheng, J. Zhu, R.H. Zhang, and G. Zhou. Improved ENSO forecasts by assimilating sea surface temperature observations into an intermediate coupled model. *Advances in Atmospheric Sciences*, 23(4):615–624, 2006.

[155] J. Zhu, G.Q. Zhou, R.H. Zhang, and Z. Sun. Improving ENSO prediction in a hybrid coupled model with an embedded entrainment temperature parameterisation. *International Journal of Climatology*, online, 2012.

[156] A. Zifan. Enhanced, modified, and vectorized Europe map of Köppen climate classification. For Wikimedia Commons `https://en.wikipedia.org/wiki/File:Europe_map_of_K%C3%B6ppen_climate_classification.svg`, February 2016. Derived from World Köppen Classification.svg.